

UNIVERSITÄTSKLINIKUM HAMBURG-EPPENDORF

Klinik und Poliklinik für Pädiatrische Hämatologie und Onkologie

Prof. Dr. med. Stefan Rutkowski

The Role of SMARCA4 in the Development of WNT and Group 3 Medulloblastoma

Dissertation

zur Erlangung des Doktorgrades Dr. rer. biol. hum.
an der Medizinischen Fakultät der Universität Hamburg

vorgelegt von:

Carolin Göbel

aus Bad Soden am Taunus

Hamburg 2023

**Angenommen von der
Medizinischen Fakultät der Universität Hamburg am: 21.09.2023**

Veröffentlicht mit Genehmigung der Medizinischen Fakultät der Universität Hamburg.

Prüfungsausschuss, der/die Vorsitzende: Prof. Dr. med. Ulrich Schüller

Prüfungsausschuss, zweite/r Gutachter/in: Priv.-Doz. Dr. rer. nat. Malte Kriegs

I. TABLE OF CONTENTS

I.	TABLE OF CONTENTS	3
II.	ABBREVIATIONS	4
1	INTRODUCTION	9
1.1	SMARCA4 and the BAF Chromatin Remodeling Complex	9
1.2	Medulloblastoma	12
1.3	Mouse Models	17
1.4	Aim of this Work	24
2	MATERIALS AND METHODS	25
2.1	Materials	25
2.2	Cloning of Constructs	34
2.3	Mouse Experiments	36
2.4	Cell Culture.....	39
2.5	Histological Analysis of Tissues and Cells	45
2.6	Protein Analysis by Western Blotting.....	49
2.7	Methylation Analysis.....	50
2.8	Gene Expression Analysis.....	51
2.9	Single-Cell Gene Expression Analysis	52
2.10	Statistical Analysis.....	54
3	RESULTS	55
3.1	Characterization of SMARCA4 Variants <i>in vitro</i>	55
3.2	SMARCA4 in the Development of Group 3 Medulloblastoma	59
3.3	SMARCA4 in the Development of WNT Medulloblastoma	68
4	DISCUSSION	82
4.1	Characterization of SMARCA4 Variants <i>in vitro</i>	82
4.2	SMARCA4 in the Development of Group 3 Medulloblastoma	84
4.3	SMARCA4 in the Development of WNT Medulloblastoma	88
4.4	Conclusions and Outlook	94
5	ABSTRACT	96
6	ZUSAMMENFASSUNG	97
7	REFERENCES	98
8	APPENDIX	115
8.1	Supplementary Figures	115
8.2	Supplementary Tables	124
9	DANKSAGUNG	129
10	CURRICULUM VITAE	130
11	LIST OF PUBLICATIONS	131
12	EIDESSTATTLICHE VERSICHERUNG	132

II. ABBREVIATIONS

Table 1. List of abbreviations

Abbreviation	Meaning
°C	Degree Celsius
μL	Microliter(s)
μm	Micrometer(s)
7-AAD	7-Aminoactinomycin D
ATRT	Atypical Teratoid Rhabdoid Tumor
ATAC	Assay for Transposase-Accessible Chromatin
ATP	Adenosine Triphosphate
BAF	BRG1/BRM-Associated Factor
BLBP	Brain Lipid Binding Protein
bp	Base Pair(s)
BrdU	Bromodeoxyuridine
BRG1	Brahma-Related Gene 1
BRM	BRAHMA
BSA	Bovine Serum Albumin
CC3	Cleaved Caspase-3
CDK4/6	Cyclin Dependent Kinase 4/6
ChIP	Chromatin Immunoprecipitation
cm	Centimeter(s)
cm ²	Square Centimeter(s)
CMV	Cytomegalovirus
C-MYC	v-Myc Myelocytomatosis Viral Oncogene Homolog
CNS	Central Nervous System
CNV	Copy Number Variation
CO ₂	Carbon Dioxide
cPD	Cumulative Population Doublings
Cre	Causing Recombination
CREB	cAMP Response Element-Binding Protein
CREBBP	CREB-Binding Protein
CSI	Craniospinal Irradiation
d	Day
DAB	3,3'-Diaminobenzidine
DAPI	4',6-Diamidino-2-Phenylindole
ddH ₂ O	Double Distilled Water
DEPC	Diethyl Pyrocarbonate
DMEM	Dulbecco's Modified Eagle Medium
DMSO	Dimethyl Sulfoxide

Abbreviation	Meaning
DNA	Deoxyribonucleic Acid
dNTP	Deoxynucleotide Triphosphate
DPBS	Dulbecco's Balanced Salt Solution
DTT	Dithiothreitol
ECL	Enhanced Chemiluminescence
EDTA	Ethylenediaminetetraacetic Acid
EGF	Epidermal Growth Factor
EGL	External Granular Layer
EMEM	Eagle's Minimal Essential Medium
ESC	Embryonic Stem Cell
EtOH	Ethanol
FACS	Fluorescence Activated Cell Sorting
FCS	Fetal Calf Serum
FDR	False Discovery Rate
FFPE	Formalin-Fixed Paraffin-Embedded
FGF	Fibroblast Growth Factor
Fig.	Figure
fl	Flanked by LoxP sites ('floxed')
FSC	Forward Scatter
g	Gram(s)
G	Group(s)
G3/4	Group 3/4 (Medulloblastoma)
GABA	Gamma-Aminobutyric Acid
GAPDH	Glyceraldehyde-3-Phosphate-Dehydrogenase
GCP	Granule Cell Precursor(s)
gDNA	Genomic DNA
GEMM	Genetically Engineered Mouse Model
(h)GFAP	(Human) Glial Fibrillary Acidic Protein
GFP	Green Fluorescent Protein
Glc	Glucose
GLT-1	Glutamate Transporter 1
GLUT-1	Glucose Transporter 1
GO	Gene Ontology
HE	Hematoxylin and Eosin
H3K27Me3	Histone H3 Trimethylated at Lysine 27
HBSS	Hanks' Balanced Salt Solution
HCl	Hydrochloric Acid
HDAC	Histone Deacetylase
HEPES	4-(2-Hydroxyethyl)-1-Piperazineethanesulfonic Acid

Abbreviation	Meaning
HPC	Hindbrain Progenitor Cells
HRP	Horseradish Peroxidase
i.p.	Intraperitoneal
IF	Immunofluorescence
IF-P	Immunofluorescence Staining of Paraffin Slides
IGL	Internal Granular Layer
IHC	Immunohistochemistry
IHC-P	Immunohistochemistry Staining of Paraffin Slides
Int-1	Integrase-1
IRES	Internal Ribosome Entry Side
kb	Kilo Bases
KCl	Potassium Chloride
L	Liter(s)
LB	Lysogeny Broth
LCA	Large Cell/Anaplastic
LDS	Lithium Dodecyl Sulfate
logFC	Log Fold Change
loxP	Locus of X-over P1
LRL	Lower Rhombic Lip
mo	Month(s)
M	Molar
mA	Milli-Ampère
MB	Medulloblastoma
MBEN	Medulloblastoma with Extensive Nodularity
MEM-NEAA	Minimum Essential Medium-Non-Essential Amino Acids
MES	2-[N-Morpholino]ethanesulfonic Acid
mg	Milligram(s)
MgCl ₂	Magnesium Chloride
min	Minute(s)
mio	Million(s)
mL	Milliliter(s)
mM	Millimolar
MOI	Multiplicity of Infection
mRNA	Messenger RNA
ms	Millisecond(s)
MSCV	Murine Stem Cell Virus
MYC	v-Myc Avian Myelocytomatosis Viral Oncogene Homolog
N	Normal
n.a.	Not Available

Abbreviation	Meaning
NaCl	Sodium Chloride
NaOH	Sodium Hydroxide
nBAF	Neuronal BAF Complex
NEAA	Non-Essential Amino Acids
NeuN	Neuronal Nuclear Protein
NGS	Normal Goat Serum
nm	Nanometer(s)
npBAF	Neural Progenitor BAF Complex
nr.	Number
ns	Not Significant
NSC	Neural Stem Cells
NSCLC	Non-Small-Cell Lung Cancer
NSG	NOD Scid Gamma
OLIG2	Oligodendrocyte Transcription Factor
OS	Overall Survival
OTX2	Orthodenticle Homeobox 2
P	Passage (Cell Culture) or Postnatal Day (Mouse)
PAP	Peroxidase-Antiperoxidase
PAX2	Paired Box Gene 2
PBS	Phosphate Buffered Saline
PBS-T	Phosphate Buffered Saline, Supplied with Triton-X-100
PCA	Principal Component Analysis
PCR	Polymerase Chain Reaction
PD	Population Doubling
Pen/Strep	Penicillin/Streptomycin
PFA	Paraformaldehyde
pHH3	Phospho-Histone H3
PI3KCA	Phosphatidylinositol-4,5-Bisphosphate 3-Kinase Catalytic Subunit Alpha
PLO	Poly-L-Ornithine
pLV	Passiflora Latent Virus
PRC	Polycomb Repressive Complex
Prep(s)	Preparation(s)
q.s.	Quantum Satis
rec	Recombined
RFP	Red Fluorescent Protein
RIN	RNA Integrity Number
RIPA	Radioimmunoprecipitation Assay Buffer
RL	Rhombic Lip
RNA	Ribonucleic Acid

Abbreviation	Meaning
RT	Room Temperature
SCCOHT	Small Cell Carcinoma of the Ovary, Hypercalcemic Type
scrRNA	Scrambled RNA
SDS	Sodium Dodecyl Sulfate
SDS-PAGE	Sodium Dodecyl Sulfate Polyacrylamide Gel Electrophoresis
sec	Second(s)
SHH	Sonic Hedgehog
shRNA	Small Hairpin RNA
SMARCA2	SWI/SNF-related, Matrix-Associated, Actin-Dependent Regulator of Chromatin, Subfamily A, Member 2
SMARCA4	SWI/SNF-related, Matrix-Associated, Actin-Dependent Regulator of Chromatin, Subfamily A, Member 4
SOX2	Sex Determining Region Y (SRY)- Box 2
SVZ	Subventricular Zone
SWI/SNF	SWItch/Sucrose Non-Fermentable
TAE buffer	Tris Acetate EDTA buffer
Tam	Tamoxifen
TE buffer	Tris and EDTA buffer
Tris	2-Amino-2-(Hydroxymethyl)Propane-1,3-Diol
TU	Transducing Units
UBC	Unipolar Brush Cell
UK	United Kingdom
UMAP	Uniform Manifold Approximation and Projection for Dimension Reduction
URL	Upper Rhombic Lip
USA	United States of America
UV	Ultraviolet Light
V	Volt(s)
VSV-G	Vesicular Stomatitis Virus
VZ	Ventricular Zone
w	Week(s)
WHO	World Health Organization
WNT	Wingless/Int-1
x g	Force of gravity (9.81 m/s ²)
y	Year(s)

1 INTRODUCTION

1.1 SMARCA4 and the BAF Chromatin Remodeling Complex

1.1.1 Physiological Functions of BAF

The human genome, which counts around three billion base pairs (bp), is tightly condensed to fit into the nucleus of a cell. This compact structure is called chromatin and consists of nucleosomes with 147 bp DNA each wrapped around a histone octamer [1]. The accessibility of chromatin to the binding of proteins largely influences which genes are actively transcribed. This is where chromatin remodeling complexes come into play by altering dense inaccessible heterochromatin to an open state called euchromatin that allows binding of transcription factors to drive gene expression [2, 3]. One of these complexes is the ATP-dependent chromatin remodeling complex BAF (short for BRG1/BRM-associated factor). It is the mammalian equivalent to the SWItch/Sucrose Non-Fermentable (SWI/SNF) complex in yeast, which was discovered in the 1980s for its function in switching of mating type and nutrient source [4, 5]. Only later, it was discovered that SWI/SNF is also responsible for transcriptional activation within the yeast genome [6, 7]. While yeast SWI/SNF is only composed of six subunits, the mammalian BAF complex contains at least 14 subunits. Many of these subunits have paralogues, thus enabling multiple possible BAF assemblies, which are specific to certain tissues or stages in development [8-10]. What remains conserved throughout all BAF complexes is the presence of an ATPase subunit as the catalytic component, which is either SMARCA2 (also known as BRM [BRAHMA]) or SMARCA4 (also known as BRG1 [BRAHMA related gene 1]) [8, 11]. According to the 'loop recapture' model, their mechanism of action is the displacement of DNA from the nucleosome by the formation of DNA loops with a subsequent translocation of the nucleosome alongside the DNA powered by ATP hydrolysis [12-14] (Fig. 1). Consequently, new DNA regions are accessible for the binding of transcription

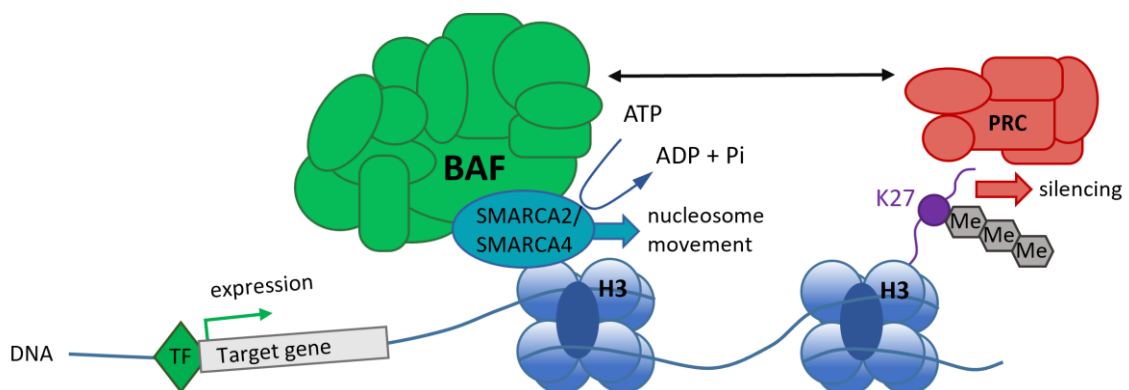


Figure 1. Chromatin remodeling by BAF complexes. The BAF complex binds to nucleosomes and causes changes in DNA accessibility by nucleosome movement, which involves ATP conversion by the catalytic subunit SMARCA2 or SMARCA4. This allows transcription factors (TF) to bind to accessible DNA regions and induce expression of target genes. In contrast to that, the Polycomb Repressive Complex (PRC) contributes to silencing of DNA regions by trimethylation of lysine 27 (K27) on histone H3. Adapted and modified from [12].

factors and active gene expression. Hereby, the BAF complex has opposing functions to the Polycomb Repressive Complex (PRC), which is responsible for the methylation of lysine 27 on histone H3 (H3K27me3), leading to transcriptionally silent chromatin [15, 16]. However, BAF can also contribute to the repression of genes, for instance through the recruitment of histone deacetylases (HDAC), which remove the activating acetyl mark H3K27ac from histone tails [17-19]. Besides this, there are many more discovered interactions with proteins and receptors which underline the far more complex involvement of BAF in gene expression than that of its yeast counterpart SWI/SNF [20-22].

The targeting of chromatin regions by BAF depends on the recognition of binding sequences, the presence of histone modifications, and the assembly of subunits within the complex, which all contain DNA binding domains such as zinc fingers or bromodomains [9, 23, 24]. This explains the varying composition of BAF complexes at different stages of development. In embryonic stem cells (ESCs) for example, chromatin remodeling by the so-called esBAF complex is required for maintaining pluripotency, self-renewal, and proliferation [16, 19]. Later in neural development, when ESCs start differentiating into neural stem cells (NSCs), the neural progenitor BAF (npBAF) complex takes over, which is followed by the next shift to the neuronal BAF (nBAF) complex after mitotic exit of neural progenitors [25-27]. These different types of complexes and their perfectly timed switch are essential to ensure proper neurogenesis and gliogenesis [27, 28]. Similar principles have been described in heart and skeletal muscle development [29-32]. Throughout life, BAF remains indispensable due to its involvement in DNA damage repair [33-35], synaptic plasticity [36], immune response [37], and cell cycle control [18, 38]. Consequently, it is not surprising that alterations in BAF subunits are not only associated with developmental disorders, but also play an important role in tumorigenesis [8, 12, 39].

1.1.2 SMARCA4 Alterations in Cancer

Up to 20% of all human tumors bear a mutation within a subunit of BAF, which places it among the most frequently mutated complexes in cancer. These alterations mostly comprise deleterious/loss of function mutations, hereby suggesting a role of BAF as tumor suppressor [8, 40]. The catalytic subunit SMARCA4 (SWI/SNF related, matrix associated, actin dependent regulator of chromatin, subfamily A, member 4) is one of the most frequently altered BAF subunits across various types of cancer. An example for biallelic loss of *SMARCA4* can be found in small cell carcinoma of the ovary, hypercalcemic type (SCCOHT). SCCOHT is a rare but very aggressive tumor entity, which in contrast to most other ovarian cancers mainly affects young women [41, 42]. Similarly, biallelic losses of *SMARCA4* are detected in around 10-25% of non-small cell lung cancers (NSCLC) and are associated with a significantly worse outcome than *SMARCA4* wildtype NSCLCs [43].

Other entities outside the central nervous system (CNS) affected by *SMARCA4* alterations include pancreatic cancer, hepatocellular carcinoma, and head and neck cancer [40, 44].

Within the CNS, biallelic loss of *SMARCA4* is present in the rare entity of atypical/teratoid rhabdoid tumors (ATRT), a very aggressive brain tumor mainly affecting infants. Most ATRTs carry a biallelic loss of *SMARCB1*, whereas around 2% of patients show a loss of *SMARCA4* instead, making up a molecularly distinct class of tumors with a median survival of only 3 months [45, 46]. Meanwhile, medulloblastomas (MB) are mostly affected by heterozygous missense mutations of *SMARCA4*, which have a dominant-negative effect and result in a loss of function [44] (see section 1.2.4). In contrast, an increased expression of wildtype *SMARCA4* is found in glioblastoma, the most common malignant brain tumor in adults with a median survival of only 15 months [47, 48]. Within this entity, a knockdown of *SMARCA4* significantly reduces invasion and migration potential of tumor cells *in vitro* [49]. Similarly, correlations between high *SMARCA4* expression and poor survival have been discovered in mesothelioma, sarcoma, adrenocortical carcinoma, skin cutaneous melanoma, and acute myeloid leukemia [50-52]. Consequently, the influence of a loss or gain of *SMARCA4* seems to be highly context dependent. This observation contradicts the proposed role of BAF as a tumor suppressor in general and emphasizes the importance to investigate the role of alterations in each tumor entity individually.

Altogether, the mechanism by which *SMARCA4* alterations drive tumor formation is not understood yet. Some studies suggest a pathological effect of the residual BAF complex incorporating *SMARCA2* to compensate for the loss of *SMARCA4* [53, 54]. Although both subunits share 75% sequence homology, their incorporation into BAF is associated with different developmental states and chromatin marks, indicating considerable functional differences [55]. Therefore, an exchange from *SMARCA4* to *SMARCA2* could significantly alter chromatin remodeling and could lead to transformation and selection advantage of tumor cells [53, 54]. This mechanism could be exploited by therapeutic targeting of *SMARCA2* in *SMARCA4*-deficient tumors [56]. Other proposed therapeutic strategies include the inhibition of cyclin-dependent kinase 4/6 (CDK4/6) with efficacy shown in SCCOHT cells *in vitro* and in xenograft mouse models [57]. Xue *et al.* attributed the susceptibility of *SMARCA4*-deficient cells to CDK4/6 inhibition to their reduced level of cyclin D1, which limits CDK4/6 kinase activity and thereby creates a high dependency [57]. Similarly, reduced levels of KDM6A/B demethylases in *SMARCA4*-deficient cells make them especially vulnerable to KDM6A/B inhibition [58].

1.2 Medulloblastoma

1.2.1 Epidemiology and Clinical Features

Medulloblastoma (MB) is a highly aggressive brain tumor that arises in the cerebellum, in the fourth ventricle, or in the dorsal brain stem and is therefore closely linked to hindbrain development [59, 60]. While occurrence in adults is rare, it is the most common malignant brain tumor in childhood with an incidence of around six cases per one million per year in the USA and Western Europe [61-65]. The World Health Organization (WHO) classifies this tumor as grade 4, which indicates the highest degree of malignancy [59]. However, MBs comprise a rather heterogeneous group of tumors with varying characteristics and associated outcomes (see sections 1.2.2 and 1.2.3). The 5-year overall survival (OS) of pediatric MB patients has improved within the last decades, now ranging between 70-80% [66-68]. Nevertheless, this value drops to around 20-40% within high-risk groups [69-71]. Additionally, most survivors suffer from treatment-related morbidities, influencing their quality of life well into adulthood [72, 73].

The treatment of MBs usually comprises surgical resection, craniospinal irradiation (CSI), and extensive chemotherapy. Gross total resection, meaning complete removal of tumor tissue, is desirable but cannot always be achieved, particularly due to risk of surgical complications when tumors are adjacent to critical structures such as the brainstem [74, 75]. The posterior fossa syndrome, also called cerebellar mutism, is a common consequence of tumor resection with symptoms of mild to severe cognitive deficits, speech deficits, and ataxia, occurring in around 20% of patients [74, 76]. CSI on the other hand is very damaging to the developing nervous system, which is why it is mostly withheld in patients under the age of three years after careful consideration of survival benefits against neurocognitive consequences [77-79]. The chemotherapeutic regimen varies between different countries but mainly includes cytostatic drugs such as alkylating agents (e.g. cyclophosphamide, lomustine), microtubule inhibitors (e.g. vincristine), platin derivatives (e.g. cisplatin), topoisomerase inhibitors (e.g. etoposide), and antimetabolites (e.g. methotrexate) [70, 80, 81]. In Germany, Switzerland, and Austria, intrathecal application of methotrexate directly into the brain ventricle system is routinely performed and shows favorable outcome for pediatric MB [68, 82].

Altogether, the aggressive therapy of MB patients results in side effects such as decreased neurocognitive functions, endocrine disorders, growth defects, reduced fertility, and a higher risk for secondary malignancies [72, 83]. Therefore, in recent years, clinical studies have aimed at stratifying patients into high- and low-risk groups to escalate or de-escalate treatment according to the patient's needs. By this, treatment-related morbidities can be reduced in low-risk patients through a reduction of radiation intensity or administration of chemotherapeutics, while high-

risk patients receive an aggressive therapy to increase survival probability [70, 71, 84]. This stratification mostly depends on the presence of certain mutations or classification into molecular subgroups as described in section 1.2.3.

1.2.2 Histological Subgroups

Histologically, MBs can be divided into four classes. Classic MBs are the most frequently encountered group, characterized by densely packed small blue round cells. In some cases, Homer Wright rosettes can be found, displaying radial arrangements of cells around a neuropil region [59, 85]. The desmoplastic/nodular group shows nodules with neuronal differentiation intervened by internodular areas with a more primitive degree of differentiation and a higher proliferation. Desmoplasia describes the pericellular collagen deposition in the internodular area, which can be detected by reticulin deposition [85, 86]. MB with extensive nodularity (MBEN) are a special variant of this group with a bigger proportion of nodules that often fuse together with cells arranged in stream-like patterns [87]. MBENs are associated with a favorable prognosis [68, 88, 89]. The last group, large cell/anaplastic (LCA) MB, shows increased cell size, cytologic pleomorphism, and frequent nuclear molding. Mitotic activity is high and apoptotic bodies are frequently detected [90]. Several studies have confirmed a negative prognostic relevance of the LCA histology compared to the other three histological subtypes [70, 91, 92].

The most recent WHO classification of Tumors of the Central Nervous System (2021) still includes histological subtypes of MB for diagnosis and risk assessment [59, 93]. However, recent advances in molecular analysis of tumors have shifted the focus to the distinction between molecular subgroups, which are described in the next section.

1.2.3 Molecular Subgroups

In 2006, Thompson *et al.* started with a first attempt to distinguish molecular classes of MBs according to their gene expression profiles, hereby identifying five different subgroups A-E within a small cohort [94]. In the following years, publications by Kool *et al.* [95], Cho *et al.* [96], and Northcott *et al.* [97] followed a similar approach, which finally resulted in an international consensus to distinguish four different molecular subgroups of MB [98]: Wingless/Int-1 (WNT), Sonic Hedgehog (SHH), Group 3, and Group 4. The first two were named after characteristically altered signaling pathways in tumor development, while Group 3 and 4 could not be assigned to one single pathway [99]. Due to their similar characteristics that can hamper a clear separation, Group 3 and 4 were summarized as non-WNT/non-SHH MB in the 2016 and 2021 WHO classification [59, 100] (Table 2). Nowadays, the classification of MB into the four molecular subgroups is routinely performed by global DNA methylation analysis and subsequent upload to the brain tumor classifier developed by Capper *et al.* in 2018 [101]. Compared to gene expression profiling, this method

benefits from higher stability of DNA, which also allows analysis of low-quality samples and archived biopsy material derived from FFPE tissue [102].

Table 2. MB subgroups according to the WHO classification of tumors of the central nervous system 2021 [59, 93]

Medulloblastoma, molecularly defined
Medulloblastoma, WNT-activated
Medulloblastoma, SHH-activated & <i>TP53</i> wild-type
Medulloblastoma, SHH-activated & <i>TP53</i> mutant
Medulloblastoma, non-WNT/non-SHH
Medulloblastoma, histologically defined
Classic medulloblastoma
Desmoplastic nodular medulloblastoma
Medulloblastoma with extensive nodularity
Large cell/anaplastic medulloblastoma








Characteristics of the four molecular MB subgroups are summarized in table 3. WNT MBs make up the smallest subgroup and show a classic morphology and very good prognosis with a median 5-year OS of 90-100% [70, 103]. Tumors typically expand into the fourth ventricle with involvement of the cerebellar peduncle and brain stem [104]. They are proposed to originate from progenitor cells in the lower rhombic lip [105]. All cases show a constitutive activation of WNT signaling, which is caused by hotspot mutations in the β -catenin gene *CTNNB1* in the vast majority (95%) [70, 106]. These mutations stabilize β -catenin, which can subsequently enter the nucleus to drive expression of WNT targets such as MYC and cyclin D1 to promote tumor cell proliferation [107]. Additionally, loss of chromosome 6 (monosomy 6) is a common feature of WNT MB [70, 106]. Several clinical studies aim at treatment de-escalation for children harboring these low-risk tumors with reduced doses in radiation and chemotherapy [84, 108, 109].

SHH MBs show a good to intermediate prognosis (median 5-year OS 73-83%) and often display desmoplastic or MBEN histology [68, 70]. They are characteristically localized within the hemispheres of the cerebellum and originate from granule cell precursors (GCPs) of the external granular layer [110, 111]. In these tumors, mutations of *PTCH1*, *SMO*, or *SUFU* or amplification of *GLI1/2* lead to the activation of the SHH signaling pathway [106]. Other recurrent events include germline mutations in elongator complex protein 1 (*ELP1*) or somatic mutations in the telomerase reverse transcriptase (*TERT*) [112, 113]. An additional mutation of tumor suppressor p53 (*TP53*) is associated with a worse prognosis, which is why SHH MBs *TP53* wildtype and *TP53* mutant are listed separately in the WHO classification [70, 114] (Table 2).

Group 3 MBs account for 25% of MB cases and mainly affect younger children and infants with a male predominance. They can display classic or LCA histology and are often already metastasized at diagnosis [115]. Group 3 MBs show the worst prognosis of all subgroups with a median 5-year OS below 60% [70, 116]. Tumors are typically localized in the cerebellar midline (vermis) with involvement of the fourth ventricle [110, 111]. The cell of origin has been thoroughly discussed and is currently suggested to reside in a species-specific cell population in the developing human rhombic lip [117] (see discussion). Recurrent alterations in Group 3 MBs include *MYC* amplifications in 15-20% of cases, which correlate with poor survival [70, 116, 118]. Furthermore, amplifications of *MYCN* or mutations of *SMARCA4* or *KBTBD4* are among the most frequently detected alterations [70, 106, 119]. Other recurrent events are chromosomal rearrangements resulting in the positioning of *GFI1* or *GFI1B* next to an active enhancer driving their expression, a phenomena called ‘enhancer hijacking’ [120].

Group 4 MBs make up the biggest molecular subgroup with an intermediate prognosis (median 5-year OS 75-80%) and high male predominance [70, 121]. Histology is mainly classic with a few LCA cases, and localization is similar to that described for Group 3 MB [70, 110]. Comparisons to single-cell RNA sequencing data of the developing mouse brain have suggested a cellular origin of Group 4 MB in the unipolar brush cell (UBC) lineage [60]. However, recent findings point towards a shared origin of Group 3 and 4 MB in the subventricular zone of the developing human rhombic lip [117, 119].

Table 3. Characteristics of molecular MB subgroups, adapted from Juraschka and Taylor, 2019 [115] and updated according to recent publications [70, 112, 117, 119]

MB Subgroup	WNT	SHH	Group 3	Group 4
% of MB cases	10	30	25	35
Age  infant  child  adult				
Sex ratio (m:f)	1:1	1:1	2:1	3:1
Anatomic location	4th ventricle, cerebellar peduncle	cerebellar hemisphere	midline, adjacent to 4th ventricle	midline, adjacent to 4th ventricle
Histology	classic, rarely LCA	desmoplastic, MBEN, classic, LCA	classic, LCA	classic, rarely LCA
Metastasis at diagnosis	5-10 %	15-20 %	40-45 %	35-40 %
Prognosis	very good	infants good, others intermediate	poor	intermediate
Proposed cell of origin	progenitor cells in the lower rhombic lip	granule cell precursors	human rhombic lip progenitors	human rhombic lip progenitors
Recurrent mutations	<i>CTNNB1</i> , <i>DDX3X</i> , <i>SMARCA4</i> , <i>TP53</i>	<i>PTCH1</i> , <i>SMO</i> , <i>SUFU</i> , <i>TP53</i> , <i>TERT</i> , <i>ELP1</i>	<i>SMARCA4</i> , <i>KBTBD4</i>	<i>KDM6A</i> , <i>KBTBD4</i> , <i>ZMYM3</i> , <i>KMT2C</i>
Recurrent amplifications	–	<i>MYCN</i> , <i>GLI1</i> or <i>GLI2</i>	<i>MYC</i> , <i>MYCN</i> , <i>OTX2</i>	<i>SNCAIP</i> , <i>MYCN</i> , <i>OTX2</i> , <i>CDK6</i>
Other recurrent events	chromosome 6 loss	–	<i>GFI1(B)</i> enhancer hijacking	<i>PRDM6</i> or <i>GFI1(B)</i> enhancer hijacking

Since the definition of the four molecular MB subgroups, several researchers have attempted to define further intra-subgroups to address heterogeneity within the subgroups, especially concerning non-WNT/non-SHH MB [106, 116, 122]. In 2019, Sharma *et al.* tried to reconcile these findings by integrating DNA methylation data from 1,051 patients with non-WNT/non-SHH MB [123]. They were able to divide these MB into eight stable molecular subtypes, namely I-VIII. Each of these subtypes is associated with distinct clinical features, cytogenetic events, molecular drivers, and survival of patients. Some subtypes only contain Group 3 MBs (II, III, IV), others only Group 4 MBs (VI, VIII), but the remaining subtypes I, V, and VII include a mixture of Group 3 and 4, which again indicates a shared biology of both subgroups. Risk stratification of patients according to these eight molecular subtypes has been proposed for future clinical trials [71].

1.2.4 SMARCA4 Alterations in Medulloblastoma

SMARCA4 mutations are among the most commonly detected alterations in MB. They frequently occur in the molecular subgroups WNT (~20% of patients) and Group 3 (9-15%) but also show rare occurrence in SHH and Group 4 MB (1-2%) [70, 106]. Within the eight subtypes of Group 3/4 MB described by Sharma *et al.* [123], *SMARCA4* mutations mostly occur in subtype II, which is also enriched for *MYC* amplifications. *SMARCA4* mutations are mainly somatic heterozygous missense mutations that are broadly distributed along the catalytic core (helicase and ATPase chain) of the protein (Fig. 2). WNT and Group 3 MB harbor similar *SMARCA4* mutations and show no specificity for certain variants or affected regions [70, 106, 124-129]. *In vitro* studies revealed that these missense mutations either hinder binding of *SMARCA4* to the DNA (DNA groove mutants) or prevent subsequent ATP hydrolysis to execute its catalytic activity [43, 44]. Consequently, DNA accessibility at enhancer sites is reduced and PRCs accumulate across the genome [44, 130]. In contrast, a heterozygous knockdown of *SMARCA4* does not influence chromatin remodeling, which hints towards a dominant-negative effect of the missense mutation instead of haploinsufficiency causing this phenotype [44]. Nevertheless, it is not clear in which way altered chromatin remodeling caused by dysfunctional *SMARCA4* specifically affects MB development. A recent study by Ballabio *et al.* showed that overexpression of *SMARCA4* wildtype in a Group 3 MB mouse model significantly increases survival [131]. This effect was not seen when the mutated variant *SMARCA4* T910M was concurrently expressed, again confirming a dominant-negative effect on the wildtype allele. However, the generation of a tumor model bearing loss of *SMARCA4* or mutated *SMARCA4* as an oncogenic driver was not successful [131].

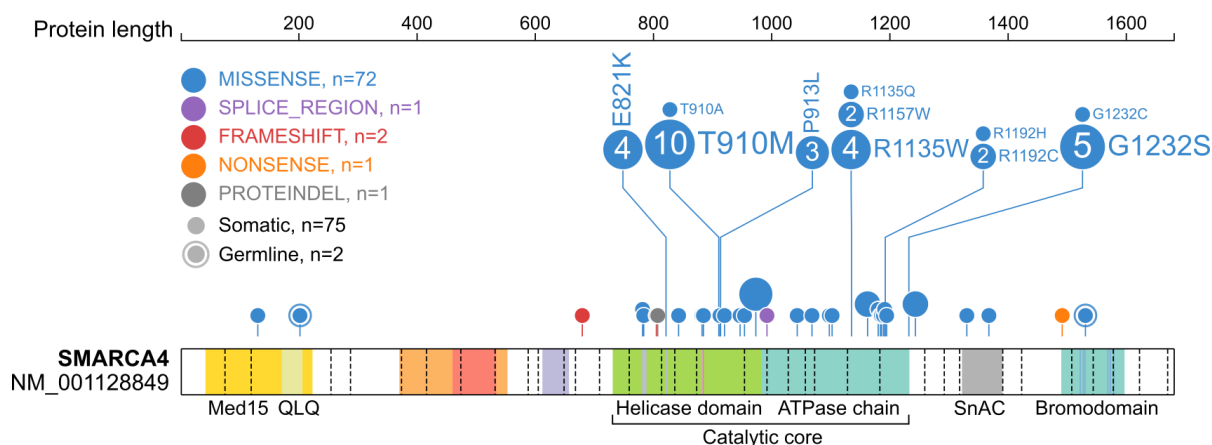


Figure 2. Mutational landscape of SMARCA4 in MB. Lollipop plot depicting previously identified and published mutations of *SMARCA4* in MBs (all four molecular subgroups included) [70, 106, 124-129]. The plot was generated by manual upload to the St Jude’s Protein Paint platform (<https://proteinpaint.stjude.org/>). Mutations are mainly somatic missense mutations located in the catalytic core (helicase domain and ATPase chain) of the protein. The size of bubbles and numbers within correspond to the number of identified cases. Other rarely affected protein domains include Med15 = subunit of mediator complex non-fungal, QLQ = glutamine-leucine-glutamine domain, SnAC = Snf2 ATP coupling, and the bromodomain.

1.3 Mouse Models

1.3.1 Hindbrain Development in Mice

Humans and rodents display major evolutionary conservation of brain architecture, which makes mouse models a valuable tool for understanding neurodevelopmental processes. During early embryonic development in mice, neuroepithelial cells derived from the neuroectoderm form the neural plate, which then bends and fuses to form the neural tube, a process called neurulation [132]. The first segmentation of brain areas is evident at embryonic day 9.5 (E9.5), when the anterior part of the neural tube forms three primary brain vesicles: the forebrain (prosencephalon), mid-brain (mesencephalon), and hindbrain (rhombencephalon) (Fig. 3A). Meanwhile, the caudal part of the tube retains its shape to build the spinal cord [132, 133]. The hindbrain is segmented into rhombomeres 0-11 (r0-r11), of which r0 and r1 later give rise to the cerebellum (Fig. 3B). The

most anterior rhombomere r0 is also known as the isthmus and is responsible for stabilizing the mid-hindbrain boundary from E11.5 onwards [134, 135].

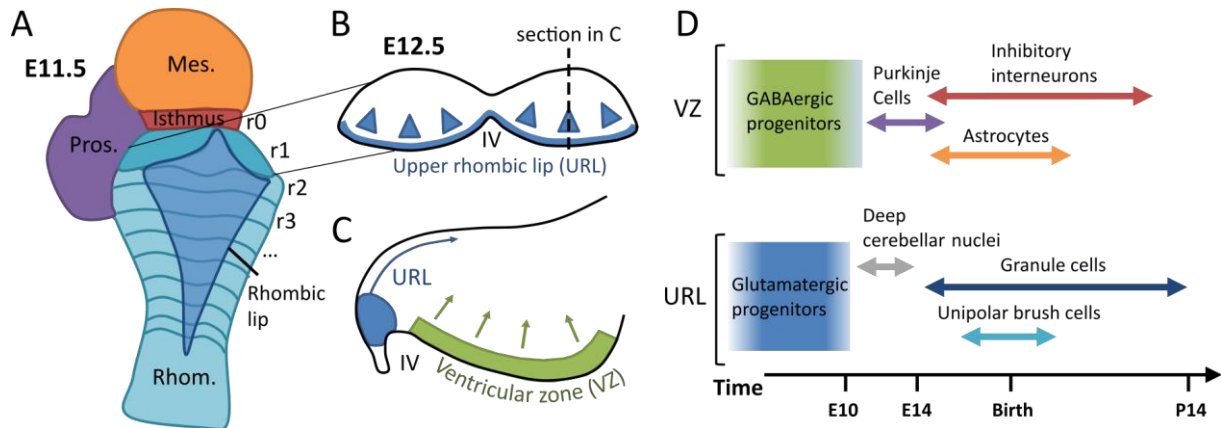


Figure 3. Embryonic hindbrain development in mice. (A) Rear view on an embryonic hindbrain at E11.5 shows the three primary brain vesicles prosencephalon (Pros.), mesencephalon (Mes.), and rhombencephalon (Rhomb.). The rhombencephalon is divided into 11 rhombomeres, of which r0/the isthmus is responsible for stabilizing the mid-hindbrain boundary. (B) Sagittal view on the developing cerebellum at E12.5 shows the upper rhombic lip (URL) and migration patterns of developing precursors. (C) Coronal section of the developing cerebellum at E12.5 shown in (B) with the second germinal zone, the ventricular zone (VZ). (D) Respective cell populations developing from the two germinal zones in the cerebellum. IV: fourth ventricle. Adapted and modified from [135, 136].

At E12.5, two distinct germinal zones in the developing cerebellum can be distinguished, which give rise to all diverse cell types that make up the mature cerebellum: The ventricular zone (VZ) and the upper rhombic lip (URL) (Fig. 3C) [137]. The VZ forms the ventral lining of the cerebellum adjacent to the fourth ventricle (IV) and gives rise to all inhibitory (GABAergic) neuronal progenitors and glial lineages, including Purkinje cells, inhibitory interneurons, Bergmann glia, and other types of astrocytes. These distinct populations start differentiating at specific embryonic or post-natal points in time while radially migrating inside the cerebellum. In contrast to that, the upper rhombic lip (URL) gives rise to excitatory (glutamatergic) neuronal progenitors, which then further differentiate into deep cerebellar nuclei, unipolar brush cells, or granule cells, which later make up the major cell population in the mature cerebellum (Fig. 3D) [136]. Granule cell precursors (GCPs), evolving between E12.5-E16.5 from the URL, migrate tangentially across the surface of the cerebellum, where they form another transient germinal zone, the external granular layer (EGL). Here, proliferation and vast clonal expansion of GCPs is driven by Sonic Hedgehog (SHH) protein secreted by Purkinje cells [134, 138]. After birth, GCPs gradually start to exit the cell cycle and migrate inwards along the fibers of Bergmann glia cells to form the internal granular layer (IGL) as mature granule neurons. This migration is completed at around three weeks of age in mice or after the first year of life in humans [134].

Finally, the mature cerebellum displays four distinct layers (Fig. 4A): The outermost molecular layer is cell-poor and mainly contains axons and dendrites of granule cells and Purkinje cells. Beneath lies the Purkinje cell layer as a monolayer of Purkinje cell somata, followed by the IGL, which is populated by a large number of granule cells. Each of these three cellular layers additionally contains distinct populations of inhibitory interneurons. Lastly, the white matter builds the innermost layers with deep cerebellar nuclei and fibers connecting to other brain areas [139-141]. Macroscopically, the mature cerebellum in mice is subdivided into ten lobes divided by fissures (Fig. 4B). The vermis builds the midline of the cerebellum connecting the two hemispheres (Fig. 4C) [140].

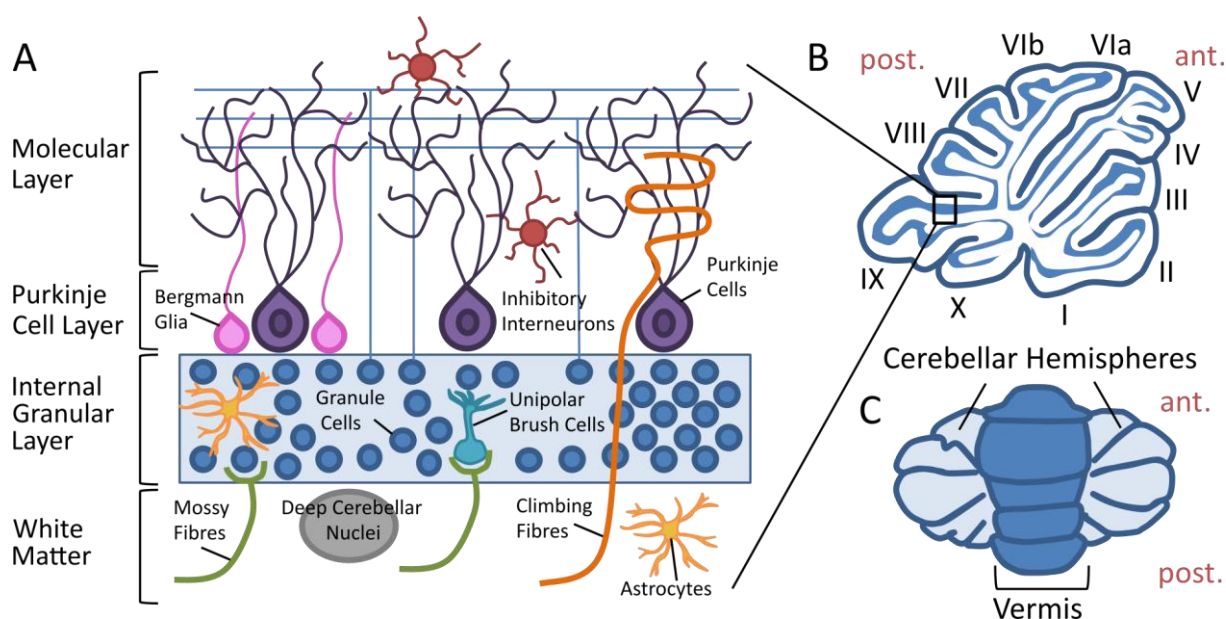


Figure 4. Structure and layering of the mature murine cerebellum. (A) Layering and location of different neural cell populations in the mature murine cerebellum based on findings in [137, 139, 140]. (B) Sagittal view on the mature cerebellum shows the presence of ten lobes (I-X) counting from the anterior (ant.) to the posterior (post.) parts. (C) Top view on the cerebellum shows the division of the cerebellum into two hemispheres separated by the vermis in the midline.

1.3.2 Modeling Disease in Mice

Due to their high biological similarity to the human organism and easy handling, transgenic mouse models are a helpful tool to model tumor-specific gene modifications and investigate tumor origins and therapy options [142, 143]. Within the last 40 years, the cre/loxP (cyclization recombinase/ locus of X [cross]- over P1) system has been widely used to knock out genes in the murine genome or to introduce the expression of transgenes. This system makes use of the cre recombinase, an enzyme which recognizes 34 bp DNA sequences (so-called loxP sites) and catalyzes the recombination between these sites [144-146]. When loxP sites are introduced flanking an essential exon of a target gene (therefore called a *floxed* gene), cre recombination leads to a knockout

of the respective gene. Similarly, new transgenes with an upstream stop cassette flanked by loxP sites can be introduced. In this case, the stop cassette is excised upon cre recombination, allowing active expression of the transgene [147, 148].

In *Blbp-cre* mice used in this study, cre activity is coupled to the expression of the brain lipid binding protein (BLBP), which is present in neural progenitor cells during CNS development [105, 149]. Consequently, breeding of the *Blbp-cre* strain with mice bearing floxed (fl) *Smarca4* (*Smarca4^{fl/fl}*) alleles results in a specific knockdown of *Smarca4* in BLBP-expressing cells.

For a time-controlled activation of the knockdown, cre can be coupled to a mutated estrogen receptor in cre-ERT2 mouse strains. As this mutated receptor needs hydroxy-tamoxifen as a ligand to enter the nucleus, it can only act at loxP sites after administration of tamoxifen [150]. This principle is applied in *Math1cre-ERT2::Smarca4^{fl/fl}* mice used in this study to introduce a tamoxifen-dependent recombination of *Smarca4* in GCPs at defined time points [151].

To track cells and their progeny after successful recombination, different strains of so-called ‘fate mapping’ mice have been developed. These mice carry a floxed stop cassette between the gene of a fluorescent protein and a strong promoter coupled to an ubiquitously expressed locus, for example the red fluorescent protein (RFP) driven by the *Rosa26* locus in *lsIR26tdRFP^{fl/fl}* mice. When bred with a cre strain, all cells expressing cre at some time point in development are permanently labelled by RFP expression and pass this feature on to their progeny [152, 153].

Despite its big range of applications in biomedical research, the cre loxP system also has its limitations. Expression of cre on its own can induce toxicity in cell lines and causes metabolic phenotypes in *Nestin-cre* mice by off-target recombination [154, 155]. Secondly, unexpected expression of cre outside of desired cell types or even within the germline can largely influence phenotypes and must be carefully accounted for [156, 157]. In case of inducible cre systems, so-called ‘cre leakiness’ can result in weak expression of cre and thus unwanted recombination without tamoxifen administration [158, 159]. Moreover, tamoxifen injections can cause severe side effects such as uterine inertia in pregnant mice [160]. Lastly, the use of different genetic backgrounds (e.g. *C57BL/6* or *FVB*) can affect the degree of recombination and resulting phenotypes [161, 162]. Taken together, great care and diligent phenotyping and genotyping is needed to ensure a proper use of the cre loxP system, thus enabling the generation of reproducible and well-characterized mouse models.

1.3.3 SMARCA4-Deficient Mouse Models

Several mouse models have investigated the influence of a SMARCA4 deficiency on brain development in mice. Altogether, a homozygous loss of SMARCA4 mostly resulted in early lethality or severe developmental phenotypes [163-165]. When the *Smarca4* locus is inactivated by homologous recombination in embryonic stem cells, blastocysts already die during the peri-implantation step, suggesting indispensability of the protein in early embryonic development [163]. Meanwhile, a similar inactivation of the paralogue *Smarca2* at embryonic stage results in viable mice without any evident phenotype except for slightly increased weight [166].

SMARCA4 loss in NSCs of *Nestin-cre::Smarca4^{fl/fl}* mice with active cre expression from E10.5 on leads to reduced brain size, hypoplastic cerebella, and a thinned cortex [164]. Due to their inability to breathe, *Nestin-cre::Smarca4^{fl/fl}* mice die at birth. SMARCA4-deficient NSCs derived from these mice show a highly reduced ability for astrocytic differentiation, suggesting an important role of SMARCA4 in gliogenesis [164]. A homozygous loss of SMARCA4 in *hGFAP-cre::Smarca4^{fl/fl}* mice yields viable mice but otherwise similar phenotypes, including hydrocephalus, hypoplastic cerebella, and underdeveloped cortices and hippocampi, resulting in a median survival of only two weeks [165]. Hypoplastic cerebella and disturbed cortical layering are also evident in *Math1-cre::Smarca4^{fl/fl}* mice with a more specific loss of SMARCA4 in GCPs [167]. On the other hand, an induced loss at postnatal day 3 (P3) in *Math1-creER^{T2}::Smarca4^{fl/fl}* does not impair cerebellar architecture [168], highlighting the time-dependent importance of SMARCA4 in cerebellar development. When a loss of SMARCA4 is induced in *Sox2-creER^{T2}::Smarca4^{fl/fl}* mice by tamoxifen injections between E6.5 and E14.5, the effects on brain development are also highly dependent on the time of induction. While an induction of SMARCA4 loss at E6.5 or E14.5 does not cause evident alterations in embryonic brain development, a deletion between E7.5 to E12.5 results in severe architectural alterations in the brain, including rosette-like structures in the subventricular zone and enlarged neural retina [169]. A loss of SMARCA4 can also affect the peripheral nervous system, which was highlighted by a *p0-cre::Smarca4^{fl/fl}* mouse model showing neuromuscular weakness and paralysis of limbs from the age of 1-3 months on [170].

In contrast, a heterozygous loss of SMARCA4 driven by the various cre drivers mentioned before does not induce any phenotype in the brain, indicating the sufficiency of one *Smarca4* allele for normal CNS development. However, SMARCA4 heterozygotes show increased susceptibility for mammary tumors and lung cancer [171, 172].

Taken together, all these studies support a high significance of SMARCA4 in nervous system development, but do not address the tumorigenic mechanism behind *Smarca4* alterations in the CNS.

To our knowledge, until now, attempts at modelling SMARCA4-deficient brain tumors like ATRT or MB in mice have not been successful.

1.3.4 WNT Medulloblastoma Models

In 2010, the first mouse model for WNT MBs was described by Gibson *et al.*, suggesting a tumor origin in the lower rhombic lip [105]. They used *Blbp-cre::Ctnnb1(ex3)^{fl/wt}::Trp53^{fl/fl}* mice, which carry a stabilizing β -catenin (*Ctnnb1*) mutation to activate WNT signaling, combined with a loss of tumor suppressor p53 (*Trp53*). The resulting tumors originate from the dorsal brain stem and show similar gene expression patterns as their human counterpart. However, tumors develop at a penetrance of only 15% with earliest tumor detection at the age of eight months. This issue was addressed two years later, when the group additionally introduced an activating mutation of *Pik3ca* (phosphatidylinositol 3-kinase) in *Blbp-cre::Ctnnb1(ex3)^{fl/wt}::Trp53^{fl/fl}::Pik3ca^{fl/wt}* mice. This adjustment resulted in MB development with 100% penetrance and significantly reduced latency [127]. Although mutations of *TP53* or *PIK3CA* occur in WNT MB patients (each at a frequency of 5-10%), the combination of both alterations has not been detected throughout several MB cohorts, which could limit practicality of this model [106, 173]. To our knowledge, no further WNT MB mouse models have been described so far. Consequently, the effect of frequently altered *SMARCA4* in WNT MB has not been investigated in any mouse model yet.

1.3.5 Group 3 Medulloblastoma Models

Many groups have attempted to model Group 3 MB in mice within the last 13 years, following different technical approaches as well as using a broad range of cellular origins (detailed list in Suppl. Table 1). The first model developed in 2010 used an amplification of *MYCN* in hindbrain progenitors to generate tumors in a genetically engineered mouse model (GEMM) which is now known as the GTML model [174]. Tumors displayed similarities to aggressive MB with either classic or LCA histology and were later designated as Group 3 MB [175]. However, *MYCN* is a far less common driver than *MYC* in Group 3 MB patients, which is why future models focused on modeling *MYC* alterations. One of the first *MYC*-induced tumor models by Kawauchi *et al.* was generated by transplanting p53-deficient and *MYC* transduced GCPs into the cerebella of *CD1^{nu/nu}* mice [176]. Resulting tumors showed similar gene expression profiles as *MYC*-driven MBs and harbored neoplastic potential in serial transplantations. A few years later, the same group used *in utero* electroporation to show that the combination of a p53 loss and *MYC* overexpression is able to drive MB formation in several different neural progenitor populations in mice, including multipotent cerebellar stem cells and inhibitory interneurons [177]. However, alterations in *TP53* are not common in primary tumors of Group 3 MB patients. Therefore, Ballabio *et al.* combined overexpression of *MYC* and overexpression of either *GFI1* or *OTX2* using the PiggyBac transposon system.

Both combinations resulted in tumor formation with histology and methylation signatures resembling Group 3 MB [131]. On the other hand, recent publications have demonstrated that formation of Group 3-like MB can be achieved by MYC amplification only. Tao *et al.* transplanted lentivirally MYC-transduced SOX2-positive cerebellar progenitors into immunodeficient brains to successfully drive MB formation [178]. Meanwhile, Mainwaring *et al.* generated a GEMM driving MYC overexpression in hindbrain progenitors as an equivalent to the GTML model [179]. Few mouse models for Group 3 MB were developed without using MYC as a driver. Dhar *et al.* induced tumor formation by *Kmt2d* knockdown in NSCs, whereas Vo *et al.* used random aberrations induced by the Sleeping Beauty Transposase system [180, 181]. Altogether, the targeting of divergent cell populations within all of these studies shows that there are still many open questions regarding the biology and especially the origin of Group 3 MB. Moreover, none of these mouse models include alterations of *Smarca4*, which is one of the most frequently altered genes in Group 3 MB patients and the function of which still needs to be revealed.

1.4 Aim of this Work

The aim of this work was to decipher the role of *SMARCA4* alterations in the development of MB. Although *SMARCA4* is one of the most frequently altered genes in both WNT and Group 3 MB, the functional significance of these alterations remains unclear [70, 106]. Until now, no mouse model or cell line has demonstrated how a mutation or loss of *SMARCA4* contributes to tumorigenesis within these subgroups. Therefore, we aimed at elucidating tumor-driving mechanisms of mutant *SMARCA4* by using both *in vitro* and *in vivo* models.

In a first approach, we generated lentiviral constructs to induce overexpression of *SMARCA4* variants T910M and R1135W, which were previously identified in MB patients [106, 126]. By transduction of both MB cell lines and primary neural cells, we wanted to investigate the influence of altered *SMARCA4* on cell viability and proliferation. Although both *SMARCA4* variants are suggested to induce a loss of function, residual activity might be present and influence observed phenotypes [182]. Therefore, we intended to compare the effects of overexpressed variants to a complete *SMARCA4* knockdown induced by small hairpin RNA (shRNA) in the same setting.

Moreover, we aimed at developing new mouse models recapitulating the biology of *SMARCA4* altered MB by following two different technical approaches: First, we focused on developing a *SMARCA4*-deficient Group 3 MB model by orthotopic transplantation. So far, mouse models have convincingly demonstrated a tumor-driving role of *MYC* in the development of Group 3 MB [176-178]. However, none of the models include alterations of *SMARCA4*, which is among the most frequently altered genes in this subgroup. Therefore, we combined *MYC* overexpression with a loss of *SMARCA4* in GCPs, which we transplanted into immunodeficient mice. By this, we intended to establish the first *SMARCA4*-deficient Group 3 MB mouse model in hope to elucidate the contributions of *SMARCA4* to tumor development as a basis to identify new therapeutic targets.

Secondly, we modified a previously published WNT MB mouse model by combining a β -catenin mutation with a loss of *SMARCA4* in *Blbp-cre::Ctnnb1(ex3)^{fl/wt::Smarca4^{fl/fl}}* mice [105]. Concurrent mutations of *CTNNB1* and *SMARCA4* or other chromatin modifiers are common within this subgroup, which hints towards cooperative effects between both alterations. Consequently, we intended to develop a mouse model with the potential to study both tumor origin and tumor-driving mechanisms attributed to disturbed chromatin remodeling in WNT MB.

Taken together, this work aimed at clarifying how *SMARCA4* alterations contribute to MB development while taking into account both biological differences between molecular subgroups and the type of mutation.

2 MATERIALS AND METHODS

2.1 Materials

All materials were provided by the laboratory facilities of the Research Institute Children's Cancer Center Hamburg, the Institute of Neuropathology at the University Medical Center Hamburg-Eppendorf, and the Leibniz Institute of Virology, Hamburg.

2.1.1 Chemicals, Media, and Reagents

Table 4. List of chemicals, media, and reagents used in this study

Item	Manufacturer
7-AAD Viability Staining Solution	Invitrogen, Thermo Fisher Scientific Inc, USA
Accutase (StemPRO)	Thermo Fisher Scientific Inc, USA
Agar	Carl Roth GmbH & Co KG, Germany
Agarose	Biozym Scientific GmbH, Germany
Ampicillin	Sigma-Aldrich, Merck KGaA, Germany
Antiseptic (Braunol®)	B. Braun SE, Germany
Aqua ad ini (Ampuwa®)	Fresenius SE & Co KGaA, Germany
B27™ Supplement	Thermo Fisher Scientific Inc, USA
BamHI Restriction Enzyme (Fast Digest)	Fermentas, Thermo Fisher Scientific Inc, USA
Borax (anhydrous)	Sigma-Aldrich, Merck KGaA, Germany
BrdU	Sigma-Aldrich, Merck KGaA, Germany
BSA (Albumin Fraction V)	Carl Roth GmbH & Co KG, Germany
CaCl ₂	Carl Roth GmbH & Co KG, Germany
Carprofen (Rimadyl, 50 mg/mL)	Zoetis Inc, USA
Clarity Western ECL Substrate	Bio-Rad Laboratories Inc, USA
Corn Oil	UKE Apotheke, Germany
DAPI (4',6-Diamidino-2-Phenylindol)	Sigma-Aldrich, Merck KGaA, Germany
DEPC	Carl Roth GmbH & Co KG, Germany
D-Glucose	Carl Roth GmbH & Co KG, Germany
DMEM + 4.5 g/L D-Glucose, L-Glutamine	Gibco, Thermo Fisher Scientific Inc, USA
DMEM/F-12 (1:1) + GlutaMAX	Gibco, Thermo Fisher Scientific Inc, USA
DMSO (Dimethyl Sulfoxide)	Carl Roth GmbH & Co KG, Germany
DNA Ladder Gene Ruler 1 kb	Thermo Fisher Scientific Inc, USA
DNA Ladder Gene Ruler 100 bp plus	Thermo Fisher Scientific Inc, USA
DNase I (Grade II)	Roche AG, Switzerland
dNTPs (25 μmol each)	Promega Corporation, USA
DPBS (without CaCl ₂ and MgCl ₂)	Gibco, Thermo Fisher Scientific Inc, USA
DTT (Dithiothreitol)	Carl Roth GmbH & Co KG, Germany

Item	Manufacturer
EDTA	Carl Roth GmbH & Co KG, Germany
EGF (recombinant, human)	PeproTech Inc, Thermo Fisher Scientific Inc, USA
Eosin	Merck KGaA, Germany
Ethanol (99%, denatured)	Th. Geyer GmbH & Co KG, Germany
Ethidium bromide (10 mg/mL)	Carl Roth GmbH & Co KG, Germany
Eye Ointment (Bepanthen)	Bayer AG, Germany
Fast Alkaline Phosphatase	Fermentas, Thermo Fisher Scientific Inc, USA
Fast Digest Green Buffer (10x)	Fermentas, Thermo Fisher Scientific Inc, USA
FCS (Fetal Calf Serum)	Gibco, Thermo Fisher Scientific Inc, USA
FGF (recombinant, human)	PeproTech Inc, Thermo Fisher Scientific Inc, USA
Formaldehyde (4%)	Grimm med Logistik GmbH, Germany
Glacial Acetic Acid	Carl Roth GmbH & Co KG, Germany
Glycine	Carl Roth GmbH & Co KG, Germany
HBSS (10x Stock)	Gibco, Thermo Fisher Scientific Inc, USA
HCl (37% Stock)	Merck KGaA, Germany
Hematoxylin	Carl Roth GmbH & Co KG, Germany
HEPES	Gibco, Thermo Fisher Scientific Inc, USA
Isoflurane	Baxter International, USA
Isopropanol	Th. Geyer GmbH & Co KG, Germany
KCl (2M)	Invitrogen, Thermo Fisher Scientific Inc, USA
LDS Sample Buffer (NuPAGE™)	Thermo Fisher Scientific Inc, USA
L-Glutamine	Life Technologies, Thermo Fisher Scientific Inc,
Lidocaine (Xylocitin-Loc 2%)	Mibe GmbH Arzneimittel, Germany
MEM Non-essential Amino Acids (100 x)	Gibco, Thermo Fisher Scientific Inc, USA
MES SDS Running Buffer (NuPAGE) (20x)	Thermo Fisher Scientific Inc, USA
Methanol	Carl Roth GmbH & Co KG, Germany
MgCl ₂	Merck KGaA, Germany
Milk Powder	Carl Roth GmbH & Co KG, Germany
Mowiol (4-88)	Carl Roth GmbH & Co KG, Germany
Na ₂ EDTA	Sigma-Aldrich, Merck KGaA, Germany
Na ₂ HPO ₄	Sigma-Aldrich, Merck KGaA, Germany
NaCl	Carl Roth GmbH & Co KG, Germany
NaCl solution (0.9%) for injection	B. Braun SE, Germany
NaOH	Carl Roth GmbH & Co KG, Germany
NGS (Normal Goat Serum)	Merck KGaA, Germany
PAP Pen	Life Technologies, Thermo Fisher Scientific Inc,
Papain Dissociation System (PDS Kit)	Worthington Biochemical Corporation, USA
Paraffin	Sakura FineTek Europe, The Netherlands
PFA (Paraformaldehyde)	Carl Roth GmbH & Co KG, Germany

Item	Manufacturer
PCR buffer (GoTaq® Green, 5x)	Promega Corporation, USA
Penicillin/Streptomycin (5.000 U/mL)	Gibco, Thermo Fisher Scientific Inc, USA
PLO (Poly-L-Ornithine)	Sigma-Aldrich, Merck KGaA, Germany
Polybrene	Sigma-Aldrich, Merck KGaA, Germany
Protamine sulfate (from salmon, grade x)	Sigma-Aldrich, Merck KGaA, Germany
Protease Inhibitor Cocktail (100x)	Thermo Fisher Scientific Inc, USA
Protein Ladder Page Ruler Plus	Thermo Fisher Scientific Inc, USA
Protein Ladder Spectra Multicolor High Range	Thermo Fisher Scientific Inc, USA
Proteinase K	Carl Roth GmbH & Co KG, Germany
RPMI-1640	Gibco, Thermo Fisher Scientific Inc, USA
SDS	Carl Roth GmbH & Co KG, Germany
SDS Gel (NuPAGE™ 4-12% Bis Tris Gel)	Thermo Fisher Scientific Inc, USA
SHH Protein	Self-made, see section 2.4.8.1
Sodiumdeoxycholate	Merck KGaA, Germany
T4 Ligase	Thermo Fisher Scientific Inc, USA
T4 Ligase Buffer (10x)	Thermo Fisher Scientific Inc, USA
TAE-Buffer (50x)	AppliChem GmbH, Germany
Tamoxifen	Sigma-Aldrich, Merck KGaA, Germany
Taq Polymerase (GoTaq® G2)	Promega Corporation, USA
Tissue Adhesive (Surgibond)	SMI AG, Belgium
Trisodium Citrate Dihydrate	Carl Roth GmbH & Co KG, Germany
Tris (Base)	Carl Roth GmbH & Co KG, Germany
Tris-Hydrochloride (Tris-HCl)	Sigma-Aldrich, Merck KGaA, Germany
Triton X®-100	Carl Roth GmbH & Co KG, Germany
Trypan Blue Solution (0.4%)	Gibco, Thermo Fisher Scientific Inc, USA
Trypsin/EDTA (0.25%)	Gibco, Thermo Fisher Scientific Inc, USA
Tryptone	Carl Roth GmbH & Co KG, Germany
Tween®20	Sigma-Aldrich, Merck KGaA, Germany
XhoI Restriction Enzyme (Fast Digest)	Fermentas, Thermo Fisher Scientific Inc, USA
Xylol	Th. Geyer GmbH & Co KG, Germany
Yeast Extract	Carl Roth GmbH & Co KG, Germany
Zeocin™	Thermo Fisher Scientific Inc, USA

2.1.2 Assays and Kits

Table 5. List of assays and kits used in this study

Item	Manufacturer
Cell Titer Glo® Luminescent Cell Viability Assay	Promega Corporation, USA
Chromium Next GEM Single Cell 3' v3.1	10x Genomics, Inc., USA

Item	Manufacturer
CORALL Total RNA-seq V2	Lexogen GmbH, Austria
DC™ Protein Assay	Bio-Rad Laboratories Inc, USA
EZ DNA Methylation Kit	Zymo Research, USA
High Sensitivity D5000 ScreenTape®	Agilent Technologies, USA
Infinium™ Mouse Methylation BeadChip	Illumina, USA
iView™ DAB Detection Kit	Roche AG, Switzerland
Maxwell® RSC DNA FFPE Kit	Promega Corporation, USA
Nucleo Spin® Tissue Kit	Macherey-Nagel, Germany
OptiView DAB Detection Kit	Roche AG, Switzerland
Protino™ Ni TED 2000	Macherey-Nagel, Germany
QIAquick® Gel Extraction Kit	QIAGEN GmbH, Germany
QuikChange® Lightning Site-Directed Mutagenesis Kit	Agilent Technologies, USA
RiboCop Human/Mouse/Rat V2	Lexogen GmbH, Austria
RNA 6000 Nano Chip	Agilent Technologies, USA
UltraView DAB Detection Kit	Roche AG, Switzerland
Vivaspin® 6/20 MWCO 10.000	Sartorius AG, Germany
ZymoPURE™ Maxi Prep Kit	Zymo Research, USA
ZymoPURE™ Mini Prep Kit	Zymo Research, USA

2.1.3 Consumables

Table 6. List of consumables used in this study

Item	Manufacturer
10 cm Tissue Culture Dishes	Sarstedt AG & Co KG, Germany
24-Well Tissue Culture Plates	Sarstedt AG & Co KG, Germany
6 cm Tissue Culture Dishes	Eppendorf SE, Germany
6-Well Tissue Culture Plates	Sarstedt AG & Co KG, Germany
96-Well Microtiter Plates	Sarstedt AG & Co KG, Germany
96-Well Microtiter Plates (non-TC treated, white)	Nunc, Thermo Fisher Scientific Inc, USA
96-Well Microtiter Plates (TC-treated, white)	Greiner Bio-One GmbH, Austria
Cannulas (all gauges)	B. Braun SE, Germany
Cell Scraper	Sarstedt AG & Co KG, Germany
Cell Spreader	Isolab GmbH, Germany
Cell Strainer (40 µm)	Corning Inc, USA
Cotton Swabs (Raucotupf)	Lohmann & Rauscher, Germany
Countess Counting Chambers	Invitrogen, Thermo Fisher Scientific Inc, USA
Cover Slips (12 mm Ø)	Hecht Glaswarenfabrik GmbH, Germany
Cryotubes (CryoPure)	Sarstedt AG & Co KG, Germany

Item	Manufacturer
Cytoslides (Shandon)	Thermo Fisher Scientific Inc, USA
Embedding Cassettes (Tissue-Tek®)	Sakura FineTek Europe, The Netherlands
FACS Tubes (5 mL)	Sarstedt AG & Co KG, Germany
Falcon Tubes (CELLSTAR®; 15 mL; 50 mL)	Greiner Bio-One GmbH, Austria
Filter Cards for Cytospins (Shandon)	Thermo Fisher Scientific Inc, USA
Filter Pipet Tips (2.5 µL; 10 µL; 100 µL; 1000 µL)	Sarstedt AG & Co KG, Germany
Freezing Container (Mr.Frosty™)	Thermo Fisher Scientific Inc, USA
Lancets (SoftClix)	Roche AG, Switzerland
Microcentrifuge Tubes (0.5 mL; 1.5 mL; 2 mL)	Eppendorf SE, Germany
Microtome Blades (FEATHER® S35)	pfm medical AG, Germany
Nitrocellulose Membranes (Amersham Protran®)	Merck KGaA, Germany
Object Slides (SuperFrost Plus)	Hecht Glaswarenfabrik GmbH, Germany
Parafilm	Bemis Company Inc, USA
PCR Tubes	Sarstedt AG & Co. KG, Germany
Scalpels	Dahlhausen & Co GmbH, Germany
Serological Pipettes (2 mL; 5 mL; 10 mL; 25 mL)	Sarstedt AG & Co KG, Germany
Sterile Filter Tops (0.2 µm; Filtropur V50)	Sarstedt AG & Co KG, Germany
Sterile Syringe Filters (0.2 µm; 0.45 µm)	Sarstedt AG & Co KG, Germany
Syringes (MicroFine 0.3 mL, for injections)	BD Biosciences, USA
Syringes (PlastiPak 30 mL, for filtering)	BD Biosciences, USA
Tissue Culture Flasks (T25; T75)	Sarstedt AG & Co KG, Germany
Tubes for Bacterial Culture (13 mL)	Sarstedt AG & Co KG, Germany
X-Ray Filters (CEA RP)	AGFA, Belgium

2.1.4 Technical Devices

Table 7. List of technical devices used in this study

Item	Description/Model	Manufacturer
Automatic Cell Counter	Countess 3	Invitrogen
Bioanalyzer	Agilent 2100	Agilent Technologies, USA
Brightfield Microscope	BX43	Olympus Corporation, Japan
Centrifuges	Heraeus Multifuge 3 R-S Heraeus Pico 21 Heraeus Fresco 17	Heraeus GmbH & Co KG, Germany
CO ₂ Cell Culture Incubator	HERAcell™ 240	Thermo Fisher Scientific Inc, USA
Cytoclips	Shandon	Thermo Fisher Scientific Inc, USA
Cytospin Centrifuge	Cytospin 4	Thermo Fisher Scientific Inc, USA
Cytospin Funnels	Shandon, reusable	Thermo Fisher Scientific Inc, USA

Item	Description/Model	Manufacturer
Dissecting Microscope	Leica M165 FC	Leica Camera AG, Germany
FACS Sorter	FACSAria™ Fusion	BD Biosciences, USA
Flow Cytometry System	LSRFortessa	BD Biosciences, USA
Fluorescence Microscope	Nikon Eclipse Ti2	Nikon Corporation, Japan
Gel Documentation System	BioDoc Analyze	Biometra GmbH, Germany
Gel Electrophoresis Chamber	Compact Multi-Wide	Biometra GmbH, Germany
Hamilton Needle (NanoFil)	NanoFil 26 Gauge	World Precision Instruments, USA
Hamilton Syringe	NanoFil	World Precision Instruments, USA
IncuCyte Imaging System	SX5	Sartorius AG, Germany
Isoflurane Vaporizer	Sigma Delta	Penlon Limited, UK
Laminar Flow Hood	HERASafe KS12 + KS18	Thermo Fisher Scientific Inc, USA
Microarray Scanner	iScan	Illumina, USA
Microtome	HM 325	Microm
Multipipette	M4	Eppendorf SE, Germany
PCR Thermocycler	T3000	Biometra GmbH, Germany
Pipettes	10 µL/200 mL/1000 µL	Gilson Inc, USA
Pipettor	Pipetus	Hirschmann Laborgeräte, Germany
Rocker-Shaker (Cell Culture)	PS-3D	Grant Instruments Inc, USA
Sequencing System	NextSeq500	Illumina, USA
Sequencing System (Single-cell)	NovaSeq6000	Illumina, USA
Shaker (Bacterial Culture)	innova 44	Eppendorf SE, Germany
Staining Tray	StainTray™	Carl Roth GmbH & Co KG, Germany
Steamer	Type 3216	Braun GmbH, Germany
Stereotactic Frame	Kopf 921	David Kopf Instruments, USA
Tape Station	2200	Agilent Technologies, USA
Tecan Reader	Infinite M200	Tecan Group AG, Switzerland
Thermomixer	ThermoMixer C	Eppendorf SE, Germany
Tissue Processor	ASP300S	Leica Camera AG, Germany
Ultracentrifugation Tubes	Oak Ridge, PPCO, 50 mL	Carl Roth GmbH & Co KG, Germany
Ultracentrifuge	Sorvall RC 5C PLUS	Thermo Fisher Scientific Inc, USA
UV-Vis Spectrophotometer	NanoDrop™ 2000	Thermo Fisher Scientific Inc, USA
Ventana Staining System	Benchmark XT	Roche AG, Switzerland
Vortexer	Reax Top	Heidolph Instruments, Germany
Water Bath	Hydro H4	LAUDA Technology Ltd, UK
Western Blot Cassette	Hypercassette™	Amersham plc, UK
X-Ray Film Processor	Structurix M ECO	Newco Inc, USA

2.1.5 Antibodies

Table 8. List of antibodies used for staining

Antibody Target	Manufacturer	Catalog Nr.	Source	Dilution (IHC)	Dilution (IF)
β -catenin	Dako, Agilent Technologies	M3539	Mouse	1:100	-
BrdU	Invitrogen, Thermo Scientific	B35128	Mouse	-	1:100
Calbindin	Merck KGaA	AB1778	Rabbit	1:100	-
CC-3	Cell Signaling Technology	9664	Rabbit	1:100	-
Cre	BioLegend	908001	Rabbit	1:100	-
GFAP	Dako, Agilent Technologies	M0761	Mouse	1:200	-
GFP (IHC)	Abcam, Inc.	ab13970	Chicken	1:500	-
GFP (IF, ms)	Invitrogen, Thermo Scientific	A11120	Mouse	-	1:100
GFP (IF, rb)	Invitrogen, Thermo Scientific	A11122	Rabbit	-	1:100
GLUT-1	Merck KGaA	07-1401	Rabbit	-	1:500
Ki67	Abcam, Inc.	ab15580	Rabbit	1:100	-
mCherry	Novus Biologicals	NBP2-25157	Rabbit	-	1:500
MYC	Cell Signaling Technology	D84C12	Rabbit	-	1:800
Nestin	Abcam, Inc.	ab221660	Rabbit	1:2000	-
NeuN	Merck KGaA	MAB377	Mouse	1:50	-
OLIG2	Merck KGaA	AB9610	Rabbit	1:200	-
Parvalbumin	Merck KGaA	MAB1572	Mouse	1:2000	-
PAX2	Invitrogen, Thermo Scientific	71-6000	Rabbit	-	1:200
PAX6	BioLegend	901301	Rabbit	1:1000	-
pHH3	Cell Signaling Technology	9706S	Mouse	1:200	1:200
RFP	Antibodies Online GmbH	ABIN129578	Rabbit	1:50	-
S100	Dako, Agilent Technologies	Z0311	Rabbit	1:100	-
SMARCA4	Abcam, Inc.	ab110641	Rabbit	1:25	1:25
SOX2	Abcam, Inc.	ab92494	Rabbit	1:200	-
Secondary Antibodies					
Anti-mouse Alexa 488	Cell Signaling Technology	4408S	Goat	-	1:500
Anti-mouse Alexa 555	Cell Signaling Technology	4409S	Goat	-	1:500
Anti-rabbit Alexa 488	Cell Signaling Technology	4412S	Goat	-	1:500
Anti-rabbit Alexa 546	Invitrogen, Thermo Scientific	A11035	Goat	-	1:500

Table 9. List of antibodies used for Western Blotting

Antibody Target	Manufacturer	Catalog Nr.	Source	Dilution (WB)
GAPDH	GeneTex	GTX100118	Rabbit	1:5000
SMARCA4	Abcam, Inc.	ab110641	Rabbit	1:10,000
MYC	Cell Signaling Technology	D84C12	Rabbit	1:500
β -Tubulin	Sigma-Aldrich	T4026	Mouse	1:500
Goat-Anti-Rabbit-HRP	Dako, Agilent Technologies	P0448	Goat	1:10,000
Goat-Anti-Mouse-HRP	Dako, Agilent Technologies	P0447	Goat	1:10,000

2.1.6 Primers

Primers listed in the table below were self-designed using *Primer-BLAST* [183] or were adapted from previous publications. They were synthesized by Metabion AG, Planegg, Germany.

Table 10. List of primers used in this study

Genotyping Primers			
Allele		Sequence (5'-3')	Expected PCR product
<i>cre</i>	Forward	TCCGGGCTGCCACGACCAA	448 bp
	Reverse	GGCGCGCAACACCATTTT	
<i>mNtf3</i> (added to <i>cre</i> PCR as control)	Forward	CTGAGTGACAGCACCCCTTT	100 bp
	Reverse	GTTTCCTCCGTGGTGAGGTT	
<i>Ctnnb1(ex3)</i>	Forward	CGTGGACAATGGCTACTCAA	wildtype: 330 bp floxed: 500 bp
	Reverse	TGTCCAACCTCCATCAGGTCA	
<i>Ctnnb1(ex3)</i> recombined	Forward	GTTCTCTCCCTTCTGCACAC	wildtype: 631 bp recombined: 400 bp
	Reverse	CTCTGAGCCCTAGTCATTGCATA	
<i>Ctnnb1(ex3)</i> recombined (FFPE)	Forward	ATCACGAGGCCCTTTTCGTCT	290 bp
	Reverse	TAGTCATTGCATACTGCCCGT	
<i>RFP</i>	Forward	AAAGTCGCTCTGAGTTGTTAT	wildtype: 600 bp mutant: 250 bp
	Rev (mut)	GCGAAGAGTTTGTCTCAACC	
	Rev (wt)	GGAGCGGGAGAAATGGATATG	
<i>Smarca4</i>	Forward	GTCATACTTATGTCATAGCC	wildtype: 241 bp floxed: 387 bp
	Reverse	GCCTGTCTCAAACCTGATAAG	
<i>Smarca4</i> recombined	Forward	GATCAGCTCATGCCCTAAGG	313 bp
	Reverse	GCCTGTCTCAAACCTGATAAG	
Primers for site-directed mutagenesis			
Name		Sequence (5'-3')	
<i>SMARCA4 T910M</i>	Forward	CCGCCTGCTGCTGATGGGCACACCGC	
	Reverse	GCAGCGGTGTGCCCATCAGCAGCAG	
<i>SMARCA4 R1135W</i>	Forward	CGAAGGCGGAGGACTGGGGCATGCT	
	Reverse	CAGCAGCATGCCCCAGTCCTCCGCCT	

Sequencing Primers		
Name		Sequence (5'-3')
<i>pLV-Myc-IRES-GFP</i>	Seq 1	GTGAACCGTCAGATCCAAG
	Seq 2	AAAGACAGCACCAGCCTGAG
<i>SMARCA4</i>	<i>T910M</i>	GGTGTCCCTGTACAACAACAAC
<i>SMARCA4</i>	<i>R1135W</i>	CCTACATGTTCCAGCACATC

2.1.7 Plasmids

Table 11. List of plasmids used for lentiviral production

Plasmid	Contains	Source
MSCV-Myc-IRES-RFP	murine MYC, RFP	Dr. Daisuke Kawauchi ¹
pLV-CMV-IRES-GFP (Mock)	GFP	Vectorbuilder.com
pLV-CMV-Myc-IRES-GFP	murine MYC, GFP	cloned in lab
LeGO-iC2-Zeo ⁺ (Mock)	mCherry, Zeocin resistance	Prof. Dr. Boris Fehse ²
LeGO-iC2-Zeo ⁺ -SMARCA4 WT	SMARCA4 WT, mCherry, Zeocin resistance	Dr. Franziska Modemann ²
LeGO-iC2-Zeo ⁺ -SMARCA4 T910M	SMARCA4 T910M, mCherry, Zeocin resistance	cloned in lab
LeGO-iC2-Zeo ⁺ -SMARCA4 R1135W	SMARCA4 R1135W, mCherry, Zeocin resistance	cloned in lab
LeGO-iC2Zeo ⁺ -hSMARCA4 shRNA	shRNA against human SMARCA4, mCherry, Zeocin resistance	Dr. Franziska Modemann ²
LeGO-iC2Zeo ⁺ -scrRNA	scrambled shRNA	Dr. Franziska Modemann ²
pEXP-DEST-LRC4	SHH-H His-tag fusion protein	Rowitch Lab ³
psPAX2	packaging proteins gag, pol, rev, tat	Addgene #12260
pMD2.G	envelope plasmid VSV-G	Addgene #12259

¹ National Cancer Center Hospital, Tokyo, Japan
² University Medical Center Hamburg-Eppendorf, Hamburg, Germany
³ University of Cambridge, Cambridge, UK

2.1.8 Software

Table 12. List of software used in this study

Software	Version	Manufacturer/Source
Cell Ranger	7.0.1	10x Genomics, Inc., USA
Cytoscape	3.9.1, Java 11.0.6	Open Source, https://cytoscape.org/
FACS Diva	8.0.1	BD Biosciences, USA
FlowJo®	10.6.1	FlowJo LLC, USA
GIMP	2.10.28	Open Source, www.gimp.org

Software	Version	Manufacturer/Source
Graph Pad Prism	9.4.1	GraphPad Software Inc, USA
ImageJ	1.53, Java 1.8.0	Open Source, https://imagej.net/ij/
IncuCyte	2021a	Sartorius AG, Germany
Inkscape	1.1	Open Source, www.inkscape.org
NIS-Elements	AR 5.11.03	Nikon Corporation, Japan
CellSens Entry	1.15	Olympus Corporation, Japan
R	4.1.1/4.1.2	Open Source, www.r-project.org
R Studio Desktop	2021.09.0	Open Source, https://posit.co/download/rstud
Snagene	5.0.7	GSL Biotech LLC, USA

2.2 Cloning of Constructs

2.2.1 MYC Lentivirus

A lentiviral plasmid for overexpressing MYC was generated by cloning the murine *Myc* gene into a self-designed lentiviral expression vector ordered from Vectorbuilder.com (pLV-CMV-IRES-GFP). Restriction enzymes BamHI and XhoI were used to cut out the *Myc* insert out of the MSCV-MYC-IRES-RFP vector, and to linearize the destination backbone pLV-CMV-IRES-GFP with a parallel dephosphorylation to avoid relegation (Table 13).

Table 13. Restriction digestion of donor (left) and recipient plasmid (right) for the generation of a lentiviral MYC construct

Reagent	Amount	Reagent	Amount
MSCV-MYC-IRES-RFP	1 µg	pLV-CMV-IRES-GFP	1 µg
Fast Digest Green Buffer (10x)	2 µL	Fast Digest Green Buffer (10x)	2 µL
BamHI Fast Digest	1 µL	BamHI Fast Digest	1 µL
XhoI Fast Digest	1 µL	XhoI Fast Digest	1 µL
DEPC H ₂ O	q.s. to 20 µL	Fast Alkaline Phosphatase	1 µL
		DEPC H ₂ O	q.s. to 20 µL
Incubation: 37 °C for 5 min, 80 °C for 5 min		Incubation: 37 °C for 10 min, 80 °C for 20 min	

After MSCV-MYC-IRES-RFP digestion, gel electrophoresis was performed on a 1% agarose gel with 0.05% ethidiumbromide at 90 V for 50 min. Then, the gel was examined under UV light, and the *Myc* fragment (at 1300 bp) was identified and cut out using a scalpel. Extraction of the DNA fragment was performed using the *QIAquick Gel Extraction Kit* according to manufacturer's instructions. The digested recipient plasmid pLV-CMV-IRES-GFP was purified using the same kit without performing gel electrophoresis. Subsequently, ligation was performed at a molar ratio of 1:3 (vector:insert) as described in table 14.

Table 14. Ligation of pLV-CMV-Myc-IRES-GFP construct

Reagent	Amount
pLV-CMV-IRES-GFP	30 ng
Myc insert	14.28 ng
T4 Ligase Buffer (10x)	2 μ L
T4 Ligase	1 μ L
DEPC H ₂ O	q.s. to 20 μ L
Incubation: 42 °C for 5 min, 16 °C overnight, 65 °C for 10 min	

Ligated constructs were transformed into competent *JM109* cells by adding 2 μ L of the ligation solution to freshly thawed cells and incubating on ice for 30 min. Afterwards, cells were smeared onto pre-warmed ampicillin (100 μ g/mL) agar plates, which were incubated at 37 °C overnight. Single colonies were picked and separately cultured in 3 mL of LB-Medium (10 g/L tryptone, 5 g/L yeast extract, 5 g/L NaCl) with ampicillin (50 μ g/mL) at 37 °C and 200 rpm overnight. The next day, isolation of plasmids was performed using the *ZymoPURE Mini Prep* kit according to manufacturer's instructions. Control digestion of the plasmids was performed with BamHI/XhoI as previously described in table 13. The presence of expected bands in gel electrophoresis confirmed successful ligation in some of the Mini Preps. Those were used for inoculating 150 mL of LB-Medium with ampicillin for the main culture at 37 °C and 200 rpm overnight. Lastly, the plasmids were isolated from the main culture using the *ZymoPURE Maxi Prep* kit according to manufacturer's instructions. The final DNA concentration was measured using a *NanoDrop* spectrophotometer and sequencing was performed at Microsynth Seqlab, Göttingen, Germany with two different primers (see table 10) to verify the sequence of the *Myc* construct.

2.2.2 SMARCA4 Variants

A lentiviral construct for the overexpression of SMARCA4 (LeGO-iC2-Zeo+-SMARCA4 WT) was provided by Dr. Franziska Modemann, University Medical Center Hamburg-Eppendorf. To introduce point mutations T910M (base change ACG→ATG) and R1135W (base change CGG→TGG) similar to those found in pediatric MB patients, the *QuikChange Lightning Site-Directed Mutagenesis* kit was used according to manufacturer's instructions. Briefly, for each mutation, two primers bearing the desired base change were designed (forward and reverse, see table 10). These were used in a PCR to amplify the construct, thereby adding the desired base change. Any remaining template without the base change was digested by adding the DpnI restriction enzyme, which specifically cleaves methylated DNA. Then, the PCR product was used for transformation in

XL10Gold ultracompetent cells, and colonies were picked for Mini Prep with subsequent sequencing using the sequencing primers described in table 10. Clones with successful base change were selected for a main culture and Maxi Prep.

2.3 Mouse Experiments

All experimental procedures on animals were approved by the Government of Hamburg, Germany (N113/16, N050/2018, N099/2019) and were performed according to national regulations. Mice were kept on a 12 h dark/light cycle and food and water was provided *ad libitum*. Animals of both sexes were used. Mice younger than 13 days were sacrificed by decapitation. Older mice were sacrificed by floating the cage with CO₂ (30-50% of cage volume/min) with subsequent cervical dislocation to ensure death. For dissection of embryos, pregnant mothers were sacrificed as described above. Then, the uterus was removed via caesarean section and each embryo was separately collected and sacrificed by decapitation. In embryonic experiments, the day of vaginal plug detection in the morning after mating and ovulation was defined as embryonic day 0.5 (E0.5). Postnatal days were counted starting with postnatal day 0 (P0) on the day of birth.

2.3.1 Mouse Strains

The mouse strains used in this study are described in table 15. Except for *CD1^{nu/nu}*, they were all maintained on a *C57Bl6/J* background.

Table 15. Mouse strains used in this study

Mouse strain (official name)	Characteristics	Provided by	Original Publications
<i>Blbp-cre</i> (<i>B6, CB-Tg(Fabp7-creLacZ)3Gtm/Nci</i>)	cre expression in neural progenitors	NCI Repository (strain #01XM9)	[149]
<i>CD1^{nu/nu}</i> (<i>Crl:CD1-Foxn1^{nu}</i>)	immunodeficient (lack of thymus)	Charles River (strain #086)	[184]
<i>Ctnnb1(ex3)^{fl/fl}</i>	loxP sites flanking exon 3 of <i>Ctnnb1</i> → loss of phosphorylation site upon cre expression	M.M Taketo, Kyoto, Japan	[185]
<i>IslR26tdRFP^{fl/fl}</i> (<i>Gt(ROSA)26Sortm1Hjf</i>)	excision of stop codon upon cre expres- sion → RFP signal	MGI: 3696099	[186]
<i>Math1-creER^{T2}</i> (<i>Tg(Atoh1-cre/Esr1*)14Fsh/J</i>)	cre expression in GCPs, induced by ta- moxifen injection	Jackson Labora- tory (strain #7684)	[151]
<i>Smarca4^{fl/fl}</i> also known as <i>Brg1^{fl/fl}</i>	loxP sites flanking exon 2 and 3 of <i>Smarca4</i> → loss of protein upon cre ex- pression	P. Chambon, Illkirch, France	[187, 188]

2.3.2 Tamoxifen Induction

To induce *Smarca4* recombination in *Math1-creERT²::Smarca4^{f/f}* mice, pups received a single dose of 0.4 mg tamoxifen dissolved in 20 μ L of corn oil at P3. For this purpose, 0.3 mL syringes were filled with the solution under sterile conditions, and the injection was performed intraperitoneally. Mice were sacrificed at the age of 7 or 8 days for further analysis or cell culture.

2.3.3 Genotyping

2.3.3.1 DNA Isolation

Tail tips or ear biopsies were used for genotyping of mice. First, the samples were incubated in 500 μ L of Laird's lysis buffer (200 mM NaCl, 0.2% SDS, 100 mM Tris-HCl, 5 mM EDTA in ddH₂O) with 400 μ g/mL Proteinase K at 56 °C and 1000 rpm for 2 h. Afterwards, each sample was centrifuged at 4 °C and 14,000 rpm for 5 min. The supernatant holding the genomic DNA was transferred into a new 1.5 mL tube containing 500 μ L isopropanol. Again, the tube was centrifuged at 4 °C and 14,000 rpm for 5 min, and the isopropanol was discarded. The DNA pellet was air-dried and resuspended in 100 μ L TE Buffer (20 mM Tris, 1 mM EDTA in ddH₂O). Afterwards, the solution was incubated at 37 °C and 1000 rpm for 1 h. Finally, the isolated DNA was stored at 4 °C.

2.3.3.2 Fast DNA extraction with HotSHOT Method

To increase the speed of genotyping for samples used in single-cell RNA sequencing and embryo transplantation experiments, DNA extraction was performed according to the HotSHOT protocol (described by Truett *et al.* [189]). Briefly, tissue biopsies were incubated in 75 μ L Alkaline Lysis Reagent (25 mM NaOH, 0.2 mM Na₂EDTA in ddH₂O) in a Thermocycler at 95 °C for 30 min. Then, samples were cooled down and 75 μ L of Neutralization Reagent (40 mM Tris-HCl in ddH₂O) were added. After ensuring the solution was well-mixed, 1-2 μ L were directly used for PCR reactions as described in the next section.

2.3.3.3 PCR Analysis

For the determination of genotypes, specific regions for each mutated allele were amplified by PCR using the previously isolated genomic DNA. The composition of the master mix is described in table 16. The PCR programs were individually optimized for each allele as shown in table 17.

Table 16. Composition of PCR mastermix for genotyping per sample

Reagent	Volume (μL)	Final Concentration
PCR buffer (5x)	2	1x
MgCl ₂ *	0.5	25 mM
dNTPs	0.15	10 mM
forward primer	0.25	0.25 M
reverse primer	0.25	0.25 M
DNA	1	-
DEPC H ₂ O	5.75	-
Taq Polymerase	0.1	0.05 U/ μL
Total volume	10 μL	

* PCRs for *Ctnnb1 rec* and *SMARCA4 rec* were performed without MgCl₂

Table 17. PCR programs for genotyping

	<i>cre</i>	<i>Ctnnb1</i>	<i>Ctnnb1 rec</i>	<i>RFP</i>	<i>Smarca4</i>	<i>Smarca4 rec</i>
Initial denaturation	95 °C, 3 min	92°C, 2 min	95°C, 3 min	94 °C, 5 min	94 °C, 3 min	94°C, 5 min
Denaturation	95 °C, 20 s	92°C, 20 s	95°C, 20 s	94 °C, 30 s	94 °C, 20 s	94°C, 30 s
Annealing	65 °C, 30 s	60°C, 30 s	62°C, 30 s	50 °C, 30 s	55 °C, 30 s	50°C, 30 s
Elongation	72 °C, 1 min	72°C, 1 min	72°C, 40 s	72 °C, 30 s	72 °C, 1 min	72°C, 1 min
Number of cycles	32	35	35	35	35	35
Final elongation	72 °C, 3 min	72°C, 3 min	72°C, 3 min	72 °C, 5 min	72 °C, 3 min	72°C, 5 min
Cooling	4 °C, ∞	4 °C, ∞	4 °C, ∞	4 °C, ∞	4 °C, ∞	4 °C, ∞

To analyze the fragment size of PCR products, gel electrophoresis was performed using a 2% agarose gel (in 1x TAE buffer [40 mM Tris, 20 mM glacial acetic acid, 1 mM EDTA]) containing 0.5 $\mu\text{g}/\text{mL}$ ethidium bromide at 130 mA for 40 min. DNA bands were detected under UV light in a *Biometra Gel Documentation* system.

2.3.4 Stereotactic Transplantations

Before transplantation, the samples (either GCPs or embryonic hindbrain progenitors [HPCs]) were prepared according to their individual protocol (see sections 2.4.8.4 and 2.4.9.2) and were kept on ice until injection. Recipient mice (6-week-old *CD1^{nu/nu}*) received analgesia by subcutaneous injection of carprofen (6 mg/kg; 50 mg/mL stock diluted 1:100 in 0.9% NaCl) before the procedure. During transplantation, they were anesthetized with isoflurane (3.5% for induction, later reduced to 2.5%) in a stereotactic frame and were placed on a heating pad. Eye ointment was applied to avoid dehydration. The head was safely secured, and the skin was disinfected using

80% EtOH before adding 2% lidocaine for local anesthesia. Then, a cut was performed in the hind-brain area using a scalpel, and the skull was uncovered with the help of sterile cotton swabs. Lidocaine was added to the exposed area before puncturing the skull at coordinates $x = +1$ mm and $y = -1$ mm from the lambda suture. At this site, the cell suspension was injected using a Hamilton (Nanofil) syringe at $z = -2$ mm with an angle of 30° measured from the skull surface. Afterwards, the syringe was removed and rinsed with sterile water and EtOH. The wound was glued with tissue adhesive and sterilized with antiseptic. Then, mice were removed from the stereotactic frame and were allowed to recover in a warmed cage until they were fully awake and ready to be resocialized again. The next day, transplanted mice received another dose of carprofen (6 mg/kg). They were monitored daily for any sign of tumor development within the next six months.

2.4 Cell Culture

Cell lines and primary murine embryonic cells were cultured at the laboratory facilities of the Research Institute Children's Cancer Center Hamburg in a *HERAcell™ 240* incubator at 37°C , 5% CO_2 , and 86% humidity.

2.4.1 Lentivirus Production

2.4.1.1 Culture and Transfection of HEK293T

HEK293T cells were cultured in DMEM supplied with 10% FCS and 50 U/mL penicillin/streptomycin (Pen/Strep) in T75 flasks and were passaged when reaching a confluency of around 80%. For this purpose, medium was aspirated, and flasks were washed with 5 mL of PBS. 2 mL of Trypsin/EDTA were added, and flasks were incubated at 37°C for around 5 min. Cells were detached from the surface by tapping against the flasks, and 5 mL of medium was added to stop the reaction. Then, the cell suspension was centrifuged at $300 \times g$ for 5 min, and the pellet was resuspended in 1 mL of medium for cell counting. For lentivirus production, cells were seeded onto 10 cm dishes at a density of 3-4 mio cells per dish. The next day, medium was aspirated and replaced by DMEM without any supplements. Cells were placed back into the incubator for two hours before starting transfection. Meanwhile, the transfection mix was prepared as shown in table 18. The two separate tubes were combined by dropwise adding of the contents of tube 2 to tube 1 while steadily introducing bubbles with a 2 mL pipet tip. Then, the solution was incubated at RT for 10 min. Afterwards, transfection of the HEK293T culture was performed by dropwise adding of 1 mL transfection mix per dish while gently swirling the dishes.

Table 18. Composition of lentiviral transfection mix

Tube	Reagent	Volume per Dish	Final Concentration
1	2x HBS*	500 μ L	1x
	Lentiviral plasmid	**	1.64 pmol
	psPAX2	**	1.30 pmol
2	pMD2.G	**	0.72 pmol
	Aqua ad ini.	ad 500 μ L	
	CaCl ₂ (2.5 M)	100 μ L	0.5 M

* 270 mM NaCl, 10 mM KCl, 1.4 mM Na₂HPO₄, 40 mM HEPES, 10 mM D-Glucose in ddH₂O, pH adjusted to 7.05

** calculated individually depending on concentration in plasmid preparation

After an incubation time of 4-6 h in the incubator, medium was replaced by DMEM +10% FCS + 50 U/mL Pen/Strep for further cultivation. Successful transfection was confirmed by the detection of a GFP or mCherry signal under the microscope on the next day. Harvesting of the viral supernatant was performed twice on day 2 and 3 after transfection. For this purpose, the medium was aspirated using a 30 mL syringe and was filtered through a 0.45 μ m membrane to remove cells from the solution. The viral supernatant was stored at 4 °C until ultracentrifugation.

2.4.1.2 Concentration of Lentiviral Supernatant

For concentration of viral supernatant, ultracentrifugation was performed. First, the viral supernatant was equally distributed into autoclaved ultracentrifugation tubes using a scale. Then, ultracentrifugation was performed at 4 °C and 20,000 rpm for 4 h using the *SS-34* rotor in a *Sorvall RC 5C* ultracentrifuge. Afterwards, the supernatant was carefully aspirated, and the pellet was re-suspended in DMEM (volume around 100 times less than volume of viral supernatant) without any supplements and allowed to dissolve for 30 min at 4 °C. The resulting solution was pooled in a 1.5 mL tube, and aliquots of around 20-50 μ L were prepared and stored at -80 °C.

2.4.1.3 Titration of Lentivirus

For titration of lentivirus, HEK293T cells were seeded onto a 24-well plate in a density of 5×10^4 cells per well. Polybrene (10 μ g/mL) was directly added to the medium to ameliorate transduction efficiency. Then, cells were allowed to adhere for 2-5 h before transduction. An aliquot of ultracentrifuged virus was thawed, and different amounts of virus (0.1 μ L, 1 μ L, 10 μ L) were added to the cells in triplicates. Afterwards, the plate was centrifuged at 1,000 x g for 1 h and was placed back into the incubator. Around 72 h later, cells were dissociated with Trypsin/EDTA, and the cell suspension was transferred into FACS tubes. Fixation of cells was performed by adding the same amount of 8% PFA to achieve an overall concentration of 4% PFA. Then, the fluorescence signal

of cells (GFP⁺ [laser: 488 nm, emission filter: 530/30 nm] or mCherry⁺ [laser: 561 nm, emission filter: 610/20 nm]) was detected on an *LSRFortessa* flow cytometer using the *FACS Diva* software. The *FlowJo* software was used to perform exclusion of dead cells and doublets and to calculate the percentage of transduced cells. For calculating the virus titer, a condition with a transduction efficiency between 5-20% was chosen. Then, the titer was calculated as follows:

$$T \text{ (TU/mL)} = \frac{N * P}{V \text{ (mL)}}$$

T: Titer; N: nr of cells/well (5×10^4); P: percentage of transduced cells; V: volume of virus added

2.4.2 SCCOHT-1 Cell Line

SCCOHT-1 cells [190] were cultured in RPMI-1640 media, supplemented with 10% FCS, 1% L-Glutamine, and 50 U/mL Pen/Strep and were dissociated as described for HEK293T cells in section 2.4.1.1 when reaching a confluency of around 80%.

2.4.3 Medulloblastoma Cell Lines

MB cell lines used in this study are listed in table 19. For all three cell lines, sequencing of *SMARCA4* was performed by Florian Oyen (Pediatric Hematology and Oncology, University Medical Center Hamburg Eppendorf) and confirmed the absence of mutations.

Table 19. MB cell lines used in this study

Cell Line	MB Subgroup	Patient	Oncogenic Drivers	Culture Conditions
D283	Group 4, classic	male, 6 y	<i>MYC</i> rearranged, isochromosome 17q	Adherent, EMEM + 10% FCS + 50 U/mL Pen/Strep
D341	Group 3, classic	male, 3 y	<i>MYC</i> amplified, isochromosome 17q	Suspension, EMEM + 20% FCS + 50 U/mL Pen/Strep
D425	Group 3, classic	not known	<i>OTX2</i> amplified	Suspension, DMEM + 10% FCS + 50 U/mL Pen/Strep

D283 cells were cultured in T75 TC treated flasks, singularized as described for HEK293T cells in section 2.4.1.1, and media was exchanged every 2-3 days. Both adherent cell lines D341 and D425 were cultured in T75 suspension flasks and singularized by centrifuging the cell suspension ($300 \times g$ for 5 min) and resuspending with a pipet. Fresh medium was added to the cell suspension every 2-3 days.

2.4.4 Transduction of Cell Lines

For transduction with lentiviral *SMARCA4* constructs and mCherry mock constructs as a control (see plasmids in 2.1.7), cell lines were seeded onto 24-well plates in a density of

100,000 cells/cm². Protamine sulfate was added at a concentration of 8 µg/mL to ameliorate transduction efficiency. Then, ultracentrifuged viral supernatant was added to achieve a multiplicity of infection (MOI) of around 1-5 (individually optimized for different lentiviral batches). Plates were centrifuged at 2,000 rpm for 1 h at RT. The presence of a mCherry signal was detected on the *Nikon Eclipse Ti2* fluorescence microscope 3-5 days after transduction.

2.4.5 Selection and Sorting of Transduced Cells

Selection or sorting of transduced MB cell lines was performed five days after transduction. Adherent D283 cells were selected by the addition of Zeocin (500 µg/mL) for three weeks to ensure depletion of all remaining non-transfected cells. For suspension cell lines D341 and D425, FACS sorting of successfully transduced mCherry-positive cells was performed using a *BD FACSAria Fusion* flow cytometer (laser: 561 nm, emission filter: 610/20 nm) and the software *FACS Diva* software.

2.4.6 Cell Titer Glo Cell Viability Assay

After selection or sorting of cells, cells were seeded onto white TC treated (D283) or non-TC treated (D341+D425) 96-well plates in a density of 20,000 cells per well. *Cell Titer Glo® Luminescent Cell Viability* assays were performed after seeding and on day 2, 4, and 7 in culture according to manufacturer's instructions. Briefly, 100 µL of *Cell Titer Glo* solution were added to each well, plates were transferred into a *Tecan infite M200* plate reader, and after shaking for 2 min and incubation for another 8 min, luminescence was measured.

2.4.7 Freezing and Thawing of Cells

For the freezing of cells, cells were singularized according to their individual protocol. After the centrifugation step, resulting cell pellets were resuspended in their respective cell culture medium with the addition of 10% DMSO. The cell suspension was transferred to a cryotube, which was stored at -80 °C in a *Mr. Frosty™* freezing container and relocated to liquid nitrogen after testing negative for mycoplasma contamination. For thawing of cells, the frozen cryotube was warmed up rapidly at 37 °C in a water bath. Subsequently, the cell suspension was mixed with double the amount of warmed medium and centrifuged for 5 min at 300 x g. The resulting cell pellet was resuspended in medium and was used for reseeding in flasks or well-plates.

2.4.8 Murine Granule Cell Precursors (GCPs)

For isolation of primary murine GCPs, pups (*Math1-creER^{T2}::Smarca4^{fl/fl}* or *Smarca4^{fl/fl}*) were sacrificed at P7 or P8 by decapitation. Then, heads were dipped into 80% EtOH and transferred into a petri dish containing HBSS/Glc solution (1x HBSS in ddH₂O, 6 g/L D-Glucose, pH adjusted to 7.2). Brains were removed from the skull and were transferred into individual small petri dishes with

HBSS/Glc on ice until all brains were prepared. Under a dissecting microscope, the cerebellum was separated from the rest of the brain, and meninges and plexus were removed. For each genotype, cerebella were pooled in a 15 mL tube with HBSS/Glc on ice and were centrifuged at 70 x g for 5 min. After carefully aspirating the supernatant with a pipet, the cerebella were resuspended in a 2 mL solution of Trypsin/EDTA with DNase (400 µg/mL) for tissue digestion. The solution was incubated for 10 min at 37°C while agitating every 2 min. Afterwards, the digested tissue was resuspended using a 1 mL pipet tip and 4 mL of GCP medium (DMEM/F-12 + GlutaMAX, 25 mM KCl, 50 U/mL Pen/Strep, 1x N2 Supplement) with 10% FCS were added to stop the reaction. Non-digested tissue was allowed to sink to the bottom of the tube, and the cell suspension above was transferred into a new 15 mL tube. After centrifugation at 200 x g for 5 min, the pellet was resuspended in HBSS/Glc and centrifuged again. Finally, the pellet was resuspended in GCP medium + FCS, and the suspension was pipetted onto a 40 µm cell strainer to exclude any remaining debris. Cells were counted with the *Automatic Countess Cell Counter* and were seeded into 24-well plates coated with PLO (15 µg/mL in Aqua ad ini., coated at 4°C overnight) in a density of 1 mio cells per well. The next day, medium was changed to GCP medium without FCS and 3 µg/mL SHH protein were added to induce proliferation of GCPs.

2.4.8.1 Generation of SHH Protein

SHH Protein was recombinantly expressed by *BL21* competent bacteria transformed with the pEXP-DEST-LRC4 vector. Pre-culture in LB medium with ampicillin (50 µg/mL) was inoculated and incubated overnight at 37 °C and 120 rpm. The next day, the preculture was diluted 1:20 in LB medium with ampicillin and again cultured at 37 °C and 120 rpm until reaching an optical density of 0.4-0.6. Expression of SHH protein was induced by adding 1 M isopropyl-β-D-thiogalactopyranoside (IPTG). After an incubation time of two hours, cells were pelleted and homogenized by sonification. His-tag protein purification was performed using the *Protino™ Ni TED 2000* Kit according to manufacturer's instructions. Next, the *Vivaspin® 6/20 MWCO 10.000* Kit was applied to concentrate the samples. The final protein concentration was measured using the *DC Protein Assay* according to manufacturer's instructions. Finally, SHH protein was stored in aliquots at -80°C diluted in SHH storage buffer (5 mM Na₂HPO₄, 150 mM NaCl, 0.5 mM DTT in ddH₂O).

2.4.8.2 Transduction of GCPs

GCPs were transduced 3-4 h after plating. First, protamine sulfate was added in a concentration of 8 µg/mL to ameliorate transduction efficiency. Then, ultracentrifuged virus was added to reach a MOI of around 0.5. The optimal amount for each virus production was individually determined by pilot experiments using a range of different concentrations with subsequent evaluation of

transduction efficiency and cell survival. After transduction, the culture plates were centrifuged at 2,000 rpm or 1h at RT. Medium was changed the next day as described above.

2.4.8.3 Fixation of GCPs for Immunocytochemistry

For immunocytochemistry of GCP cultures, autoclaved 12 mm coverslips were placed inside the 24-well plates before PLO coating and seeding of cells. Two hours before fixation, BrdU was added to the cells at a concentration of 25 $\mu\text{g}/\text{mL}$. BrdU is a synthetic thymidine analogue, which is incorporated into the DNA during replication in the S phase of the cell cycle, thereby marking actively dividing cells [191]. After incubation, medium was aspirated and 500 μL of 4% formaldehyde were added to each well for 10 min at RT. Then, wells were washed twice with PBS and the plates were sealed with parafilm and stored at 4 $^{\circ}\text{C}$ until further use.

2.4.8.4 Preparation of GCPs for Transplantation

To detach GCPs from well plates, medium was aspirated, and wells were washed with PBS. Accutase was added (100 $\mu\text{L}/\text{well}$), and cells were incubated at RT for 10 min. Then, the cell layer was rinsed off using a pipet tip with 400 μL GCP medium, and cells were pooled in a 15 mL tube for each condition. After centrifuging the tubes at 300 x g and 4 $^{\circ}\text{C}$ for 5 min, the pellet was resuspended in 1 mL of GCP medium for cell counting. For each planned transplantation, 1.5×10^6 cells were transferred into a 1.5 mL tube and centrifuged again at 300 x g and 4 $^{\circ}\text{C}$ for 5 min. The supernatant was carefully aspirated to not break the pellet, and cells were resuspended in 50 μL of cold GCP medium and transferred into a new tube. After a last centrifugation step, cells were resuspended in 3 μL of cold GCP medium with 3 $\mu\text{g}/\text{mL}$ SHH, and 1 μL of Matrigel was added. Cells were kept on ice until the injection.

2.4.9 Murine Hindbrain Progenitor Cells (HPCs)

For the isolation of HPCs, E14.5 embryos (*Blbp-cre::Ctnnb1(ex3)^{fl/wt::Smarca4^{fl/fl}}*, *Blbp-cre::Ctnnb1(ex3)^{fl/wt::Smarca4^{fl/wt}}* or cre-negative littermates) were collected by caesarean section and were sacrificed by decapitation. The heads were transferred into individual small petri dishes with HBSS/Glc (1x HBSS in ddH₂O, 6 g/L D-Glucose, pH adjusted to 7.2), and tissue biopsies of each embryo were collected for genotyping. Under a dissecting microscope, the skull was opened, and the hindbrain was dissected and transferred into a 1.5 mL tube filled with HBSS/Glc on ice. After centrifuging the tubes at 110 x g for 5 min, the pellet was resuspended in Papain/DNase solution (Papain 20 U/mL, DNase 400 $\mu\text{g}/\text{mL}$ in DMEM/F12) for tissue dissociation. The tubes were incubated at 37 $^{\circ}\text{C}$ in the cell culture incubator on a Rocker-Shaker for 30 to 60 min. Then, the cell suspension was carefully resuspended and centrifuged at 300 x g for 5 min. Cells were resuspended in NSC medium (DMEM/F-12 + GlutaMAX, 40 mM HEPES, 1x B27 Supplement, 1x MEM-NEAA, 50 U/mL Pen/Strep, 20 ng/mL EGF, 20 ng/mL FGF) and were transferred into 25 mL flasks

for cell culture. EGF and FGF was freshly added every 2-3 days during the cultivation period. Approximately every week or when spheres reached a diameter of around 100 μm , cells were singularized using Accutase. For this purpose, spheres were centrifuged at 300 x g for 5 min. The pellet was resuspended in Accutase and incubated for 10 min at RT. Then, spheres were broken apart by pipetting up and down 10 times. Cells were counted and reseeded into new T25 flasks at 1 mio cells per flask.

2.4.9.1 Calculation of Cumulative Population Doublings (cPDs)

Weekly cell counts ensured monitoring of cell proliferation during the whole cultivation period of HPCs. For each cell culture, two cell counts after singularization were averaged and population doublings were calculated as follows:

$$\text{PD} = \log_2 \left(\frac{\text{cell count}}{\text{cells seeded}} \right)$$

Then, cumulative population doublings (cPDs) were calculated by adding the PDs observed until the respective day. For each genotype, the cPDs of at least three different embryonic cell cultures were averaged for comparison.

2.4.9.2 Preparation of HPCs for Transplantation

Directly after isolation and cell counting, cells of each embryo (irrespective of cell count) were centrifuged at 200 x g and 4°C for 5 min. The pellet was resuspended in 50 μL of cold NSC medium and transferred into a new 1.5 mL tube. Similar to GCPs, cells were resuspended in 3 μL of HPC medium with EGF/FGF, and 1 μL of Matrigel was added. Cells were kept on ice until ready for injection.

2.4.9.3 Live Cell Microscopy

Live brightfield and fluorescence images during cell culture of GCPs and HPCs were taken either automatically using the *IncuCyte Cell Imaging* system or manually using the *Nikon Eclipse Ti2* microscope.

2.5 Histological Analysis of Tissues and Cells

2.5.1 Embedding of Mouse Tissue

For histological analysis, mouse tissue was fixed in 4% formaldehyde solution for at least 24 h. Brains of mice older than one day were removed from the skull before fixation, while the brains of embryonic or newborn mice were left inside the skull. In this case, the skin was removed, and two small holes were pricked into the skull with lancets to ensure better penetration of formaldehyde. After fixation, brains were cut in sagittal or frontal direction before further processing.

The tissue was dehydrated using an automatic tissue processor with the programs listed below (Table 20). The standard program was used for brains and embryonic heads up to E14.5, the extended program was used for embryonic heads from E16.5 and whole heads of newborn mice. The dehydrated tissue was then embedded in paraffin, and a microtome was used to cut 2 μm thick sections for histological analysis.

Table 20. Dehydration program for mouse tissue

Reagent	Time [min]	Time [h]
	Standard Program	Extended Program
3.5% Formaldehyde	60	1
ddH ₂ O	15	0.5
70% Ethanol	30	2
80% Ethanol	45	4
96% Ethanol	75	5
96% Ethanol	75	5
100% Ethanol	90	8
100% Ethanol	120	8
Xylo	45	4
Xylo	120	6
Paraffin	60	6
Paraffin	90	6
Paraffin	90	6

2.5.2 Embedding of Cells

To embed HPCs or cell lines in paraffin blocks, cells were centrifuged at 300 x g for 5 min. Then, 100 μL of 4% formaldehyde solution were added for fixation. After incubating for 10 min, cells were centrifuged again, and the pellet was washed twice with PBS. Subsequently, they were re-suspended in a mixture of 50 μL PBS and 50 μL of 3% low melting agarose. After hardening, the resulting gel blocks were embedded in paraffin, and 2 μm thick sections were cut for histological analysis.

2.5.3 Cytospins

As an alternative to embedment in paraffin, e.g. when cell numbers were too low (<1 mio), cells were fixed on cytospins. For this purpose, cytospin funnels, filter papers, and object slides were assembled in a *Cytospin 4* centrifuge. To each cytospin, around 5×10^5 cells in 100 μL of PBS were added through the cytofunnel. After centrifugation at 400 rpm and low acceleration for 5 min, cells on the object slides were fixed by adding 4% of formaldehyde solution for 15 min at RT. Then,

the formaldehyde was removed, and PBS was added to the samples for storage at 4 °C before histological analysis.

2.5.4 Immunohistochemistry (IHC) staining

DAB (3,3'-Diaminobenzidine) stainings were performed on a *Ventana Benchmark xt* system using the *ultraView*, *OptiView*, or *iView* DAB detection kit according to manufacturer's instructions. In these stainings, the secondary antibody is coupled to a horseradish peroxidase (HRP), which catalyzes the oxidation of DAB substrate, resulting in a brown precipitate as a positive signal. Afterwards, all nuclei are counterstained in blue using hematoxylin.

Hematoxylin & Eosin (HE) stainings were performed according to standard protocols after deparaffinizing slides in a descending ethanol row. This staining results in a purple-blue coloring of nuclei and pink coloring of cytoplasm and extracellular matrix.

2.5.5 Immunofluorescence (IF) Stainings

Immunofluorescence stainings of FFPE tissue (IF-P) were performed manually. First, slides were deparaffinized in a descending ethanol row according to standard protocols. Then, antigen retrieval was performed by heating up the slides in citrate buffer (10 mM trisodium citrate dihydrate in ddH₂O, pH adjusted to 6.0) in a steamer for 20 min. After cooling down, the slides were washed in ddH₂O (5 min) followed by PBS-T (0.3% Triton X-100 in PBS) (3x 5 min). Then, blocking was performed with 5% normal goat serum (NGS) in PBS-T for 1 h at RT. A PAP pen was used to encircle the tissue to be stained before adding the primary antibody in blocking solution. Slides were transferred into a slide moisture chamber for overnight incubation at 4 °C. The next day, slides were washed with PBS (3x 5 min). The secondary antibodies (1:500) and DAPI (1:1000 of 1 mg/mL stock) were diluted in PBS with 0.3% NGS and were added to the samples for an incubation time of 1 h at RT in the dark. After a last washing step with PBS (3x 5 min), slides were mounted with Mowiol 4-88 (solution prepared according to manufacturer's instructions).

2.5.6 Immunocytochemistry

For fluorescence staining of cells, the respective wells or cytopins were stained as described in table 21. To reduce the amount of primary antibody needed, samples on cytopins were encircled with a PAP pen, while coverslips were removed from the wells and mounted upside down onto pipetted drops of antibody solution on parafilm in a wet chamber.

Table 21. Immunocytochemistry protocol

Step	Solution	Incubation
Permeabilization	PBS-T	2x5 min
DNA Denaturation	4 N HCl	} only in case of BrdU staining
Acid Neutralization	Borax buffer*	
Blocking	5% NGS in PBS-T	30 min
Primary antibodies	diluted in blocking solution	overnight, 4 °C
Wash	PBS-T	3x 5 min
Secondary antibodies + DAPI	1:500 } 1:1000 }	} in 0.3% NGS } in PBS
Wash	PBS	
Mounting	Mowiol	dry at 4 °C overnight

*0.1 M Borax anhydrous in ddH₂O, pH adjusted to 8.5

2.5.7 Image Analysis and Quantification

All IHC and HE stainings were imaged using the *Olympus BX43* brightfield microscope and the *Olympus cellSens* software. For imaging of IF stainings, the *Nikon Ti2* microscope with the camera *DS Qi2* and the corresponding software *NIS-Elements* was used. White balance correction of brightfield images was performed using the *GIMP* image manipulation software.

2.5.7.1 Cell Counting (IF of fixed cells and Cytospins)

IF signals of stained GCPs or cells on cytopins were detected automatically using the *Automatic Measurement* tool of the *NIS-Elements* software. The threshold for fluorescence intensity and cell size was adjusted separately for each fluorescence channel and was applied to all samples to retrieve cell counts. At least three representative images were analyzed for each sample and staining. When big piles of cells were present within the cultures, single cells were separated manually within these regions. Binary levels were created to analyze the overlay of two different fluorescent channels.

2.5.7.2 Cell Counting (IHC-P and IF-P)

Quantitative analysis of IHC-P and IF-P slides was performed with *ImageJ*. To determine the percentage of labelled cells (either chromogenic or fluorescent signal), cells were counted by hand using the *Cell Counter* tool and divided by the total number of cells in the respective region.

2.5.7.3 Area Measurement (Ki67 IHC-P)

Area measurement of Ki67-positive area on IHC slides was performed with *ImageJ*. First, pictures were cropped to display a region of 200 μ m in height measured from the fourth ventricle. Then, these images were converted into 8-bit format, and the white/black threshold was set using the

IJ_IsoData Macro. The tools 'Erode', 'Dilate', 'Remove Outliers', and 'Fill Holes' were used to optimize the mask. Then, the *area_fraction* tool was used to measure the fraction of white area corresponding to a positive Ki67 signal.

2.6 Protein Analysis by Western Blotting

2.6.1 Isolation and Quantification of Protein

Protein isolation from GCP cultures was performed on ice to avoid any protein degradation. The culture medium was aspirated, and the plates were washed with 500 μ L of PBS per well. Then, 100 μ L RIPA buffer (50 mM Tris, 150 mM NaCl, 0.5% sodium deoxycholate, 0.1% SDS, 1% Triton-X-100, 1x protease inhibitor cocktail) was added to the first well, and the cell layer was scratched off with a cell scraper. Subsequently, the solution was transferred to the next well until cells from all wells were detached. Finally, the solution was transferred into a 1.5 mL tube and was incubated for 30 min at 4 °C and 1,000 rpm in a Thermomixer. Subsequently, samples were centrifuged (12,000 x g, 30 min, 4 °C) to remove any remaining cell debris, and the supernatant containing the protein was collected. To determine protein concentrations in the samples, the *DC Protein Assay* was applied according to manufacturer's instructions.

2.6.2 Protein Detection via Western Blot

To detect a protein of interest within a sample, the isolated protein mixture was first separated by SDS-PAGE (sodium dodecyl sulfate polyacrylamide gel electrophoresis). For this purpose, 30 μ g of protein were diluted to 20 μ L in RIPA buffer, 3 μ L DTT (1 M) and 7.5 μ L LDS sample buffer were added, and the solution was heated up to 95 °C for 5 min at 1,000 rpm. Samples were loaded onto a precast gradient SDS gel (4-10% gradient), and electrophoresis was performed at 140 V for approximately 2 h in MES SDS running buffer. Afterwards, samples were wet blotted onto a nitrocellulose membrane in Towbin buffer (25 mM Tris, 192 mM glycine, 20% methanol) at 400 mA for 2 h. Then, the membrane was blocked in 5% milk powder in TBS-T (50 mM Tris, 150 mM NaCl, 0.1% Tween®20, pH adjusted with HCl to 7.3-7.4) for 2 h at RT or at 4 °C overnight. Next, the membrane was incubated with the primary antibody in blocking solution at 4 °C overnight. The next day, the membrane was washed with TBS-T three times for 5 min. Then, the secondary antibody coupled to a horse-radish peroxidase (HRP) was applied for an incubation time of 1 h at RT. After another washing step (3x 5 min), the *Clarity Western* ECL substrate was used for detection. The solution was pipetted on top of the membrane, which was then transferred into a cassette. Protected from light, X-ray films were applied on top for around 30 s to 30 min depending on the sample and were developed to visualize bands.

2.7 Methylation Analysis

2.7.1 DNA Isolation

DNA from frozen tissue or cell pellets was isolated using the *NucleoSpin® Tissue* kit while DNA isolation from FFPE tissue was performed using the *Maxwell RSC DNA FFPE* Kit, both according to the manufacturer's instructions. Subsequently, DNA concentration and purity was measured on a *NanoDrop* UV-Vis spectrophotometer.

2.7.2 Methylation Array

For methylation analysis of mouse samples, at least 150 ng of total DNA were used for bisulfite conversion with the *EZ DNA Methylation* kit. Then, samples were analyzed on the *Infinium™ Mouse Methylation BeadChip* array covering >285,000 CpG sites within the mouse genome on an *iScan* array scanner. Human tumor samples were analyzed on the *MethylationEPIC 850k BeadChip* array, which covers >850,000 CpG sites within the human genome. The use of biopsy-specimens for research upon anonymization was always in accordance with local ethical standards and regulations at the University Medical Center Hamburg-Eppendorf.

2.7.3 Bioinformatic Analysis of Methylation Data

Data processing and analysis was performed with *R* (4.1.2) in collaboration with Dr. Melanie Schoof. For preprocessing of raw data and extraction of beta values, the *Minfi* package [192] was used for human data, whereas the *SeSaMe* package [193] was used for mouse data. Then, quantile normalization of data was performed. For a comparison of murine samples to human brain tumor DNA methylation profiles, previously published data by Capper *et al.* [101] and Sharma *et al.* [123] were combined with data generated in-house. Within the human dataset including all brain tumor entities, the 15,000 most differentially methylated CpG sites were identified. Out of these, all 640 CpGs which are orthologous between the human and mouse genome were chosen for further analysis. Human and mouse datasets were combined and again, quantile normalization was performed. UMAPs (Uniform Manifold Approximation and Projection for Dimension Reduction; [194]) as well as hierarchically clustered heatmaps (*Complex Heatmap* package [195]) were generated based on the differential methylation of the previously chosen 640 CpGs. For the generation of distance plots, Pearson correlation (*Stats* 4.1.2 package) was applied, and plots were generated with the *Complex Heatmap* package.

For a comparison of methylation profiles between mouse samples only, samples were preprocessed with *SeSaMe* and quantile normalized as described above. Principal Component Analysis (PCA) was performed with the *prcomp* function using the 10,000 most differentially methylated CpG sites. Gene Set enrichment analysis was applied using the *methyIGSA* package with *methyIRRA*

adjustment [196] with user supplied mapping between CpG ID and gene name in the mouse genome. GO terms associated with biological processes were summarized and visualized with REVIGO [197]. The resulting interactive graph was further adjusted using the *Cytoscape* software.

2.8 Gene Expression Analysis

2.8.1 RNA Isolation and Quality Control

RNA Isolation from FFPE tissue was performed using the *Maxwell RSC RNA FFPE* kit according to manufacturer's instructions. Prior to sequencing, RNA concentration and integrity was determined on an *RNA 6000 Nano Chip* on the *Agilent 2100 Bioanalyzer* system. The RNA Integrity Number (RIN) ranged between 2.0-2.8 for all FFPE samples, which indicated substantial RNA degradation but was considered sufficient in consideration of the isolation method.

2.8.2 RNA Sequencing

RNA sequencing was performed at the Leibniz-Institute of Virology sequencing facility in cooperation with Dr. Jacqueline Nakel and Kerstin Reumann. At least 100 ng total RNA per sample were used. In a first step, ribosomal RNA was depleted with the *RiboCop Human/Mouse/Rat V2* kit. Then, library preparation was performed using the *CORALL Total RNA-seq V2* kit. Pooled libraries were sequenced on a *NextSeq500* sequencing system by 1x75 bp single-end sequencing for 75 cycles, generating at least 30 Mio reads per sample.

2.8.3 Bioinformatic Analysis of RNA Sequencing Data

Bioinformatic processing and analysis of RNA sequencing data was performed in collaboration with Shweta Godbole and Prof. Dr. Julia Neumann (both Center for Molecular Neurobiology, Hamburg, Germany).

2.8.3.1 Data Preprocessing

Raw fastq files of mouse samples were processed in usegalaxy.eu [198]. Low quality reads were detected using *FastQC* (Galaxy Version 0.73+galaxy0), and *Trimmomatic* (Galaxy Version 0.38.1) was used for trimming poor quality reads (reads with average quality <20). Reads were aligned to the GRCm39 (mm39) mouse reference genome using *STAR aligner* (Galaxy Version 2.7.8a+galaxy1). Gene expression was quantified with *featureCounts* (Galaxy Version 2.0.1+galaxy2), and VST-normalized files were generated by *DEseq2* (Galaxy Version 2.11.40.7+galaxy2). Further processing of data was performed with *R* (v4.2.1). Human gene expression data were obtained from a previously published pediatric brain tumor cohort by Sturm *et al.* 2016 ([199]; GEO: GSE73038). To compare mouse and human gene expression data, 14,151 orthologous genes between both

datasets were used, and data was batch corrected for species differences using an in-house pipeline.

2.8.3.2 Differential Expression Analysis

The previously identified 14,151 orthologous genes were used for differential gene expression analysis between human tumor subtypes using *limma* (3.52.2) [200]. The 6,000 most differentially expressed genes were selected using Benjamini-Hochberg correction for multiple testing and sorting by F-statistic. When comparing to MB only, differential gene expression analysis was performed similarly within the human MB dataset, and the 5,000 most differentially expressed genes were used. Visualizations were performed using Rstudio packages *umap* (0.2.9.0) [194] and *Complex Heatmap* (2.12.1) [195] using Euclidian distance and Ward.D2 linkage for clustering. For the distance plots, Euclidean distance was measured (*Stats* 4.1.2 package), and plots were generated with *Complex Heatmap*.

Differential gene expression analysis between mouse samples only (control cerebellum, MYC/SMARCA4 tumors, and mouse MB, SHH) was performed using *limma*. Genes orthologous to humans were used for volcano plots generated with *ggplot2* (3.4.1) with genes considered differentially expressed if $\text{LogFC} \geq 2.5$ and FDR adjusted $p \leq 0.01$. For gene set enrichment analysis, all mouse genes with $\text{LogFC} \geq 1.5$ and FDR adjusted $p \leq 0.01$ were considered, and multiple packages from *clusterProfiler* (4.4.4) were applied for analysis and visualization.

2.9 Single-Cell Gene Expression Analysis

2.9.1 Preparation of Cells for Single-Cell RNA Sequencing

Single-cell RNA sequencing was performed on cerebellar cells from E16.5 embryos. Cells were isolated similarly to HPCs as described in section 2.4.9. This time, not the whole hindbrain but only the developing cerebellum was dissected. In parallel to cell isolation, genotyping of the embryos was performed using the HotSHOT protocol (see section 2.3.3.2) to enable the start of library preparation on the very same day. Cells were kept on ice after isolation until the genotypes were known. Then, three controls (cre-negative littermates) and three mutants (*Blbp-cre::Ctnnb1(ex3)^{fl/wt::Smarca4^{fl/fl}}*) were chosen for further processing. Cells were resuspended in FACS buffer (2% BSA, 0.02% Tween@20 in PBS), and 5 μL of 7-AAD solution per million of cells were added. After incubating in the dark for 5 to 7 min, cells were sorted with a *BD FACSAria Fusion* flow cytometer using the software *Diva 8.0.1*. For each sample, 1×10^5 living cells were sorted by excluding dead 7-AAD-positive cells. Before starting library preparation, the samples were pooled together in similar quantities to generate one control and one mutant sample.

2.9.2 Single-Cell Gene Expression Library Preparation and Sequencing

Preparation of single-cell gene expression libraries was performed at the Single Cell Core Facility of the University Medical Center Hamburg using the *Chromium Next GEM Single Cell 3' v3.1* kit (Dual index) with 40,000 cells of each pooled sample. Sufficient quality of the generated library was confirmed on a *TapeStation* with the *High Sensitivity D5000 ScreenTape®*. Subsequently, libraries were sent to Novogene (UK) for paired-end sequencing on a *NovaSeq 6000* sequencing system, mode *PE150*. More than 270 G raw data were generated for each sample.

2.9.3 Bioinformatic Analysis of Single-Cell Gene Expression Data

Bioinformatic analysis of single-cell RNA sequencing data was performed in cooperation with Dr. Michael Spohn (Bioinformatics Core, University Medical Center Hamburg-Eppendorf).

Raw sequencing reads in fastq format were aligned against a murine reference genome (*mm10-2020-A*, provided by 10x Genomics) and were simultaneously counted with the *Cell Ranger* pipeline (v7.0.1) [201] employing the count command. The output from *Cell Ranger* was loaded into *R* (v4.1.1) via the *Seurat* package (v4.0.5) [202], including only genes expressed in minimum three cells and cells expressing minimum 200 features. Control and mutant datasets were merged and further filtered to include only cells expressing more than 1500 and less than 7500 features, less than 5% mitochondrial genes, and less than 40,000 overall reads. The merged dataset was then normalized and scaled, and the PCA was calculated based on the 2,000 most variable genes. The first 50 dimensions and a resolution of 0.5 were chosen for UMAP and clustering. To annotate cell classes and subclasses in the resulting clusters, a label transfer method based on Stuart *et al.* 2019 [203] was chosen with the La Manno *et al.* 2021 [204] dataset as reference. Briefly, anchor cells between query dataset and reference are chosen in low dimensional PCA space, and labels are transferred by a weights matrix that defines the association between the query cells and the anchor cells and a binary matrix of the label and the anchor cells. Similarly, age of cells was predicted using the La Manno *et al.* 2021 dataset from E10.0 to E16.5 as a reference. The following modifications were performed for predicted subclasses: exclusion of subclasses with <10 cells; summary of 'meninges' (Pia1/2,3, intermediate meninges, dura, arachnoid); summary of 'microglia' (axon tract-associated microglia, cycling microglia, non-cycling microglia); undefined cells with prediction class 'blood' also defined as 'blood' in subclasses. Cell cycle scores were assigned using the *CellCycleScoring* tool in *Seurat*.

2.10 Statistical Analysis

All statistical analysis was performed using the *GraphPad Prism (9.4.1)* software. The statistical tests applied to the data shown are all stated in the respective figure legends. For each comparison, at least $n=3$ samples per group were used and/or $n=3$ independent experiments were conducted. When comparing two groups only, two-tailed unpaired Welch's t-test or in case of paired data, two-tailed paired t-tests were performed. When normal distribution of samples could not be assumed, Wilcoxon (matched-pairs) signed-rank test was applied. For comparisons between more than two groups, Tukey's multiple comparisons tests after ANOVA was applied unless otherwise stated. The Chi-Square test was applied when comparing expected vs. counted values in mouse breeding. P-values were always corrected for multiple testing when more than two groups were compared. All graphs depict mean values \pm standard deviation unless otherwise stated.

3 RESULTS

3.1 Characterization of SMARCA4 Variants *in vitro*

In order to characterize the effect of mutant SMARCA4 on cell proliferation *in vitro*, we generated lentiviral constructs for the overexpression of either wildtype SMARCA4 or mutant variants SMARCA4 T910M and SMARCA4 R1135W. Both alterations are commonly detected as heterozygous missense mutations in MB [70, 125]. They are proposed to exert a dominant-negative function, leading to a loss of function despite the presence of a second functional *SMARCA4* allele [44]. Consequently, an overexpression of mutated SMARCA4 variants in *SMARCA4* wildtype cells should have a similar effect. This was our rationale for exploring the influence of overexpressed mutant SMARCA4 variants on cell viability of *SMARCA4* wildtype MB cell lines *in vitro*. Subsequently, a comparison to a full SMARCA4 knockdown in MB cell lines induced by shRNA was performed.

3.1.1 Reintroduction of SMARCA4 inhibits proliferation of SCCOHT-1 cells

We tested functionality of the generated lentiviral constructs carrying either wildtype or mutant SMARCA4 in the small cell carcinoma of the ovary, hypercalcemic type SCCOHT-1 cell line. This cell line carries a biallelic loss of *SMARCA4*, which was previously shown to be essential for cell proliferation [205]. In consequence, re-expression of SMARCA4 should reduce cell viability. Indeed, reintroduction of wildtype SMARCA4 with our lentiviral construct significantly reduced proliferation in successfully transduced cells as assessed by BrdU incorporation in IF staining three days after transduction (Fig. 5A-B). Meanwhile, transduction with mutant SMARCA4 (T910M) did not result in reduced proliferation, indicating that the introduced mutation results in a loss of function. Transduction of SCCOHT-1 with a 1:1 mixture of both wildtype and the T910M mutant construct resulted in no effect on proliferation either, hinting towards a dominant-negative effect of the SMARCA4 mutant. As a control, HEK293T cells with functional SMARCA4 were transduced using the same constructs. In this case, the fluorescence signal of the mCherry protein signal encoded by all lentiviral constructs was used to detect transduced cells in a BrdU/mCherry co-staining. Altogether, no alteration in cell proliferation was observed after transduction of HEK293T with any of the SMARCA4 variants, hereby confirming the previously seen effect in SCCOHT-1 cells was tumor cell-type specific (Fig. 5C).

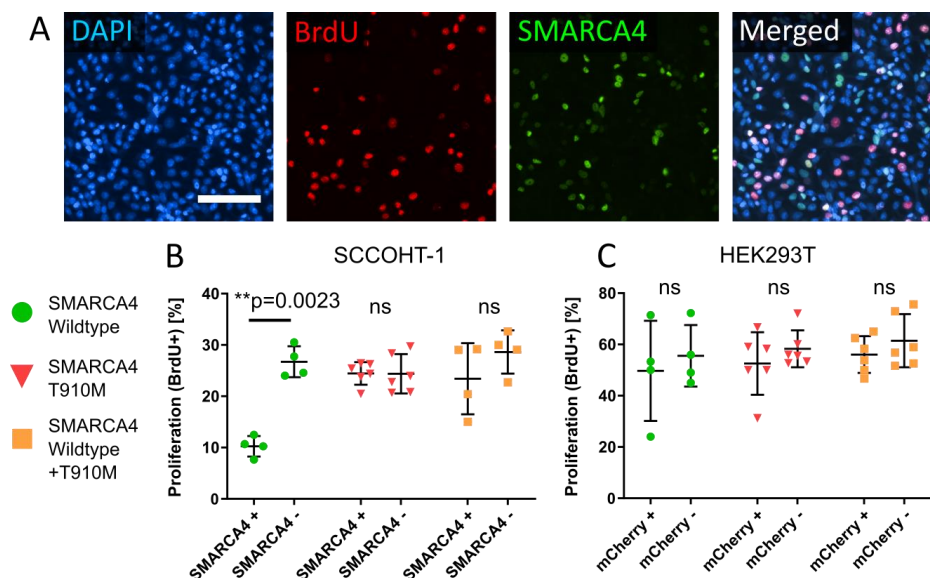


Figure 5. Reintroduction of SMARCA4 wildtype but not SMARCA4 T910M inhibits proliferation of SCCOHT-1 cells. (A) BrdU/SMARCA4 IF staining of SCCOHT-1 cells 72 h after transduction with SMARCA4 wildtype. (B, C) Proliferation of SCCOHT-1 (B) and HEK293T cells (C) measured by BrdU incorporation in IF 72 h after transduction with either wildtype SMARCA4, SMARCA4 T910M, or a 1:1 mixture of both constructs counted separately in SMARCA4-positive (SMARCA4+) and negative (SMARCA4-) cells. A two-tailed paired t-test was applied (ns=not significant). Scale bar in A corresponds to 100 μ m.

3.1.2 Overexpression of mutant SMARCA4 does not influence proliferation of MB cell lines or primary murine granule cell precursors

In a next step, we wanted to evaluate the effect of mutant SMARCA4 specifically in MB, an entity in which both SMARCA4 variants T910M and R1135W have been identified in patients as heterozygous missense mutations [70, 106, 125, 126]. For this purpose, three different non-WNT/non-SHH medulloblastoma cell lines (D283, D341, D425) were transduced with either wildtype SMARCA4, mutant SMARCA4 (T910M or R1135W), or a 1:1 mixture of both wildtype and one of the mutant constructs. Beforehand, the absence of *SMARCA4* mutations in the original cell lines was confirmed by targeted sequencing of *SMARCA4*. Transduction with a Mock construct carrying only mCherry fluorescence was performed as an additional control. After selection for successfully transduced cells through FACS (suspension cell lines D341 and D425) or zeocin selection (adherent cell line D283), all cells showed a positive mCherry signal (Fig. 6A-C). Overexpression of SMARCA4 was confirmed by Western Blot (Fig. 6D). Viability of the selected cell lines was measured after re-seeding in 96-well plates using the *Cell Titer Glo Viability Assay*. Overall, no difference in cell viability was observed in any of the three MB cell lines overexpressing either wildtype or mutant SMARCA4 (Fig. 6E-G).

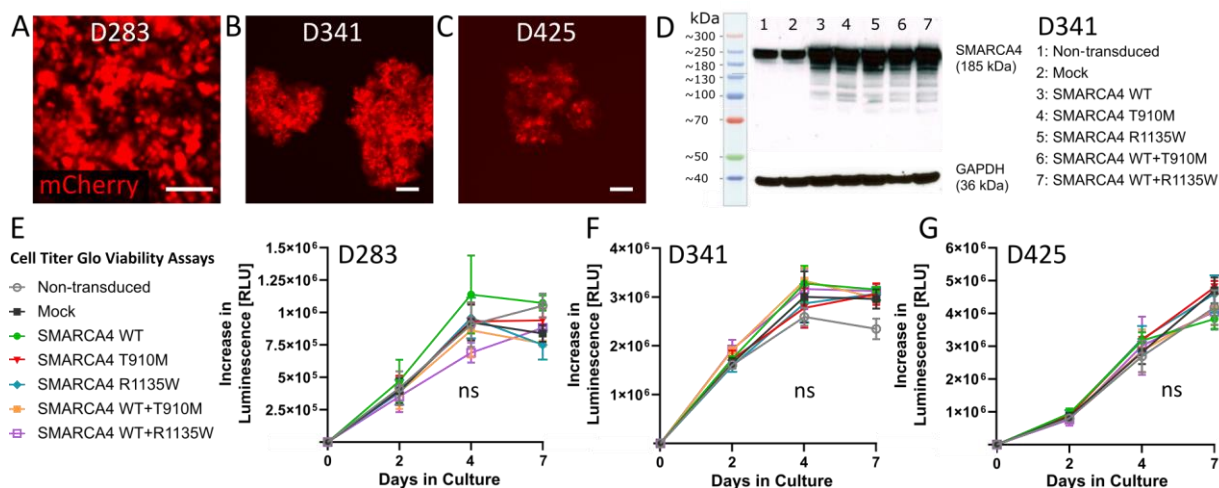


Figure 6. Overexpression of wildtype or mutant SMARCA4 does not alter viability of MB cell lines. (A) Live mCherry signal after Zeocin selection of D283 cells transduced with SMARCA4 wildtype. (B, C) Live mCherry signal after FACS sorting of D341 and D425 cells transduced with SMARCA4 wildtype. (D) Overexpression of SMARCA4 variants in transduced cells is visible in Western Blot, exemplarily shown for D341. (E, F, G) The *Cell Titer Glo Viability Assay* was applied to all cell lines after selection/sorting in three independent experiments each with four technical replicates for each experiment and condition. Increase in luminescence relative to measurement at day 0 after seeding was measured at day 2, 4, and 7 in culture. Altogether, no difference in cell viability was observed after transduction with Mock or any of the SMARCA4 constructs. Tukey's multiple comparison test was applied. Scale bars in A, B, and C correspond to 100 μ m. Mock = mCherry construct. Legend in E also applies to F and G.

In a next step, we evaluated the influence of overexpressed SMARCA4 variants on proliferation of primary murine GCPs, the cells of origin used in several previously described Group 3 MB mouse models [176, 206, 207]. Successful transduction and proliferation of cells was measured by IF staining for mCherry and BrdU three days after transduction (Fig. 7A). In three independent experiments, no difference in proliferation of GCPs was observed irrespective of the introduced SMARCA4 construct (wildtype, SMARCA4 T910M, or SMARCA4 R1135W) (Fig. 7B).

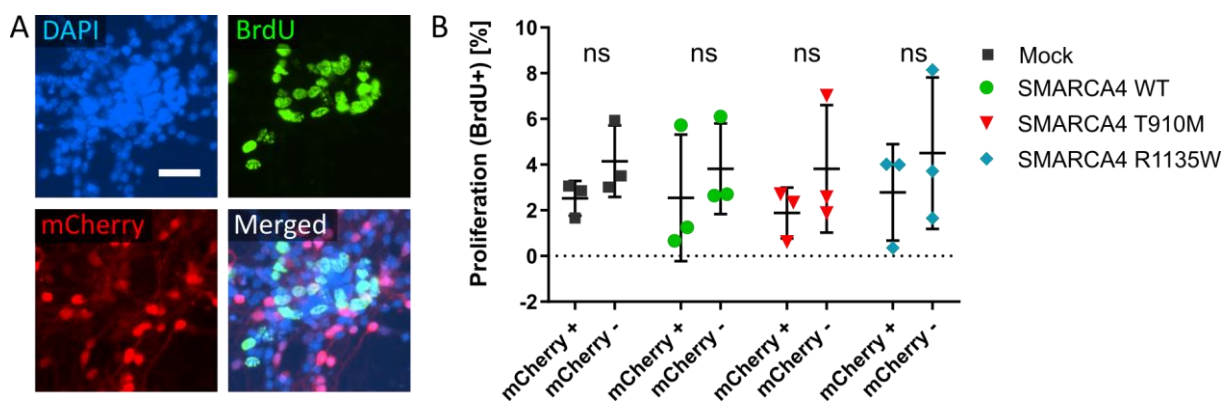


Figure 7. Overexpression of wildtype or mutant SMARCA4 does not alter proliferation of primary murine granule cell precursors (GCPs). (A) BrdU/mCherry IF staining of GCPs derived from 7-day-old *C57Bl/6/J* wildtype mice 72 h after transduction with SMARCA4 R1135W construct. (B) Proliferation measured by BrdU incorporation in IF, separately counted for mCherry-positive and negative cells in each condition (n=3). Paired two-tailed t-test was applied. Scale bar in A corresponds to 25 μ m.

3.1.3 SMARCA4 knockdown with shRNAs does not increase proliferation of MB cell lines

Similar to the overexpression of mutant SMARCA4 variants that are associated with a loss of function, a complete knockdown of SMARCA4 might accurately model the effects of *SMARCA4* alterations in MB. Consequently, we transduced our three MB cell lines with the lentiviral LeGO-iC2Zeo+-hSMARCA4shRNA construct to introduce a knockdown of SMARCA4. As a control, cell lines were transduced with a LeGO-iC2Zeo+-scrRNA construct containing a scrambled small hairpin RNA (scrRNA) with a randomly rearranged sequence. Again, both constructs contained mCherry as a selection marker. Knockdown of SMARCA4 after transduction was confirmed in IF staining 72 h after transduction with shRNA, which was not detected after transduction with scrRNA (Fig. 8A-B). Then, successfully transduced mCherry-positive cells were selected by FACS and reseeded in 96-well plates to evaluate cell viability using the *Cell Titer Glo Viability Assay*. Altogether, knockdown of SMARCA4 by shRNA did not increase cell viability of any of the three MB cell lines (Fig. 8C-E). However, statistical analysis could not be performed since only one experiment for each cell line was performed. Then, termination of the experiment was decided due to missing pro-oncogenic effects and considering new advances in the other two project parts, which were preferentially continued.

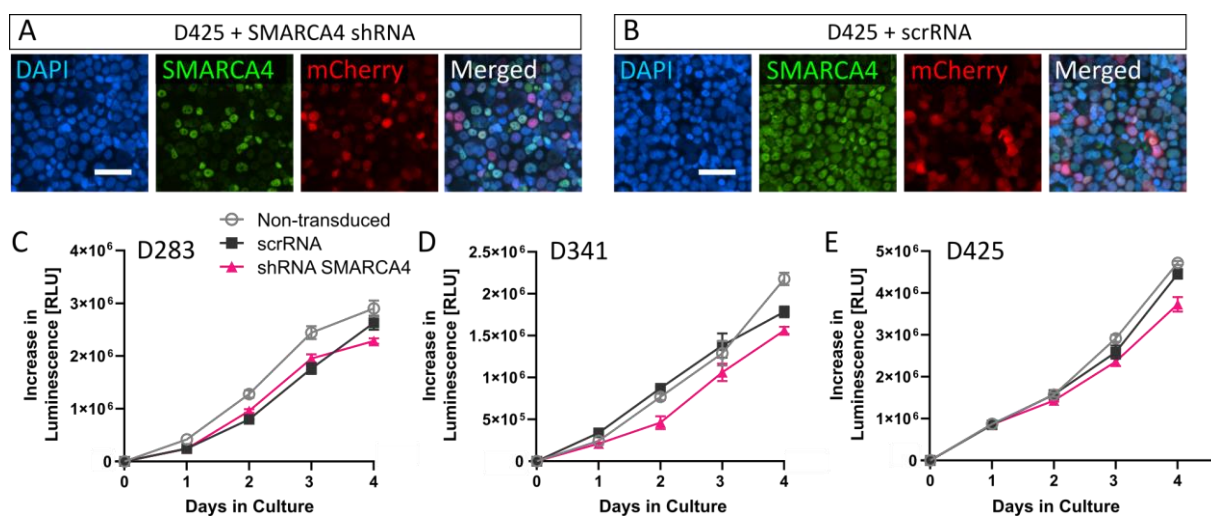


Figure 8. Knockdown of SMARCA4 does not increase viability of MB cell lines. (A) IF staining of cytopins 72 h after transduction of D425 with a SMARCA4 shRNA construct reveals SMARCA4 loss in mCherry-positive cells, which is not visible in controls transduced with scrRNA constructs (B). (C,D,E) *Cell Titer Glo Viability Assay* was applied to all cell lines after sorting in one experiment with four technical replicates for each condition. Increase in luminescence relative to measurement at day 0 after seeding was measured at day 2, 4, and 7 in culture. Altogether, no relevant difference in cell viability was observed after transduction with either scrRNA or SMARCA4 shRNA constructs. No statistics were applied as only one experiment each was performed (error bars show SD of four replicates each within the experiments). Scale bar in A and B corresponds to 50 μm. Legend in C also applies to D and E.

Taken together, we did not detect any effect on cell viability caused by the overexpression of SMARCA4 variants T910M and R1135W in both MB cell lines and primary GCPs. Similarly, first results on SMARCA4 knockdown by shRNA in MB cell lines do not indicate increased proliferation after SMARCA4 loss.

3.2 SMARCA4 in the Development of Group 3 Medulloblastoma

Although several Group 3 MB mouse models have been developed so far, none of these involve alterations of *SMARCA4*, which is among the most frequently mutated genes in this subgroup [70, 106]. Kawauchi *et al.* previously demonstrated development of Group 3-like MB after transplantation of p53-deficient and MYC-overexpressing GCPs into immunodeficient mice [176]. To uncover mechanisms by which mutations in *SMARCA4* drive formation of Group 3 MB, we used a similar approach by combining a loss of SMARCA4 with the overexpression of MYC in GCPs. While MYC amplifications and *SMARCA4* mutations occur in around 15-20% and 9-15% of Group 3 MBs, respectively, the combination of both alterations can be found in around 2% of cases [70, 106, 127].

Effects of *Smarca4* and *Myc* alterations in GCPs were studied both *in vitro* and *in vivo* by subsequent transplantation in immunodeficient mice. The resulting tumors were analyzed both histologically and molecularly to test comparability to human MB.

3.2.1 Loss of SMARCA4 or MYC overexpression does not increase proliferation of GCPs *in vitro*

To induce a loss of SMARCA4 in GCPs, *Math1-creERT2::Smarca4^{f/f}* mice received a single dose of tamoxifen (0.4 mg) at P3. GCPs were isolated from the cerebella when pups reached an age of 7-8 days. Successful knockdown of SMARCA4 was validated in Western Blot (Fig. 9A) and IF stainings (Fig. 9B). Cell counts within 19 independent experiments revealed the absence of SMARCA4 protein in around 50% of cells (Fig. 9C). Proliferation measured by BrdU incorporation showed significantly decreased proliferation in SMARCA4-negative cells at day 1 in culture (Fig. 9D). No significant difference in proliferation was observed at day 3 or 5 in culture. Next, we analyzed the effect of MYC overexpression in GCPs by transducing cells with a lentiviral MYC-GFP construct 4 h after isolation. Successful transduction was validated 72 h after transduction by the presence of MYC protein in Western Blot and by positive GFP IF stainings (Fig. 9E+F). Mean transduction rates ranged between 15.5 – 22.6% with no significant difference between GCPs of different genotypes and with or without tamoxifen administration (Fig. 9G). Overall proliferation of non-induced *Math1-creERT2::Smarca4^{f/f}* GCPs after transduction with MYC virus showed no difference compared to proliferation of cells transduced with a Mock-GFP construct in BrdU IF staining 72 h after

transduction (Fig. 9H). Similarly, when combining both SMARCA4 loss and MYC overexpression by transducing *Math1-creERT2::Smarca4^{fl/fl}* GCPs after tamoxifen-induced SMARCA4 knockdown, no significant difference in overall proliferation was observed (Fig. 9I). In IF stainings, the presence of a SMARCA4-negative and successfully transduced GFP-positive subpopulation was shown, making up around 8.4% of the whole cell culture (Fig. 9J-K).

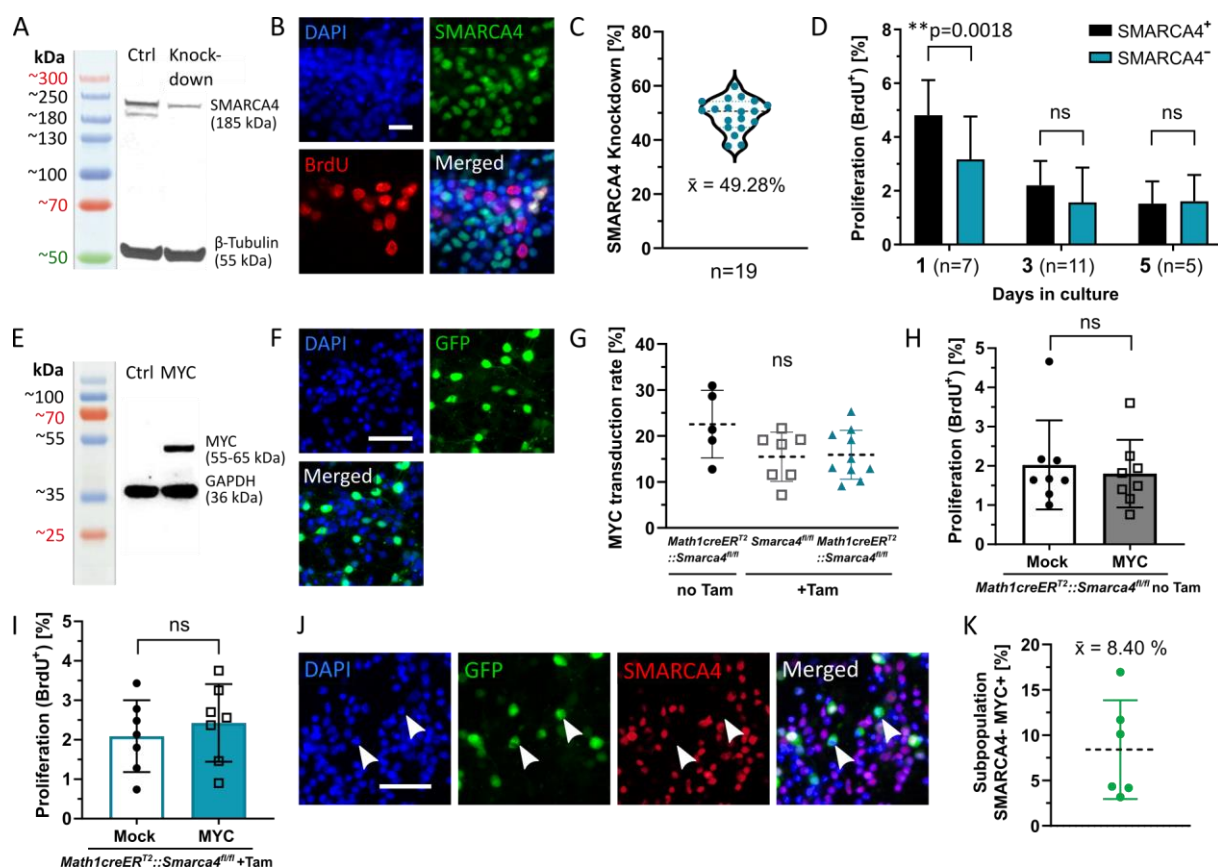


Figure 9. Loss of SMARCA4 and MYC overexpression does not increase proliferation of granule cell precursors (GCPs) *in vitro*. (A) Tamoxifen-induced knockdown of SMARCA4 is evident in Western Blot of P7/8 *Math1-creERT2::Smarca4^{fl/fl}* GCPs compared to controls (*Smarca4^{fl/fl}*) after tamoxifen injection at P3. (B) IF staining of knockdown GCPs at day 3 in culture shows loss of SMARCA4 protein and proliferation indicated by BrdU incorporation. (C) Evaluation of SMARCA4 knockdown in IF on day 3 in culture of 19 independent GCP cultures. (D) Proliferation as measured by BrdU incorporation in IF on day 1, 3, and 5 in culture, separately counted for SMARCA4-positive and -negative GCPs in knockdown cultures. Two-tailed paired t-tests were applied. (E) MYC expression is evident in Western Blot of wildtype P7/8 GCPs 72 h after transduction. (F) IF staining shows GFP signal 72 h after transduction of GCPs. (G) MYC transduction rates were evaluated in IF stainings of GCPs 72 h after transduction. The three groups include GCPs without tamoxifen (Tam) induction and GCPs of cre-negative (*Smarca4^{fl/fl}*) and cre-positive (*Math1-creERT2::Smarca4^{fl/fl}*) genotype after tamoxifen induction at P3. Tukey's multiple comparisons test was applied. (H,I) Proliferation as measured by BrdU incorporation in IF of *Math1-creERT2::Smarca4^{fl/fl}* GCPs without (H) or with tamoxifen-induced SMARCA4 knockdown (I) 72 h after transduction with Mock or MYC constructs. Paired two-tailed t-tests were applied. (J) GFP/SMARCA4 IF staining shows subpopulation with SMARCA4 protein loss and GFP signal (white arrowheads) 72 h after MYC transduction of knockdown GCPs. (K) Fraction of SMARCA4-negative GFP-positive subpopulation in IF. Scale bar in B corresponds to 20 μ m, scale bars in F+J correspond to 50 μ m.

3.2.2 Loss of SMARCA4 and MYC overexpression cooperate to drive brain tumor formation in mice

We showed no increased proliferation of GCPs after SMARCA4 knockdown and MYC overexpression *in vitro*. However, proliferation of distinct subpopulations could not be analyzed separately. Additionally, surrounding extracellular matrix or paracrine effects of other cell types present in an *in vivo* microenvironment significantly influence cell behavior [208]. Therefore, we decided to transplant altered GCPs into immunodeficient *CD1^{nu/nu}* mice to further explore the tumorigenic potential of combined *Smarca4* and *Myc* alterations *in vivo*. For this purpose, SMARCA4 knockdown GCPs were isolated from induced *Math1-creER^{T2}::Smarca4^{f/f}* mice and were transduced with a lentiviral MYC construct 4 h after plating as before. On the next day, cells were dissociated, resuspended in medium with matrigel (3:1) and were transplanted into the cerebella of *CD1^{nu/nu}* mice using a stereotactic frame (Fig. 10A). Within a cohort of 19 transplanted mice, five mice developed a tumor in the cerebellum, presenting with neurological symptoms earliest four weeks and latest five months after transplantation (Fig. 10B). Histologically, tumors presented as a cell dense mass in HE stainings, with regions showing anaplastic features as well as apoptotic areas (Fig. 10C-E). IHC stainings revealed a loss of SMARCA4 in all tumor cells (Fig. 10F). The presence of recombined *Smarca4* in tumor biopsies was also verified by PCR, which confirmed that the loss of SMARCA4 was caused by genetic recombination rather than other tumor-related mechanisms (Fig. 10G). Furthermore, tumors stained positive for both GFP and MYC, thereby validating successful transduction with the MYC-GFP construct (Fig. 10H+I). Tumors were highly proliferative and displayed a high degree of apoptosis as indicated by cleaved caspase-3 (CC3) staining (Fig. 10J+K). Staining for neural markers revealed scattered expression of SOX2 and Nestin, while no signal for NeuN or OLIG2 was detected (Fig. 10L-O). Altogether, these results affirmed the origin of detected tumors in the small subpopulation of *Smarca4* recombined MYC overexpressing GCPs and showed proliferative capacity as well as undifferentiated nature of tumors.

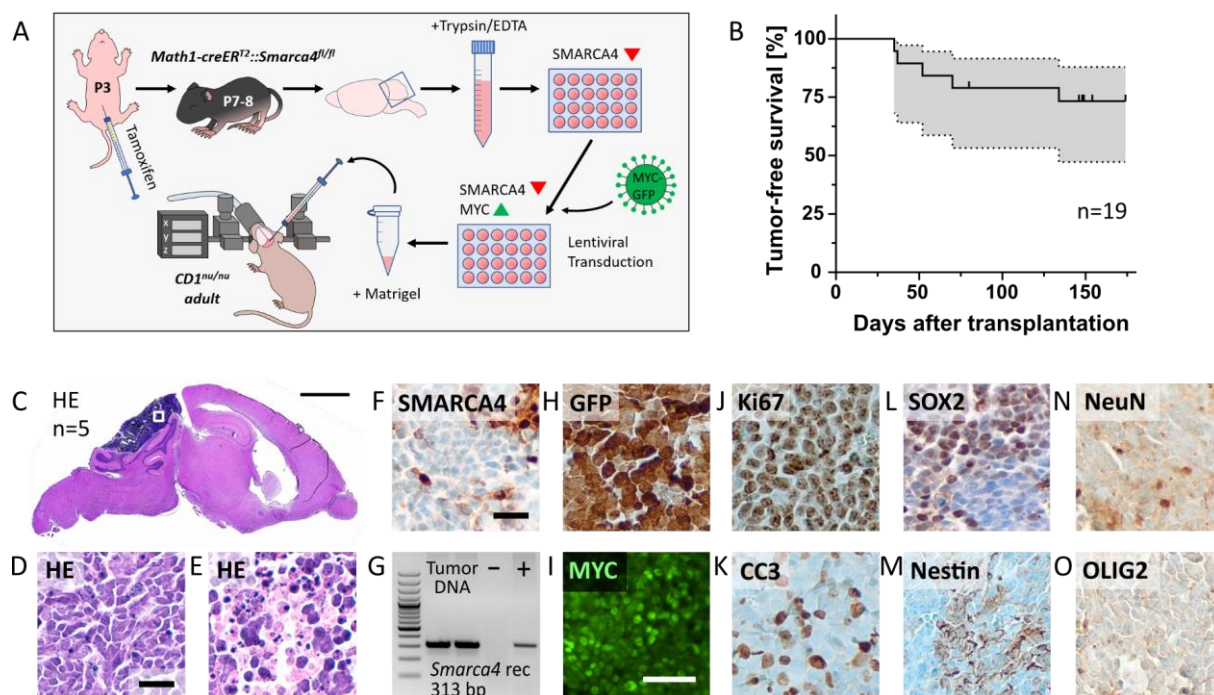


Figure 10. Loss of SMARCA4 and MYC overexpression cooperate to drive brain tumor formation in mice. (A) Schematic overview of the cell culture and transplantation protocol for the generation of SMARCA4-deficient MYC-overexpressing tumors. (B) Tumor-free survival of transplanted $CD1^{nu/nu}$ mice; grey area represents the 95% confidence interval. Censored mouse at day 80 had to be sacrificed due to illness unrelated to tumor development. (C) Representative HE staining of observed tumors in the brains of n=5 transplanted mice in sagittal brain section. (D,E) High-power HE stainings of distinct areas within the tumors showing anaplastic (D) or apoptotic (E) features. (F) Tumors show a complete loss of SMARCA4 in IHC. (G) PCR for recombined *Smarca4* in DNA isolated from tumor biopsies confirms *Smarca4* recombination on a genetic level. (H-I) Tumors stain positive for GFP (H) and MYC (I), confirming transduction with the MYC-GFP construct. (J-K) Tumors are highly proliferative as indicated by Ki67 stainings (J) with a high degree of apoptosis according to Cleaved Caspase-3 (CC3) signals (K). (L-O) Tumors show scattered expression of SOX2 (L) and Nestin (M) but no signal for NeuN (N) or OLIG2 (O). Scale bar corresponds to 2 mm in C, to 25 μ m in D + F (also applicable to E, H, J-O), and to 50 μ m in I.

3.2.3 Gene set enrichment analysis in MYC/SMARCA4 tumors

To characterize MYC/SMARCA4 tumors on a molecular level, we performed RNA sequencing using FFPE biopsy punches of four mouse tumors. As a control, we simultaneously sequenced FFPE-derived RNA of a previously established SHH MB mouse model (*Math1-cre::Smo^{fl/wt}* [209]) and of *Math1-creER^{T2}::Smarca4^{fl/fl}* P7 whole cerebella representing the cellular origin of tumors. The comparison of MYC/SMARCA4 tumors to *Math1-creER^{T2}::Smarca4^{fl/fl}* cerebella revealed *Myc* as the most significantly upregulated gene in our model (Suppl. Fig. 1A). Gene set enrichment analysis revealed downregulation of terms associated with neuronal development and differentiation, while upregulated terms were mainly associated with ribosome biogenesis and ribosomal RNA (rRNA) synthesis and processing, a characteristic hallmark for MYC-driven cancers [210] (Suppl. Fig. 1B,C). Comparison of gene expression profiles of MYC/SMARCA4 tumors to the established SHH MB mouse model again confirmed upregulation of *Myc*, while *MycN* as a target of SHH signaling was significantly downregulated (Fig. 11A, Suppl. Table 2). Other downregulated genes included *Atoh1* and *Barhl1*, both markers for granule cells, of which low levels of *BARHL1* have been associated with a less favorable prognosis in MB [211]. On the other hand, *Hoxa5* and *Fabp4*, both associated with increased malignancy in glioblastoma tumors, were upregulated in MYC/SMARCA4 tumors [212, 213]. Gene set enrichment analysis revealed downregulated GO terms mostly associated with neuronal development (Fig. 11B). Meanwhile, terms associated with transmembrane transport and synaptic signaling were upregulated in our model (Fig. 11C). Pathway analysis confirmed the downregulation of SHH signaling but also reduction of Notch and PI3K-Akt-mTOR signaling, whereas glycolysis/gluconeogenesis as well as G protein signaling pathways were upregulated in MYC/SMARCA4 tumors (Fig. 11D+E).

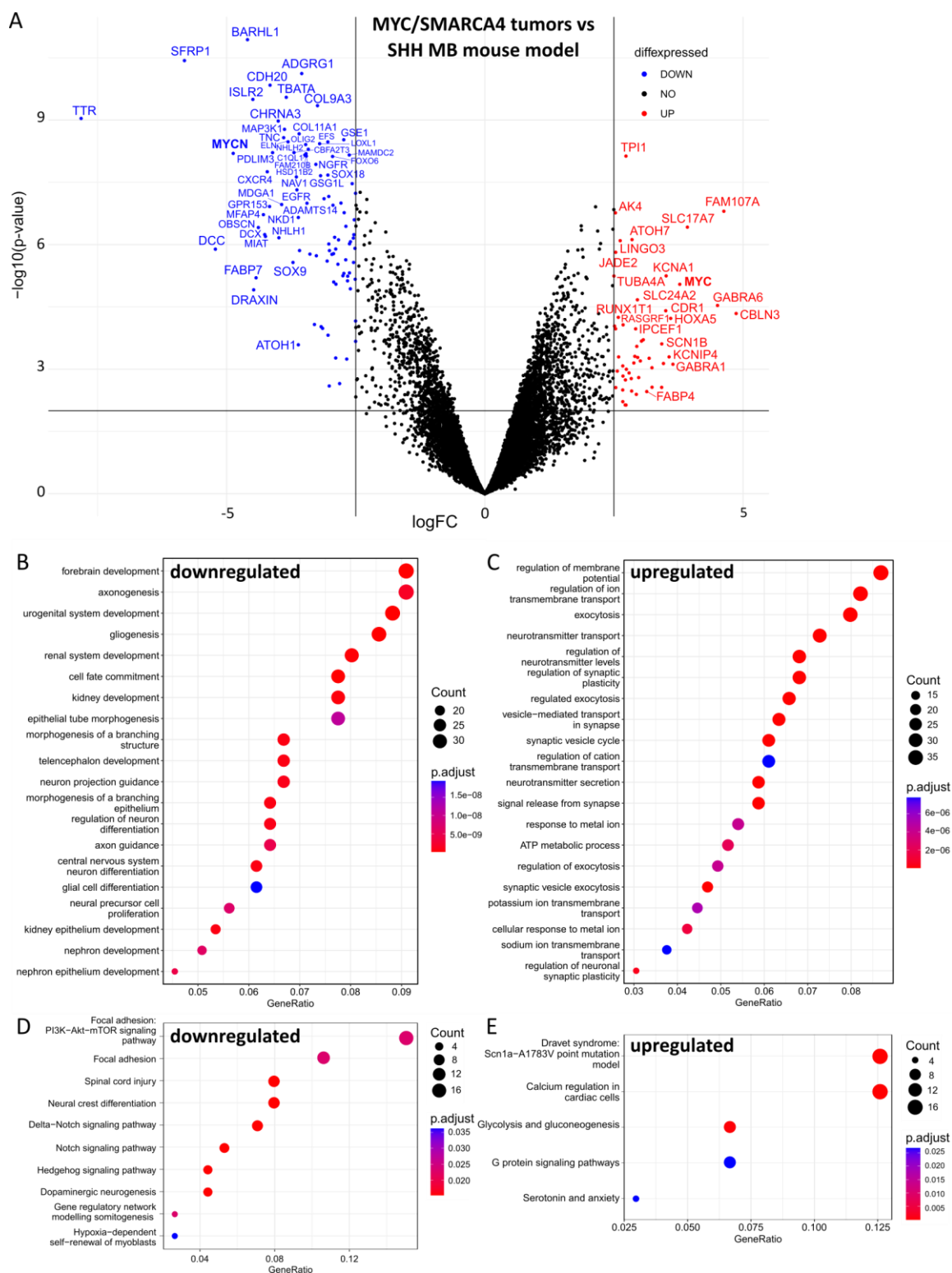


Figure 11. Differential gene expression of MYC/SMARCA4 tumors compared to mouse SHH MB model. (A) Volcano plot depicting differential gene expression between MYC/SMARCA4 tumors ($n=4$) and the *Math1-cre::Smo^{fl/wt}* SHH MB mouse model ($n=3$) as assessed by RNA sequencing analysis. Only genes orthologous in mouse and humans were visualized, and differential expression with $\log_{2}FC \geq 2.5$ and $p \leq 0.01$ was considered significant (blue/red coloring) after Benjamini-Hochberg correction (detailed list included as Supplementary Table 2). (B,C) Gene set enrichment analysis considering all significantly differentially expressed mouse genes with $\log_{2}FC \geq 1.5$ and $p \leq 0.01$. (D,E) Deregulated wiki pathways considering all significantly differentially expressed mouse genes with $\log_{2}FC \geq 1.5$ and $p \leq 0.01$. $\log_{2}FC$ = log fold change; count = count of significantly deregulated genes; GeneRatio = count/size of gene set; p.adjust = adjusted p-value.

3.2.4 MYC/SMARCA4 tumors show molecular resemblance to human Group 3 MB

In a next step, we integrated our RNA sequencing data with previously published gene expression data to test comparability of our mouse tumors to human brain tumors. An integration with a data set comprising several pediatric brain tumor entities (Sturm *et al.* 2016 [199]) revealed resemblance of our model to human MB in both UMAP and Euclidian clustering (Fig. 12A-B). While mouse SHH MB serving as a validation always displayed closest proximity to human SHH MB, MYC/SMARCA4 tumors showed similarity to both SHH MB and Group 3/4 MB in both approaches. A distance plot analysis considering mean values for each subgroup indicated closest proximity of both mouse SHH MB and our MYC/SMARCA4 tumors to human SHH MB (Fig. 12C). Based on these results, we decided to further evaluate the similarity to specific MB subgroups by comparing our mouse model exclusively to MB samples. Within the human MB cohort, we again performed gene expression analysis to identify the most differentially expressed genes between MB subgroups. This time, an integration of our mouse data with human data resulted in closest similarity of our model to Group 3 MB in both UMAP and Euclidian clustering, whereas mouse SHH MB reliably clustered with human SHH MB (Fig. 12D-E). In both approaches, one out of four tumors of our model formed an exception by clustering closely with SHH MB. Distance plot analysis further confirmed closest proximity of MYC/SMARCA4 tumors to Group 3 MB (Fig. 12F).

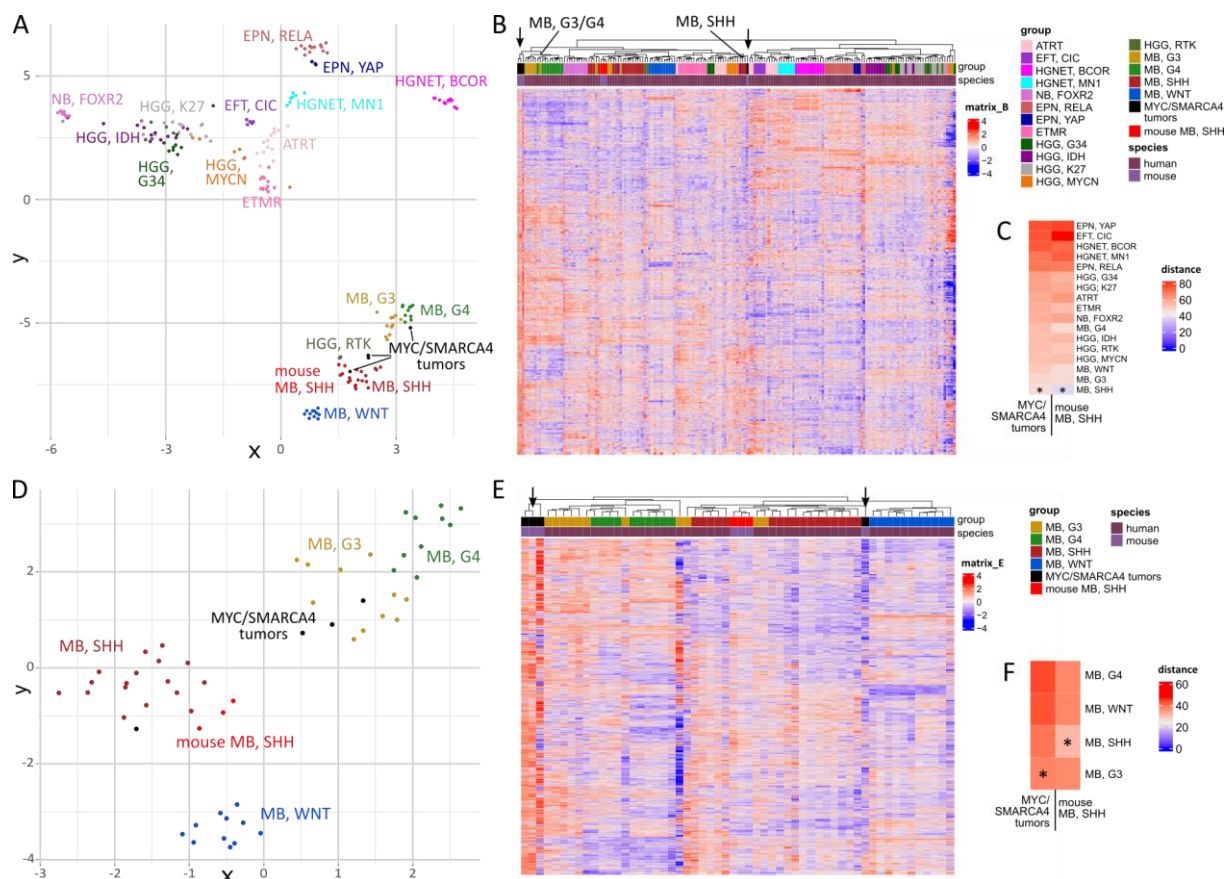


Figure 12. MYC/SMARCA4 tumors show similarities to Group 3 MB in gene expression analysis. (A) UMAP clustering of mouse tumors profiled by RNA sequencing and published expression data of pediatric brain tumors (Sturm *et al.* 2016 [199]). Out of the 14,151 orthologous genes identified between both datasets, the 6,000 most differentially expressed genes within the human dataset were used for clustering. Mouse MB, SHH show resemblance to their human counterpart MB, SHH, whereas MYC/SMARCA4 tumor model displays similarity to both MB, SHH and MB, Group 3/4 (G3/4). (B) Hierarchical clustering according to the same gene set shows proximity of MYC/SMARCA4 tumors to the MB, G3/4 cluster for three samples, whereas the remaining sample clusters with a subset of MB, SHH (black arrows). (C) Distance plot shows closest resemblance of both mouse tumor models to MB, SHH. (D) UMAP clustering of mouse tumors and human MB subgroups only (Sturm *et al.* 2016) according to the 5,000 most differentially expressed genes within the human MB dataset out of 14,151 orthologous genes. MYC/SMARCA4 tumors appear closest to MB, Group 3 tumors. (E) Hierarchical clustering according to the same gene set confirms proximity of MYC/SMARCA4 tumors to the MB Group 3/4 cluster with one exception (black arrows). (F) Distance plot shows closest resemblance of MYC/SMARCA4 tumors to MB, Group 3. EFT, CIC = Ewing sarcoma family tumor with *CIC* alteration; HGNET, BCOR = High-grade neuroepithelial tumor with *BCOR* alteration; NB, FOXR2 = neuroblastoma with *FOXR2* activation; EPN, RELA = ependymoma with *RELA* fusion; EPN, YAP = ependymoma with *YAP* fusion; ETMR = embryonal tumor with multilayered rosettes; HGG, G34 = *H3F3A* G34 mutant high-grade glioma; HGG, IDH = *IDH* mutant high-grade glioma; HGG, K27 = *H3F3A* K27 mutant diffuse midline glioma; HGG, MYCN = *MYCN*-amplified high-grade glioma; HGG, RTK = *IDH/H3F3A* wild-type high-grade glioma of the receptor tyrosine kinase (RTK) subtype.

Human brain tumors and biologically relevant tumor subgroups can be reliably classified according to their DNA methylation profile [101]. Therefore, we isolated DNA of three mouse tumors and performed global DNA methylation analysis using the *Mouse Methylation Bead Chip* for an additional confirmation of our observations. These data were integrated with a human MB dataset comprising in-house analyzed samples and previously published cohorts (Capper *et al.* [101], Sharma *et al.* [123]). Out of the 15,000 most differentially methylated CpG sites within the human

cohort, 640 CpG sites orthologous in humans and mice were chosen for further analysis. UMAP and Euclidian clustering according to differential methylation of these 640 CpG sites showed good separation of human MB subgroups, with MYC/SMARCA4 tumors clustering in close proximity to Group 3/4 MB (Fig. 13A-B). A distance plot confirmed highest resemblance of MYC/SMARCA4 tumors to Group 3 MB (Fig. 13C).

Taken together, molecular analysis of our tumors using both gene expression and DNA methylation data confirmed similarities to human MB, with closest resemblance to pediatric Group 3 MB.

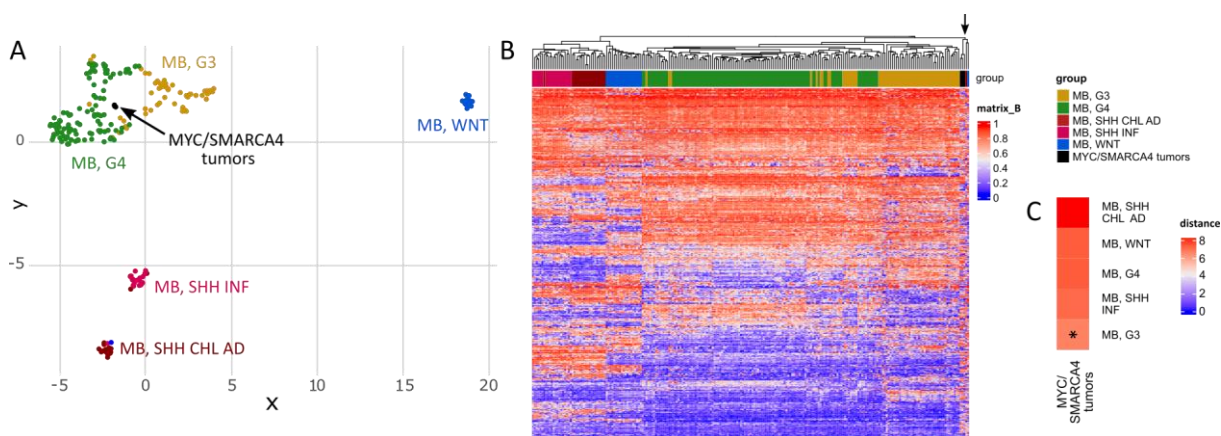


Figure 13. MYC/SMARCA4 tumors show similarities to Group 3/4 MB in DNA methylation analysis. (A) UMAP clustering according to DNA methylation of mouse tumors (*Illumina Mouse Methylation BeadChip*) and human MB (Capper *et al.* 2018 [101], Sharma *et al.* 2019 [123], in-house analyzed samples, n=228) using 640 orthologous CpG sites out of the 15,000 most differentially methylated CpG sites within the human dataset. Mouse MYC/SMARCA4 tumors (n=3) show most similarity to MB, Group 3/4. (B) Heatmap clustering according to DNA methylation of the same samples and CpG sites similarly shows proximity of the MYC/SMARCA4 tumors to MB, Group 3/4 (black arrow). (C) Distance Plot using the mean methylation values summarized for every subgroup shows lowest distance of MYC/SMARCA4 tumors to MB, Group 3. MB, SHH CHL AD = medulloblastoma SHH-activated (children and adults); MB, SHH INF = medulloblastoma SHH-activated (infants).

3.3 SMARCA4 in the Development of WNT Medulloblastoma

SMARCA4 is one of the most commonly altered genes in WNT MB. Nevertheless, no mouse model has investigated the role of *SMARCA4* mutations in tumor development yet. Gibson *et al.* induced formation of WNT MB in the brain stem of mice by combining a stabilizing mutation in the β -catenin gene *Ctnnb1* that activates WNT signaling with a loss of tumor suppressor p53 (*Blbp-cre::Ctnnb1(ex3)^{fl/wt}::Trp53^{fl/wt}*) [105]. Therefore, we combined the same promoter and β -catenin mutation with a loss of SMARCA4 in our *Blbp-cre::Ctnnb1(ex3)^{fl/wt}::Smarca4^{fl/fl}* model.

3.3.1 Severe developmental phenotypes and early lethality of *Blbp-cre::Ctnnb1(ex3)^{fl/wt}* mice

Surprisingly, *Blbp-cre::Ctnnb1(ex3)^{fl/wt}* mice developed a severe phenotype in our study with a median survival of only two days (Fig. 14A). All mice were either found dead shortly after birth (n=10) or had to be sacrificed due to ataxia and hydrocephalus within the first three weeks of life (n=8). This phenotype had not been observed by other groups that used *Blbp-cre::Ctnnb1(ex3)^{fl/wt}* mice for breeding without showing any evidence of reduced survival [105]. An additional heterozygous loss of SMARCA4 in *Blbp-cre::Ctnnb1(ex3)^{fl/wt}::Smarca4^{fl/wt}* mice did not influence observed phenotypes or survival (median survival 2.5 days). In contrast to that, mice bearing a homozygous loss of SMARCA4 alone (*Blbp-cre::Smarca4^{fl/fl}*) died even earlier. Only one mouse survived until P11, at which point it had to be sacrificed due to severe ataxia. Lastly, combined mutation of β -catenin and homozygous SMARCA4 loss in *Blbp-cre::Ctnnb1(ex3)^{fl/wt}::Smarca4^{fl/fl}* mice resulted in the highest lethality. All mice born with this genotype were either found dead at birth or died on the same day (n=8). *Blbp-cre::Smarca4^{fl/wt}* mice did not show any phenotype and were treated as equivalent to controls in further investigations.

Blbp-cre::Ctnnb1(ex3)^{fl/wt} and *Blbp-cre::Ctnnb1(ex3)^{fl/wt}::Smarca4^{fl/fl}* mice that survived up until P15 showed a macroscopic hydrocephalus and were smaller compared to littermates (Fig. 14B). Their weight was significantly reduced in comparison to littermates within their second week of life (Fig. 14C). Histologically, both genotypes showed a severe hydrocephalus and hypoplastic cerebella with significantly reduced size in comparison to controls (Fig. 14D-G). The cerebellum of mutants showed severe architectural abnormalities with disturbed layering and cell accumulations in both cerebellum and dorsal brain stem (Fig. 14H-P). IHC stainings revealed nuclear accumulation of β -catenin in cellular accumulations of both regions and both mutants, while partial SMARCA4 loss was only visible in cell accumulations of *Blbp-cre::Ctnnb1(ex3)^{fl/wt}::Smarca4^{fl/fl}* mice (Fig. 14Q-B'). Altogether, proliferation as indicated by Ki67 stainings was very low in all cell accumulations detected, pointing towards a neurodevelopmental phenotype rather than tumorous lesions (Fig. 14C'-H').

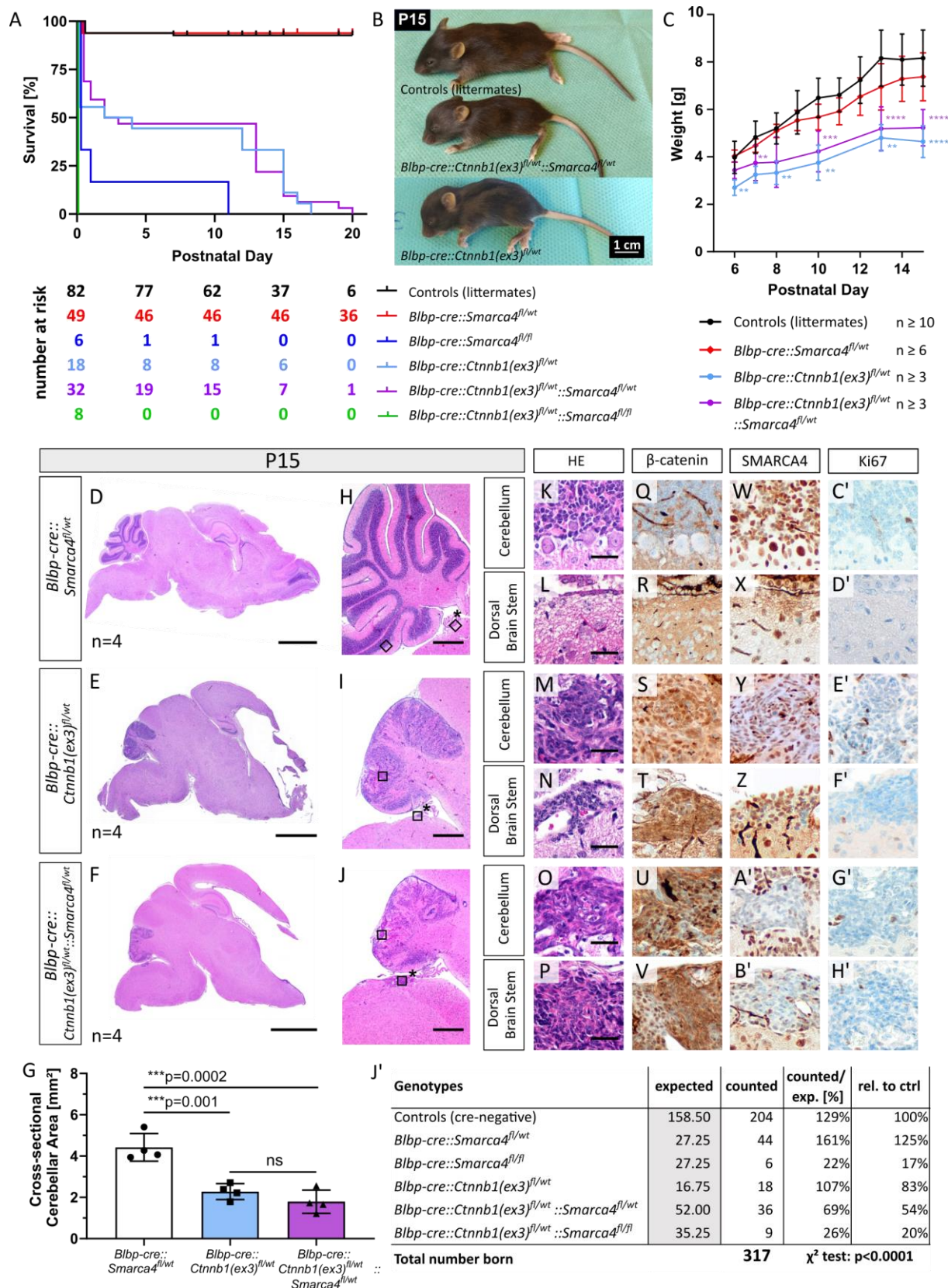


Figure 14. (Figure legend on following page)

Figure 14. Early lethality and severe developmental phenotypes of *Blbp-cre::Ctnnb1(ex3)^{fl/wt}* mice. (A) Survival curves reveal short lifespan of *Blbp-cre::Smarca4^{fl/fl}*, *Blbp-cre::Ctnnb1(ex3)^{fl/wt}*, and *Blbp-cre::Ctnnb1(ex3)^{fl/wt}::Smarca4^{fl/wt}* mice, while *Blbp-cre::Smarca4^{fl/wt}* mice behave similar to controls. All mice of the genotype *Blbp-cre::Ctnnb1(ex3)^{fl/wt}::Smarca4^{fl/fl}* died at birth or within the first day of life. The table beneath the graph depicts numbers at risks for the respective genotypes and time points. (B) Macroscopic hydrocephalus and reduced size of mutant mice at sacrifice (P15). (C) Significantly reduced weight of mutant mice compared to controls within the second week of life (Tukey's multiple comparisons test was applied; ** $p < 0.01$, *** $p < 0.001$, **** $p < 0.0001$). (D-F) HE staining of sagittal brain sections reveals hydrocephalus and hypoplastic cerebella in *Blbp-cre::Ctnnb1(ex3)^{fl/wt}* and *Blbp-cre::Ctnnb1(ex3)^{fl/wt}::Smarca4^{fl/wt}* mice compared to *Blbp-cre::Smarca4^{fl/wt}* controls. (G) Cross-sectional cerebellar area is significantly reduced in mutants as measured in HE sagittal sections of four mice each (Tukey's multiple comparisons test was applied). (H-J) HE stainings show defective lamination and foliation in cerebella of both *Blbp-cre::Ctnnb1(ex3)^{fl/wt}* and *Blbp-cre::Ctnnb1(ex3)^{fl/wt}::Smarca4^{fl/wt}* mice. (K-H') HE and IHC of aberrant cell accumulations in the cerebellum and dorsal brain stem of mutants (corresponding to black rectangles in H-J with and without asterisks, respectively). Cell accumulations show nuclear accumulation of β -catenin (S, T, U, V), partial loss of SMARCA4 only in *Blbp-cre::Ctnnb1(ex3)^{fl/wt}::Smarca4^{fl/wt}* mutants (A', B'), and weak proliferation in both mutants and both locations (E'-H'). (J') Analysis of counted versus expected genotypes according to Mendelian ratio suggests prenatal lethality, especially for *Blbp-cre::Smarca4^{fl/fl}* and *Blbp-cre::Ctnnb1(ex3)^{fl/wt}::Smarca4^{fl/fl}* mutants. A chi-square test was applied. Scale bars in D,E,F correspond to 2 mm, in H,I,J to 500 μ m, and in K-P to 50 μ m (also applicable to panels Q-H').

Further stainings were performed to gain insights into the origin and characteristics of cell accumulations (Suppl. Fig. 2). Both accumulations in brain stem and cerebellum showed similar characteristics by staining positive for cre, Nestin, and SOX2 with sparse expression of GFAP and OLIG2 and no signal for Parvalbumin, PAX6, S100, NeuN, and calbindin. Altogether, this pattern suggested an origin in undifferentiated neural progenitor cells.

To find an explanation for the unexpected severity of phenotypes in our breeding, we generated fate mapping mice to track expression of BLBP in our strain. RFP staining in *Blbp-cre::lsIR26tdRFP^{fl/wt}* mice at embryonic day 14.5 (E14.5) revealed a much broader expression in our mice than previously described. Recombination was detected throughout the whole developing cerebellum, the brain stem, and parts of the midbrain and rostral cerebral cortex (Suppl. Fig. 3). In contrast, Gibson *et al.* showed recombination in the hindbrain at the same timepoint mostly restricted to the germinal zones (lower rhombic lip [LRL], upper rhombic lip [URL], ventricular zone [VZ], external granular layer [EGL]) [105].

An analysis of mutants at birth (P0) revealed that the phenotype of *Blbp-cre::Ctnnb1(ex3)^{fl/wt}* mice with severe hydrocephalus and dorsal brain stem lesions was already evident at this point in time (Suppl. Fig. 4A -T). Additionally, mice displayed lesions in the cerebral cortex at this stage. At the same time, *Blbp-cre::Smarca4^{fl/fl}* mice developed hydrocephalus and a hypoplastic cerebellum while showing a loss of SMARCA4 but no aberrant cell accumulations in neither brain stem nor cerebral cortex (Suppl. Fig. 4U-D'). *Blbp-cre::Ctnnb1(ex3)^{fl/wt}::Smarca4^{fl/fl}* mice were mostly found dead with hydrocephalus and severely hypoplastic cerebellum and displayed no sign of tumor development (Suppl. Fig. 4E'-N'). However, counted vs expected genotypes in our breeding revealed that both mutants *Blbp-cre::Smarca4^{fl/fl}* and *Blbp-cre::Ctnnb1(ex3)^{fl/wt}::Smarca4^{fl/fl}* were

born at a highly reduced frequency relative to expected Mendelian ratio, with 22% and 26%, respectively (Fig. 14J'). These values suggested prenatal lethality of mutants and prompted us to additionally analyze mutant mice at embryonic stage.

3.3.2 *Blbp-cre::Ctnnb1(ex3)^{fl/wt}::Smarca4^{fl/fl}* mice develop proliferative cerebellar lesions at embryonic age

Blbp-cre::Ctnnb1(ex3)^{fl/wt}::Smarca4^{fl/fl} mice (further referred to as 'mutants') displayed big cerebellar lesions in the developing cerebellum at E14.5, which were not visible in cre-negative controls (Fig. 15A-D). Lesions were mainly located within the cerebellar hemispheres and were not detected in the developing vermis (Fig. 15E-H). They were cell dense, interspersed with blood vessels and showed nuclear accumulation of β -catenin and a loss of SMARCA4 in all cells (Fig. 15I-N). Furthermore, they stained positive for expression of cre and SOX2, the expression of which is usually restricted to the ventricular zone (Fig. 15O-S). Proliferation as measured by Ki67-positive area was significantly increased in mutants compared to the corresponding region in controls (36.2% and 4.2%, respectively) (Fig. 15T-U). Additionally, lesions often displayed rosette-like features, a characteristic attributed to NSCs, and a phenomena also occurring in some MB cases [85, 214] (Fig. 15V-W).

Double IF staining of SMARCA4 and phospho-histone H3 (pHH3) confirmed SMARCA4 knock-down in around 90% of cells within the lesions and revealed a significant increase of mitotic cells compared to control cerebellum (Suppl. Fig. 5A-H). Furthermore, we stained for GLUT-1 in blood vessels, which is needed to facilitate glucose transport across the blood-brain barrier [215, 216]. Phoenix *et al.* have shown the absence of GLUT-1 in human WNT MB and brain stem lesions in *Blbp-cre::Ctnnb1(ex3)^{fl/wt}::Trp53^{fl/fl}* mice that both display a defective blood-brain barrier [217]. However, blood vessels in cerebellar lesions of our mutants stained positive for GLUT-1, suggesting a maintained blood-brain barrier in our model (Suppl. Fig. 5I-L).

Next, we had a closer look at cell populations within the cerebellar ventricular zone (VZ) where the lesions seemed to originate from. During embryonic hindbrain development, the cerebellar VZ gives rise to PAX2-positive inhibitory interneurons, which migrate radially inside the cerebellum from E12.5 on [218]. While migrating PAX2-positive precursors were visible in controls at E14.5, they could not be detected throughout the whole mutant cerebellum, suggesting disturbed differentiation towards this lineage in mutants (Fig. 15X-A').

With the analysis of multiple litters at E14.5, we soon gathered evidence that cerebellar lesions were only found in *Blbp-cre::Ctnnb1(ex3)^{fl/wt}::Smarca4^{fl/fl}* mutants derived from breeding with cre-positive mothers (*Blbp-cre::Smarca4^{fl/wt}* females crossed with *Ctnnb1(ex3)^{fl/fl}::Smarca4^{fl/fl}* males). In contrary, 0 of 5 mutants derived from cre-positive fathers (*Blbp-cre::Smarca4^{fl/wt}* males

crossed with *Ctnnb1(ex3)^{fl/fl}::Smarca4^{fl/fl}* females) developed cerebellar lesions (3 litters analyzed). Consequently, we investigated *Smarca4* recombination in embryonic tail biopsies of embryos to test for germline recombination since BLBP is not physiologically expressed in this region. PCR analysis revealed a recombined *Smarca4* allele in the tails of all offspring derived from cre-positive mothers (Fig. 15B'). The fact that not only mutant but also cre-negative embryos were affected by *Smarca4* recombination in the tail suggested that *Smarca4* recombination had already happened in the oocytes of mothers and was not due to expression of cre in the embryo but in the ovaries of mothers [156]. In contrast, none of the embryos derived from cre-positive fathers showed *Smarca4* recombination in tail biopsies. We concluded that the preceding loss of one *Smarca4* allele before cre-induced loss of the second *Smarca4* allele and mutation of *Ctnnb1* greatly influences observed phenotypes in mutants. Therefore, we decided to perform all following analysis with offspring of cre-positive mothers only.

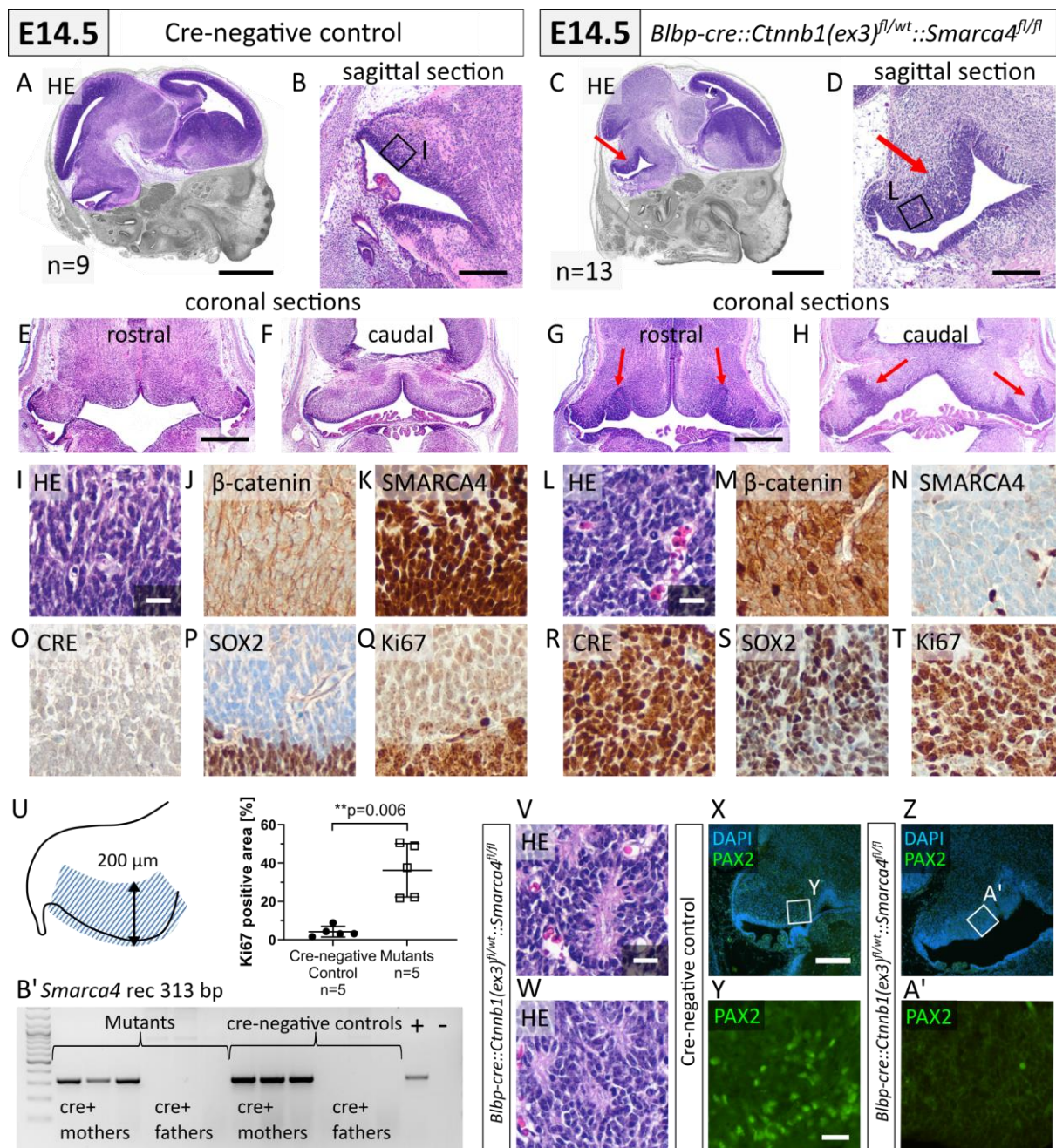


Figure 15. Combined activation of WNT signaling and loss of SMARCA4 induces proliferative lesions at embryonic age in *Blbp-cre::Ctnnb1(ex3)^{fl/wt}::Smarca4^{fl/fl}* mutant mice. (A-D) HE stainings show large lesion in the ventricular zone of the developing cerebellum at E14.5 in mutants (red arrow in C+D) compared to cre-negative littermates (A+B). (E-H) HE staining of coronal sections reveals the presence of lesions in the rostral as well as caudal section of the cerebellum within both hemispheres (red arrows) but excluding the midline. (I-T) High-power images of lesions compared to control cerebella display high cell density interspersed with blood vessels (L), nuclear accumulation of beta-catenin (M), loss of SMARCA4 (N), and positivity for cre (R) and SOX2 (S). Ki67 staining indicates high proliferation within the lesions (T) with a significantly increased area staining positive for Ki67 in mutants (U, area measured shown on the left, Welch's t-test was applied). (V+W) Rosette-like structures detected in HE within lesions of *Blbp-cre::Ctnnb1(ex3)^{fl/wt}::Smarca4^{fl/fl}* mice. (X+Y) PAX2 staining shows the migration of interneuron progenitors from the ventricular zone inwards in control animals. (Z-A') PAX2-positive interneuron progenitors are not detected in the ventricular zone of mutant animals. (B') PCR for recombinant *Smarca4* in tail biopsies of mutant and cre-negative embryos reveals the presence of a recombinant allele in the germline of all offspring of cre-positive mothers. Scale bars in A+C correspond to 1 mm, in B+D to 250 μ m, in E+G to 500 μ m (also applicable to F+H), in I+L+V to 25 μ m (applicable to I-T, W), in X to 200 μ m (applicable to Z), and in Y to 25 μ m (applicable to A').

Additionally to *Blbp-cre::Ctnnb1(ex3)^{fl/wt}::Smarca4^{fl/fl}* mutants described above, we also analyzed other mutant genotypes at E14.5. Although a loss of SMARCA4 was visible in the cerebella of *Blbp-cre::Smarca4^{fl/fl}* mice, they did not display any proliferative cerebellar lesions (Suppl. Fig. 6A-P). Furthermore, *Blbp-cre::Ctnnb1(ex3)^{fl/wt}* and *Blbp-cre::Ctnnb1(ex3)^{fl/wt}::Smarca4^{fl/wt}* mice had not developed any phenotype yet (Suppl. Fig. 6B-R).

3.3.3 Cerebellar lesions develop from E13.5 to E16.5

To find out more about the origin and developmental window of the embryonic cerebellar lesions, we analyzed *Blbp-cre::Ctnnb1(ex3)^{fl/wt}::Smarca4^{fl/fl}* mutants at different embryonic time points (E12.5, E13.5, E14.5, E16.5, E18.5). Cerebellar lesions were detected earliest at E13.5 and latest at E16.5 (Fig. 16A-D). An analysis of mutants at E18.5 was not possible as several litters did not yield any mice bearing the desired genotype (Fig. 16E). Although loss of SMARCA4 was already visible in the cerebella of mutant mice at E12.5, accumulation of β -catenin could not be detected yet (Fig. 16F,G). However, only one day later at E13.5, lesions with a complete loss of SMARCA4 and nuclear accumulation of β -catenin were evident (Fig. 16H,I). These lesions grew in size up until E16.5, at which point they spanned great parts of the developing cerebellum (Fig. 16J-M).

None of the few mutants born and analyzed at birth (P0) showed any apparent lesions although a complete loss of SMARCA4 in the cerebellum was visible (Suppl. Fig. 7A-C). To find an explanation for this discrepancy, we investigated recombination of *Smarca4* in the germline as well as local recombination of *Smarca4* and *Ctnnb1* in FFPE brain sections of the mutants histologically analyzed from E12.5 to P0. Germline recombination of *Smarca4* was detected in all mutants including mice without lesions at P0 (Suppl. Fig. 7D). Furthermore, recombination of *Smarca4* in the brains at P0 was confirmed using DNA extracted from FFPE sections (Suppl. Fig. 7E). However, recombination of *Ctnnb1* was not detected in P0 brains compared to mutants at E14.5 or E16.5, indicating incomplete recombination as a possible cause for the missing lesions and prolonged survival of a few mutants (Suppl. Fig. 7F).

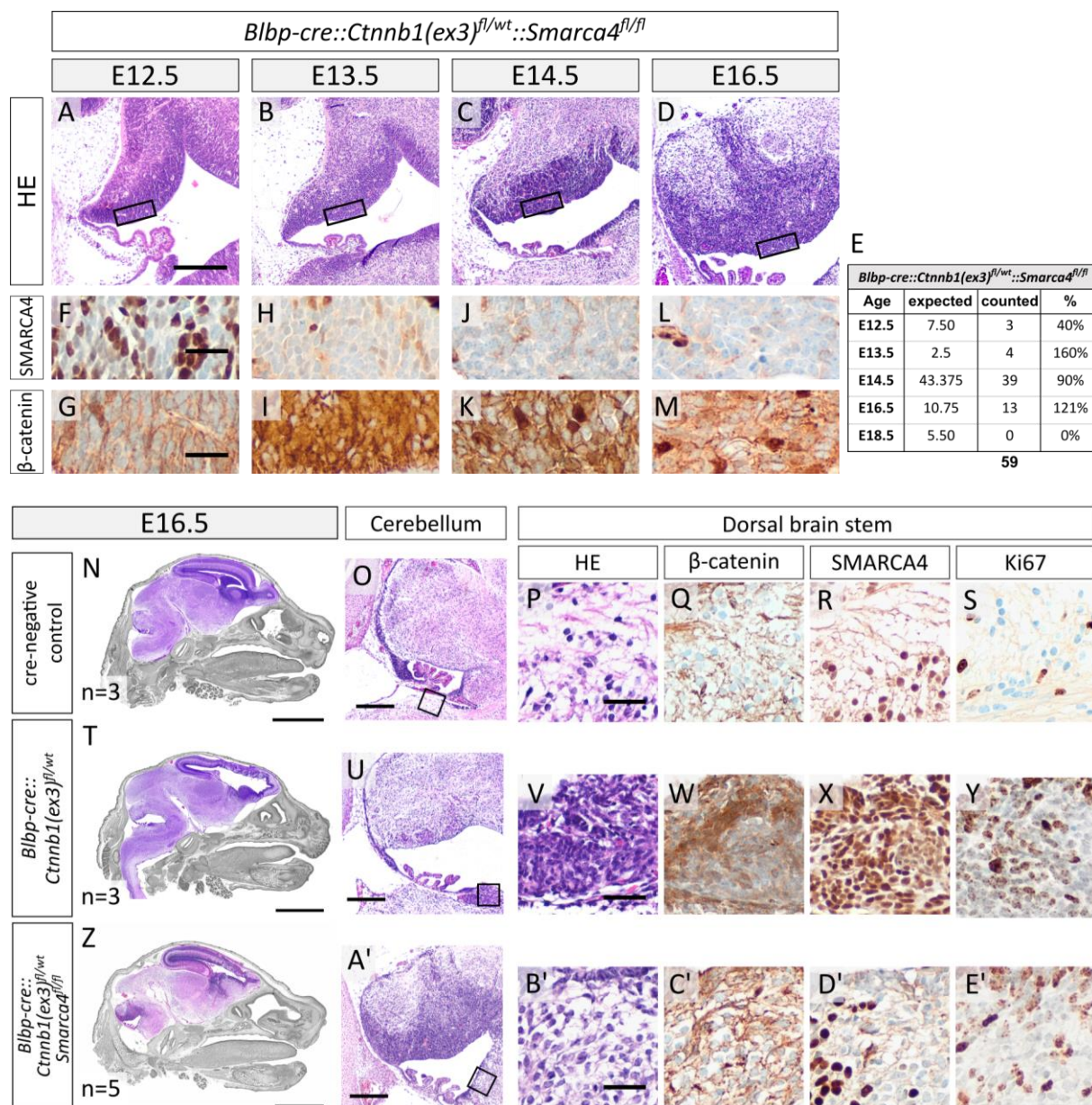


Figure 16. Cerebellar lesions develop from E13.5 to E16.5. (A-D) HE stainings of *Blbp-cre::Ctnnb1(ex3)^{fl/wt}::Smarca4^{fl/fl}* brains show cerebellar development from E12.5 to E16.5 with lesions visible from E13.5 to E16.5. (E) Expected vs counted genotypes in litters of cre-positive mothers at different embryonic stages. (F-M) SMARCA4 and β -catenin stainings of ventricular zone (black rectangle in A-D) reveals partial loss of SMARCA4 at E12.5 and complete SMARCA4 loss from E13.5 on. Nuclear accumulation of β -catenin is visible in lesions from E13.5 to E16.5. (N-S) HE stainings of cre-negative controls at E16.5 show normally developing cerebellum with low cell density in HE (N-P), absence of β -catenin accumulation (Q), positivity for SMARCA4 (R) and low proliferation (S). Meanwhile, *Blbp-cre::Ctnnb1(ex3)^{fl/wt}* mice display aberrant cell accumulations in the dorsal brain stem with high cell density (T-V), nuclear accumulation of β -catenin (W), and SMARCA4-positive cells with increased proliferation (X,Y). *Blbp-cre::Ctnnb1(ex3)^{fl/wt}::Smarca4^{fl/fl}* mutants display beforementioned cerebellar lesions (Z,A') but do not develop any cell accumulations in the brain stem (B'-E'). Loss of SMARCA4 is apparent in the affected region (D'). Scale bar in A corresponds to 250 μ m (also applicable to B-D), to 25 μ m in F+G (applicable to F-M), to 2 mm in N, T, and Z, to 250 μ m in O, U, A', and to 20 μ m in P, V, B' (also applicable to remaining panels). Only offspring of cre-positive mothers was included in analysis.

3.3.4 Brain stem cell accumulations do not develop after SMARCA4 loss

A detailed comparison of brains at E16.5 from *Blbp-cre::Cttnb1(ex3)^{fl/wt}::Smarca4^{fl/fl}*, *Blbp-cre::Cttnb1(ex3)^{fl/wt}* mice, and cre-negative controls revealed that the cell accumulations in the dorsal brain stem previously detected in *Blbp-cre::Cttnb1(ex3)^{fl/wt}* mice at P15 and P0 were already visible at this time point (Fig. 16N-Y). In contrast to that, none of the *Blbp-cre::Cttnb1(ex3)^{fl/wt}::Smarca4^{fl/fl}* mutants with cerebellar lesions developed any aberrant accumulations in the brain stem but only showed a loss of SMARCA4 in this region (Fig. 17Z-E'). Brain stem lesions were already described missing in *Blbp-cre::Cttnb1(ex3)^{fl/wt}::Smarca4^{fl/fl}* mutants at P0 (see Suppl. Fig. 4). However, in this case, the presence of cerebellar lesions at E16.5 proved successful *Cttnb1* recombination in mutants. Consequently, missing cell accumulations cannot be explained by insufficient recombination but are most probably attributed to the SMARCA4 loss in this region.

3.3.5 Methylation analysis of cerebellar lesions

To characterize cerebellar lesions of *Blbp-cre::Cttnb1(ex3)^{fl/wt}::Smarca4^{fl/fl}* mutants on a molecular level, we isolated DNA from FFPE punches of control and mutant cerebella at E16.5. Subsequent DNA methylation analysis was performed using the *Mouse Methylation BeadChip*. Principal Component Analysis (PCA) based on the 10,000 most differentially methylated CpG sites showed a clear separation of control and mutant samples (Fig. 17A). In a next step, gene set enrichment analysis was performed and revealed many significantly differentially methylated gene sets in mutant vs control samples. The top 25 gene sets according to adjusted p-values included several gene ontology (GO) terms associated with neural development, GTPase activity, cytoskeleton organization, and transmembrane transport (Fig. 17B). Moreover, β -catenin binding was included in the Top 25, providing further evidence for aberrant WNT signaling in our mutants. For a more general overview, all significantly differentially methylated GO terms designated as 'biological processes' were visualized after removing redundant terms with REVIGO [197]. Similar to trends observed in the Top 25, processes involved in nervous system development, signal transduction, cytoskeleton organization, and transmembrane transport were identified with a high degree of connectivity (Fig. 17C). Additionally, GO terms associated with protein phosphorylation, cell migration, and proliferation and apoptosis were included.

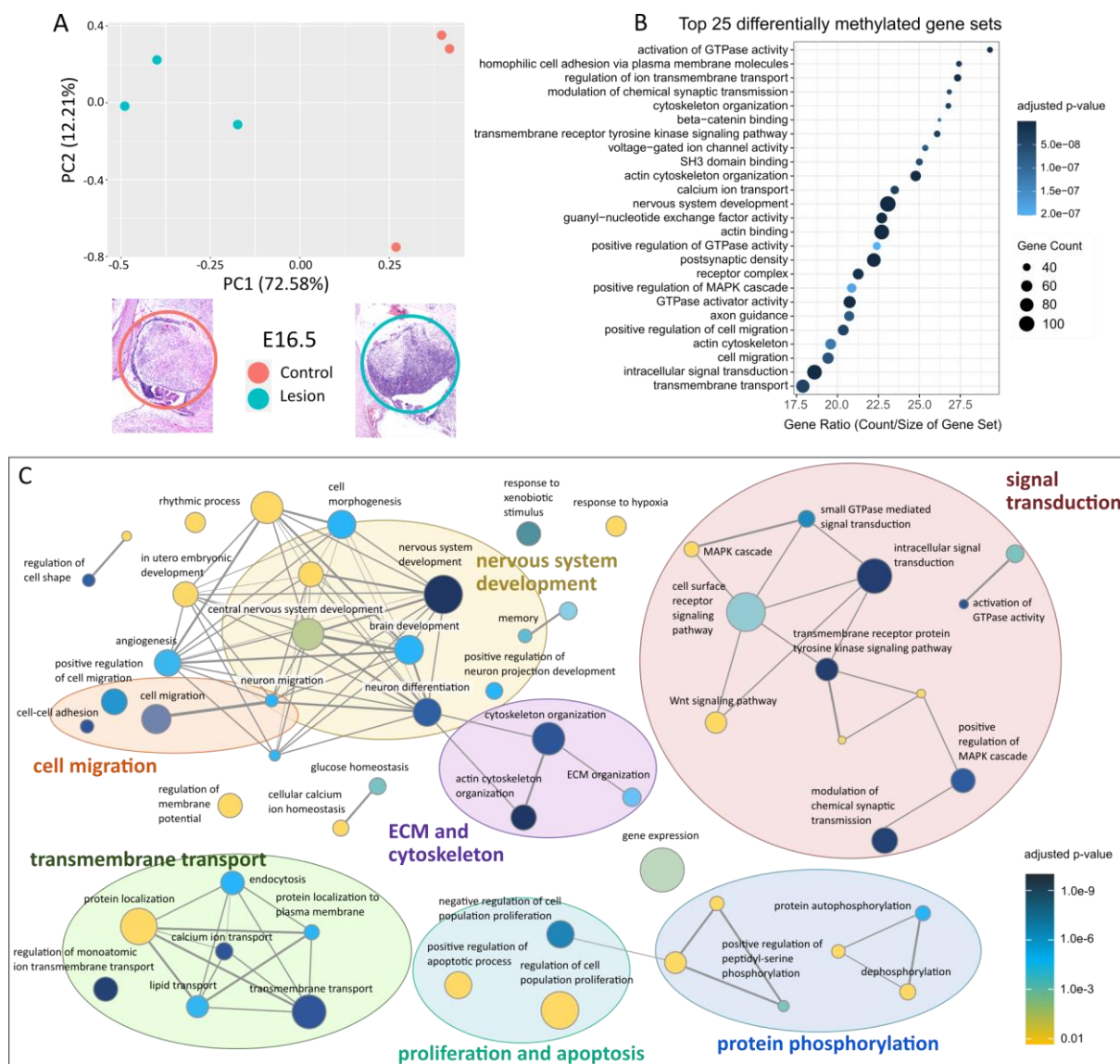


Figure 17. DNA methylation analysis of cerebellar lesions at E16.5. (A) E16.5 control cerebella and lesions of *Blbp-cre::Cttnb1(ex3)^{fl/wt::Smarca4^{fl/fl}}* mutants can be clearly separated according to 10,000 most differentially methylated CpG sites in PCA analysis. (B) Top 25 differentially methylated gene sets between controls and lesions according to adjusted p-value (methylRRA was applied [196]) sorted by gene ratio (count/size of gene sets). (C) All significantly differentially methylated gene sets of the category ‘biological process’ found with methylRRA were summarized by REVIGO to remove redundant terms [197]. Here, 3% of the strongest GO terms pairwise similarities are designated as edges in the graph. The size of bubbles corresponds to the size of gene sets. Most identified terms were related to nervous system development, ECM and cytoskeleton, transmembrane transport, proliferation and apoptosis, protein phosphorylation, or signal transduction.

To compare the methylation profile of murine cerebellar lesions to human brain tumors, we also integrated our data with a brain tumor dataset comprising in-house analyzed samples and previously published cohorts (Capper *et al.* [101], Sharma *et al.* [123]). Out of the 15,000 most differentially methylated CpG sites within the human cohort, the 640 CpG sites orthologous in humans and mice were chosen for further analysis. Differential methylation of these 640 CpG sites efficiently separated tumor subtypes in both UMAP and Euclidian clustering (Suppl. Fig. 8). However,

clustering of our lesions yielded non-conclusive results with proximity to ATRTs in UMAP and to spinal paraganglioma in Euclidian clustering.

3.3.6 Single-cell gene expression analysis of cerebellar lesions

To further characterize specific mutant cell populations in the cerebellum of *Blbp-cre::Ctnnb1(ex3)^{fl/wt}::Smarca4^{fl/ft}* mice, we performed single-cell gene expression analysis of cerebellar cells isolated at E16.5. In UMAP clustering, mutant cerebella displayed distinct clusters that were not present in cre-negative control cerebella (Fig. 18A). According to predicted cell classes, mutant clusters mainly consisted of radial glia, neuroblasts, and neurons (Fig. 18B). Especially radial glia were overrepresented in the mutant cerebellum with a count of 2282 cells (16.6% of total cells) compared to 886 cells (6.4% of total cells) in the control cerebellum (Suppl. Tables 3+4). A more detailed cell class prediction according to subclasses defined within the dataset of la Manno *et al.* 2021 [204] predominantly identified hindbrain cell populations within the mutant clusters, interspersed with midbrain and mixed region populations (Suppl. Fig. 9A-B). However, scores for the classifications were lower compared to similar populations in the control cerebellum (Suppl. Fig. 10). Moreover, cell populations previously identified as radial glia in mutants could not be assigned to a certain subclass and were designated as 'undefined', further emphasizing the anomaly of mutant cerebellar cells (Suppl. Fig. 9A-B). Overall, the number of glutamatergic cerebellar cells in mutants was highly reduced compared to controls.

Cell cycle analysis identified both clusters 2 and 9 as mitotically active, with all cells assigned to the G2M or S phase (Fig. 18C). While cluster 2 mainly consists of cells derived from control cerebellum, cluster 9 is a mutant cluster that could represent a potentially tumorigenic aberrant cell population within the lesions. Next, we compared expression of *Sox2* and WNT signaling target genes between clusters. SOX2, which stained positive in previous histological analyses of cerebellar lesions, also showed increased gene expression in mutant clusters 9 and 17, and to a smaller extent in cluster 0 (Fig. 18D). Additionally, all three clusters displayed high levels of *Dkk3*, *Wnt5a*, *Dkk2*, *Lef1*, *Axin2*, *Dkk1*, and *Wif1*, which have all been associated with activated WNT signaling before [105, 219, 220].

Next, we estimated the age of cells according to the reference dataset of la Manno *et al.* 2021, including expression data from E10.0 to E16.5. While most cells within the control clusters were assigned to E15.0-E16.5, mutant clusters also included a considerable number of cells with predicted ages between E11.0-E14.0, further emphasizing the undifferentiated nature of mutant cells (Fig. 18E). Cluster 6 displayed the highest deviation from expected age with a mean predicted age of 14.38 embryonic days (Suppl. Table 5). The mitotically active mutant cluster 9 showed a mean

predicted age of 15.13 embryonic days compared to 15.99 embryonic days in the mitotically active control cluster 2.

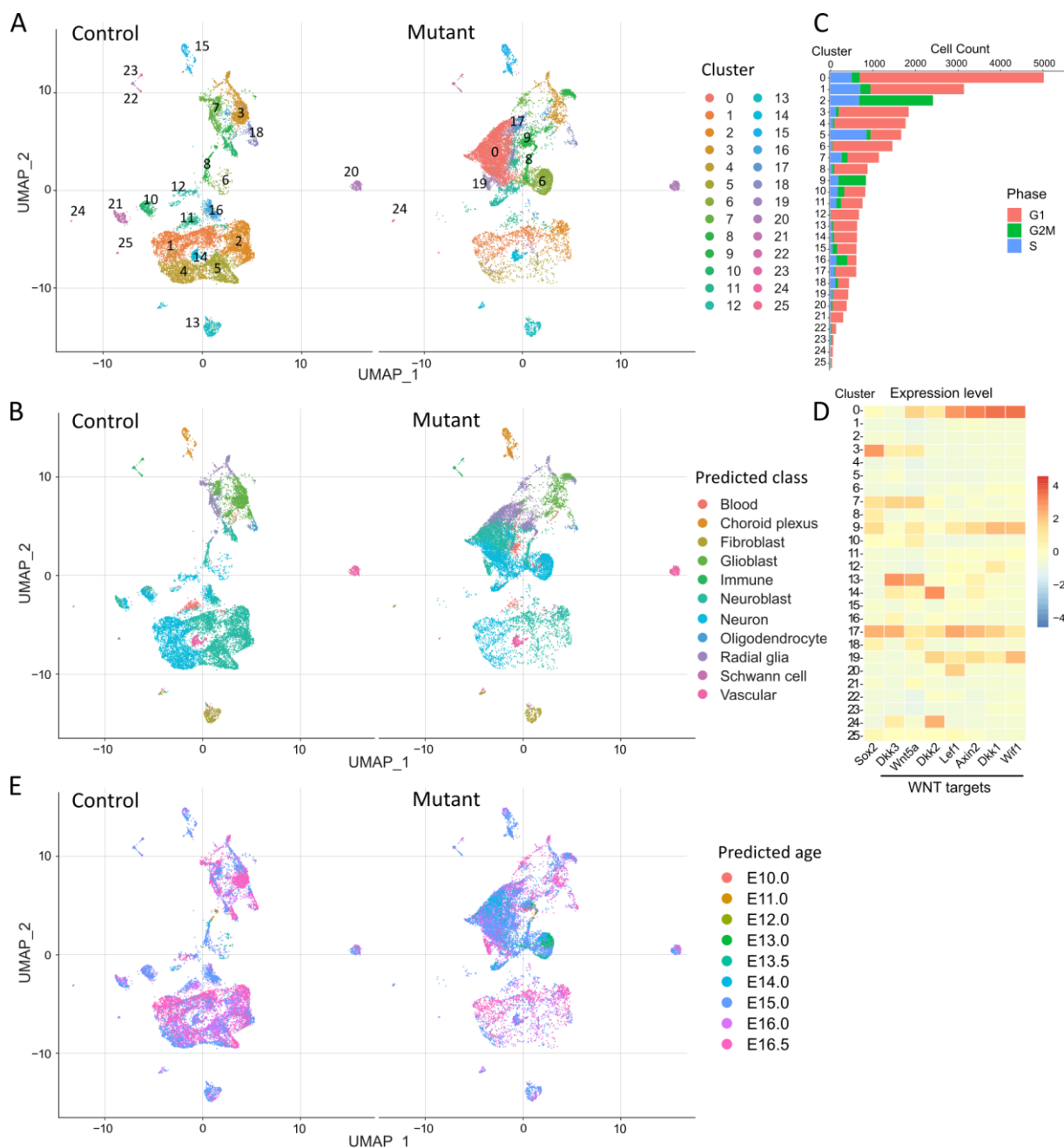


Figure 18. Single-cell RNA sequencing analysis at E16.5 reveals distinct mutant clusters of undifferentiated nature. (A) UMAP clustering of single cells derived from control and mutant (*Blbp-cre::Cttnb1(ex3)^{fl/wt}::Smarca4^{fl/fl}*) cerebella at E16.5 according to differential gene expression. In total, 25 clusters were identified, of which clusters 0, 6, 8, 9, 17, 19, and 24 mainly consist of mutant cells. (B) Predicted cell classes as described by la Manno *et al.*, 2021 [204] show an increased number of radial glia cells in mutants. (C) Cell cycle analysis identified high mitotic activity in both cluster 2 and mutant cluster 9. (D) The expression level of SOX2 and WNT target genes is increased in mutant clusters 0, 9, and 17. (E) Age predictions according to the la Manno *et al.* 2021 reference dataset including expression data from E10.0 to E16.5 suggests a more undifferentiated nature of cells within mutant clusters.

3.3.7 Analysis of *in vitro* proliferation and tumorigenic potential of cerebellar lesions

To evaluate the tumorigenic potential of cerebellar lesions detected in *Blbp-cre::Ctnnb1(ex3)^{fl/wt}::Smarca4^{fl/fl}* mutants, hindbrain progenitor cells (HPCs) were isolated from controls and mutants at E14.5. Cumulative population doublings during cell culture as neurospheres for four weeks did not show any significant differences between proliferation of cre-negative controls, mutants (*Blbp-cre::Ctnnb1(ex3)^{fl/wt}::Smarca4^{fl/fl}*), and heterozygous mutants (*Blbp-cre::Ctnnb1(ex3)^{fl/wt}::Smarca4^{fl/wt}*) (Fig. 19A). Morphologically, neurospheres of mutants did not differ from controls (Fig. 19B-C). Moreover, mutants maintained dependency on EGF and FGF in adherent cell cultures on PLO coated wells (Fig. 19D-G). IHC at early time points in culture (d9) showed a loss of SMARCA4 in the majority of cells derived from mutants (Fig. 19H). However, this loss of SMARCA4 was not detected at later time points in culture, suggesting a selection for SMARCA4-positive cells *in vitro* over time (Fig. 19I). According to double IF staining of SMARCA4 and pHH3 at d9, only SMARCA4-positive cells were mitotically active in mutants (Fig. 19J). Additionally, an evaluation of recombined β -catenin in DNA isolated at different passages of mutant HPCs showed a loss of the recombined allele from passage 2 (P2) on (Fig. 19K). Altogether, data pointed towards a loss of recombined cells after HPC culture of mutants *in vitro*. We hypothesized that the *in vitro* environment did not provide the required scaffold and paracrine signals from surrounding cells needed for survival and extensive proliferation of recombinant cells. Therefore, we transplanted E14.5 HPCs of controls, mutants, and heterozygous mutants (n=10 each) into the cerebella of immunodeficient mice to evaluate tumorigenic potential *in vivo*. To avoid selection of recombined cells, transplantation was performed directly after papain digestion and singularization of hindbrain tissue (Fig. 19L). However, no tumor development was detected in any of the groups six months after transplantation.

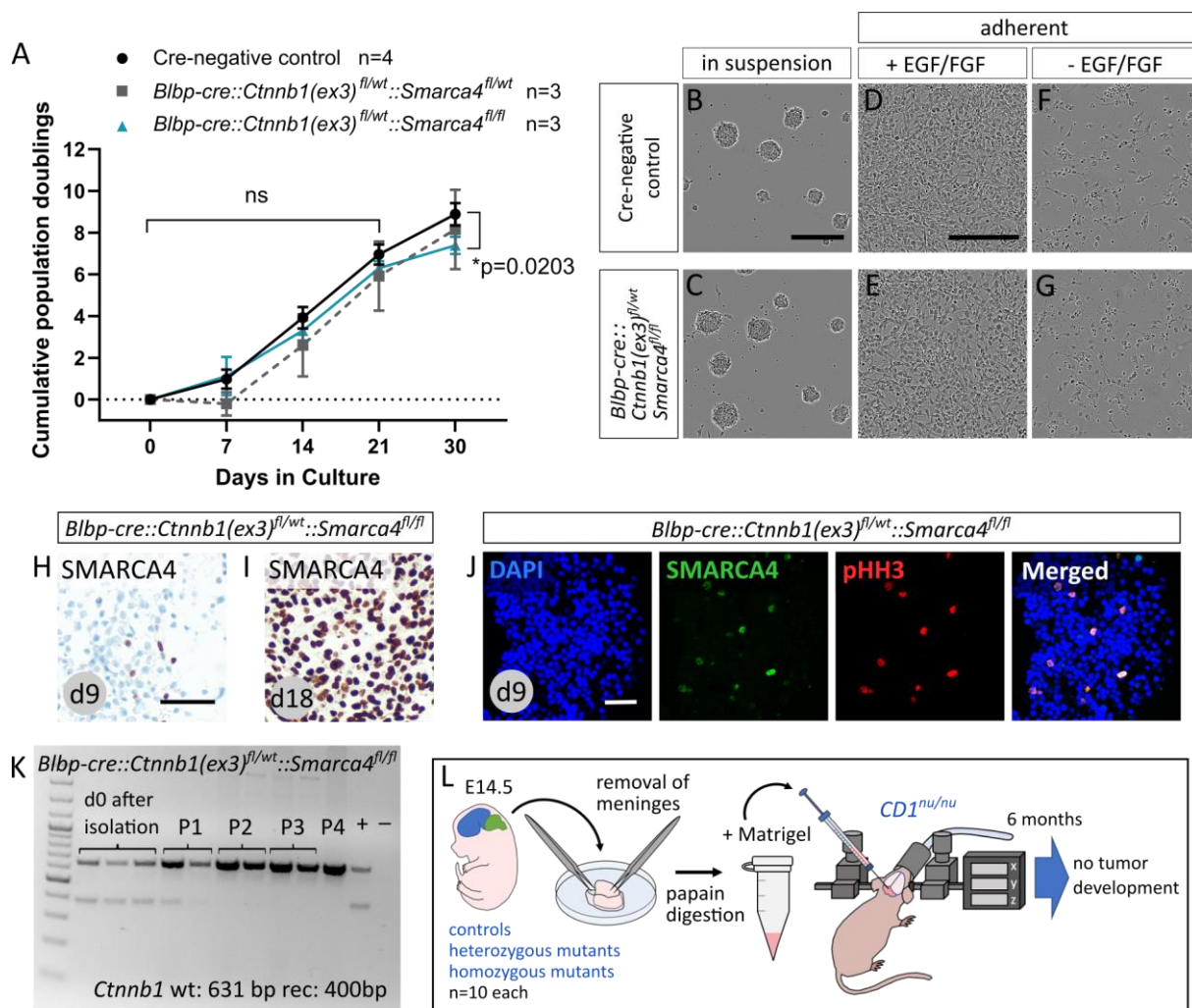


Figure 19. Hindbrain progenitor cells (HPCs) of mutant mice do not show increased proliferation *in vitro* or tumorigenic potential after transplantation. (A) HPCs isolated at E14.5 from heterozygous mutants (*Blbp-cre::Ctnnb1(ex3)^{fl/wt}::Smarca4^{fl/wt}*) and homozygous mutants (*Blbp-cre::Ctnnb1(ex3)^{fl/wt}::Smarca4^{fl/fl}*) do not display significant increase in cumulative population doublings during a culture period of 30 days with weekly passaging. At day 30, population doublings are even slightly reduced in homozygous mutants vs controls (mean=7.390 and 8.884, respectively). Tukey's multiple comparisons test was applied after two-way ANOVA. (B,C) Morphologically, neurospheres of controls and homozygous mutants do not differ from each other (both passage 2 (P2)). (D-G) Both mutant and control HPCs show adherent growth when seeded in PLO coated wells with a dependency on EGF/FGF for cell growth (both passage 3, four days after seeding). (H,I) SMARCA4 IHC on cell blocks of mutant HPCs at early passage (d9) shows a loss of SMARCA4 in the majority of cells, while at later passage (d18), almost all cells are SMARCA4 positive. (J) IF staining of mutants at early passage (d9) reveals that only SMARCA4-positive cells are mitotically active. (K) PCR for recombinant *Ctnnb1* with DNA isolated from mutant HPC pellets at isolation and at different passages (P1-P4). Recombinant *Ctnnb1* is present at d0 and at P1 but in no sample of passages 2-4, where only wildtype *Ctnnb1* can be detected. (L) Transplantation of E14.5 hindbrains (n=10 of each control, heterozygous mutants, and homozygous mutants) into immunodeficient *CD1^{nu/nu}* mice did not result in tumor development. Scale bar in B corresponds to 200 μ m (applicable to C), in D to 200 μ m (applicable to E-G), in H to 50 μ m (applicable to I) and in J to 50 μ m.

4 DISCUSSION

Within this study, we demonstrated important functions of SMARCA4 in both brain development and tumorigenesis. *In vitro*, the introduction of mutant SMARCA4 variants in cell lines and primary neural cells did not result in altered cell viability. However, orthotopic transplantation of SMARCA4-deficient and MYC overexpressing cells drove brain tumor formation *in vivo* with high resemblance to Group 3 MB. Moreover, a loss of SMARCA4 and activated WNT signaling caused proliferative lesions in murine embryonic hindbrains. Altogether, these findings provide valuable insights into the involvement of SMARCA4 in tumor development. However, limitations of our experiments such as the cellular origin of tumors, early lethality of mutant mice, and methodological restrictions will have to be considered and will be thoroughly discussed in the following sections.

4.1 Characterization of SMARCA4 Variants *in vitro*

We successfully generated lentiviral constructs to overexpress SMARCA4 wildtype and SMARCA4 variants T910M and R1135W, which are commonly detected as heterozygous missense mutations in both WNT and Group 3 MB [70, 125]. As both mutational sites are located in the catalytic core of the protein, a consequent loss of function has been proposed [126, 221]. However, most SMARCA4 mutants are still able to bind to chromatin as demonstrated by Chromatin Immunoprecipitation (ChIP) Sequencing [44]. The SMARCA4 variant T910M even shows partial ATPase activity in *in vitro* ATPase assays, enabling opening of chromatin to a small degree at specific sites [182]. Therefore, it has been suggested that a homozygous loss of SMARCA4 might not accurately model the consequences of SMARCA4 missense mutations in patients [44]. This was our rationale for exploring the influence of overexpressed SMARCA4 variants on the proliferation of MB cell lines with a subsequent comparison to the effects of a full SMARCA4 knockdown.

The overexpression of all three SMARCA4 variants by lentiviral transduction did not influence viability of either human MB cell lines or murine primary cells. MB cell lines used in this study already carry MYC or OTX2 aberrations and chromosomal rearrangements driving their proliferation *in vitro* [222, 223]. In this case, the introduction of SMARCA4 variants might not activate additional pathways to promote cell growth. However, we did not analyze other mechanisms by which mutant SMARCA4 could contribute to tumorigenic potential of cells. Various genetic aberrations have been shown to promote migration or invasiveness of cancer cells by regulating actin cytoskeleton remodeling and cell adhesion without evidence for increased proliferation [224-226]. To assess influences on migration capacity of our cell lines, we could perform additional scratch assays and compare migration distances [227]. Moreover, transwell migration through a

membrane or a layer of extracellular matrix driven by chemo-attractants in the medium could provide insights into invasive potential of cells [228]. We only used non-WNT/non-SHH MB cell lines in our studies since WNT MB cell lines were not available. In general, WNT MB cell lines are strongly underrepresented with only two cell lines from one recurrent tumors and one primary tumor described so far [229, 230].

Since a knockdown of SMARCA4 with shRNA did not increase cell viability of MB cell lines either, we did not consider an insufficient dominant-negative effect of the mutant SMARCA4 variants. Additionally, our first experiment with SCCOHT-1 cells had given sufficient proof for a loss of function at least in our T910M variant, which even overruled the effects of SMARCA4 wildtype in a mixed transduction. We did not test for these characteristics with our variant SMARCA4 R1135W, which was generated later on. However, during our conduction of experiments, an extensive study on functional characterization of SMARCA4 variants, also including T910M and R1135W, was published by Fernando *et al.* [43]. They showed that both SMARCA4 variants are not able to rescue proliferation of SMARCA4-deficient NCI-H1944 and A549 cell lines after knockdown of the paralogue SMARCA2, whereas SMARCA4 wildtype restores cell viability. Moreover, they performed ChIP sequencing and Assay for Transposase-Accessible Chromatin (ATAC) sequencing to evaluate binding of SMARCA4 to chromatin sites and subsequent changes in accessibility. Their results showed that both variants are not only deficient in opening chromatin but even decrease chromatin accessibility, which is consistent with a potential dominant-negative function [43]. Altogether, these results confirmed the previously suspected loss of function character of both variants.

The missing effect of mutant SMARCA4 overexpression on proliferation of primary cells (murine GCPs) could be attributed to the fact that a second oncogenic hit was missing. In fact, previous studies have shown decreased ability of SMARCA4-deficient GCPs to respond to SHH in order to drive proliferation *in vitro* [231]. Differences between human and murine SMARCA4 are likely unproblematic in this setting since they share 99.3% sequence homology, including both amino acids affected in the variants [232, 233]. Similar to our developed MYC/SMARCA4 tumor model within this project, additional overexpression of a second oncogene such as MYC, OTX2, or GF11, which are frequently amplified in Group 3 MB, could contribute to increased cell proliferation [70, 106]. This would also allow us to compare the effects of a SMARCA4 knockdown to the overexpression of SMARCA4 variants that might more accurately model tumor biology in MB patients. However, dual transduction might pose an additional technical challenge, especially in sensitive GCPs. Alternatively, a transgenic knock-in mouse model for the conditional overexpression of SMARCA4 variants could be generated and explored in combination with other oncogenes using the cre-loxP system [148].

4.2 SMARCA4 in the Development of Group 3 Medulloblastoma

In order to generate a model for *SMARCA4* mutated Group 3 MB, we transplanted *SMARCA4*-deficient and *MYC* overexpressing GCPs in the cerebella of immunodeficient mice, which successfully induced tumor formation. The generation of this model was closely based on the MB model generated by Kawauchi *et al.* in 2012. Kawauchi used p53-deficient GCPs that were transduced with a *MYC* construct and transplanted into the cerebella of *CD1^{nu/nu}* mice [176]. However, *TP53* is not commonly mutated in primary Group 3 MB, which is why we exchanged this alteration with a *SMARCA4* deficiency in our study to model the patients' tumor biology more accurately.

4.2.1 Effects of *Smarca4* and *Myc* alterations *in vitro*

Our *in vitro* data indicated no increase in proliferation of GCPs after loss of *SMARCA4* alone. Proliferation was even significantly decreased at day 1 in culture. As SHH protein is added to the culture in order to drive proliferation, the previously described failure of *SMARCA4*-deficient GCPs to respond to SHH could explain this observation [231]. Reduced viability of *SMARCA4*-deficient cells *in vitro* has also been observed in neural progenitors derived from *Sox2-creER^{T2}::Smarca4^{fl/fl}::IslRFP^{fl/wt}* brains after embryonic tamoxifen injection [169]. Moreover, we have shown before that an induced loss of *SMARCA4* in *Math1-creER^{T2}::Smarca4^{fl/fl}* mice delays migration of GCPs to the IGL *in vivo* but does not affect the cerebellar phenotype seen in adult mice [168]. The same mice were observed for one year after induction without any sign of tumor development (data not shown). We conclude that a loss of *SMARCA4* on its own does not harbor tumorigenic potential in GCPs.

Next, the effects of *MYC* overexpression on GCP proliferation were investigated. Lentiviral transduction of GCPs with a murine *MYC* construct did not yield any significant changes in overall proliferation of the cultures. In contrast to that, Pei *et al.* have shown higher proliferation and increased ability to form neurospheres after transducing cerebellar stem cells with a *MYC* construct [206]. However, their study differs from our setup in terms of cellular origin (Prom⁺ Lin⁻ cerebellar stem cells instead of GCPs), culture conditions (spheres in stem cell medium with EGF/FGF), and choice of *MYC* construct (stabilized form *MYC^{T58A}*). Swartling *et al.* have shown before that overexpression of *MYCN* in NSCs does not result in tumor formation after transplantation, whereas overexpression of the stabilized variant *MYCN^{T58A}* does result in the development of diverse brain tumor types [234]. Consequently, the choice of wildtype *MYC* in our model might greatly influence outcome and might cause the necessity for a second alteration such as a *SMARCA4* deficiency in tumorigenesis. Moreover, the dual potential of *MYC* to drive both proliferation and apoptosis has

been demonstrated before in multiple studies (reviewed in [235]). Murphy *et al.* suggested distinct thresholds of MYC levels at which positive regulation of proliferation switches to the activation of apoptotic pathways as a guarding mechanism to prevent uncontrolled cell growth [236]. A balance between oncogenic and apoptotic mechanisms activated by high expression of MYC in our GCPs could have resulted in the missing effect on cell proliferation seen in our experiments.

Even in combination, a SMARCA4 loss and MYC overexpression did not result in increased overall proliferation of GCPs *in vitro*. However, our evaluation by IF did not enable us to specifically investigate proliferation of transduced SMARCA4-negative cells. We showed that this subpopulation only represents around 8% of cells, which is why the evaluation of overall proliferation does not accurately measure the effects induced by both alterations. The small but non-significant tendency towards increased proliferation we see in our BrdU staining could in fact point towards increased proliferation in the subpopulation, which was not measurable in our hands. Staining for BrdU requires acid treatment of samples to unwind the DNA, which is not compatible with GFP staining as it destroys GFP epitopes [237]. Consequently, other techniques such as 5-ethynyl-2'-deoxyuridine (EdU) click assays that do not require denaturation or staining for mitotic marker such as pHH3 might provide a better alternative [238].

An additional factor influencing oncogenic effects could be the difference between *in vitro* and *in vivo* microenvironments. Our *in vitro* culture conditions are missing extracellular matrix and complex paracrine mechanisms that are usually provided by the surrounding brain tissue and other cell types such as astrocytes or microglia [208]. The viability of SMARCA4-negative cells might depend on this scaffold as a suitable tumor microenvironment. Therefore, we transplanted our altered GCPs into immunodeficient mice to evaluate tumorigenic potential *in vivo*.

4.2.2 Development of a SMARCA4-deficient Group 3 medulloblastoma model

Transplantation of SMARCA4-deficient MYC transduced GCPs successfully induced brain tumor formation in mice with a penetrance of 26.3%. Histological analysis and PCR for recombinated *Smarca4* revealed that these tumors originated from the small SMARCA4-negative GFP-positive subpopulation, which accounted for 8.4% in our original culture. Most other Group 3 MB models were generated by transplanting cells after selection for markers by FACS sorting [120, 176, 178]. The choice to transplant the whole culture without preselection in our experiments was based on the high sensitivity of SMARCA4 knockdown cells that we experienced. Even slight differences in the time needed for the isolation of cells, the exact cell numbers seeded per well or the amount of lentivirus added had severe consequences on the viability and morphology *in vitro*. We hypothesized that if both concurrent alterations harbored oncogenic potential, the respective cells would be positively selected during tumor development, which was proven by SMARCA4-negativity in

all tumors. We transplanted a total amount of 1.5 mio cells, which corresponds to approximately $0.08 \times 1.5 \text{ mio} = 120,000$ cells harboring both *Smarca4* alteration and MYC overexpression. Kawachi *et al.* were able to drive formation of primary MB with a penetrance of around 60% by injecting only 50,000 FACS sorted cells [176]. However, penetrance reached 100% when 2×10^6 cells were injected [176]. Other groups have also worked with a higher number at around 1×10^6 transplanted cells in orthotopic MB mouse models [206, 239]. Consequently, a higher cell number might increase penetrance of our model although an additional number of *Math1-creER^{T2}::Smarca4^{f/f}* pups for GCP isolation would be needed. Another factor contributing to reduced penetrance could be the remaining immunogenicity of *CD1^{nu/nu}* mice. Although these animals lack a thymus and are unable to produce T-cells, they still harbor B-cells and natural killer cells that could eliminate potentially tumorigenic cells [184]. In contrast to that, NOD scid gamma (NSG) mice are deficient in T-cell and natural killer cell production as well as multiple cytokine signaling pathways and might provide higher efficiency in engraftment of tumor cells [240]. As previous transplantations into immunocompetent *C57Bl6/J* mice by our research group did not succeed, we did not consider this option.

We thoroughly characterized our mouse model by performing histology, RNA sequencing, and DNA methylation analysis to assess comparability to human brain tumors. Histologically, tumors revealed anaplastic features and a high degree of apoptosis, which is consistent with LCA histology observed in human MB, a histological subtype most frequently detected in Group 3 MB [90, 115]. Similar observations were made in previously generated MYC-driven Group 3 MB mouse models [177, 178]. Moreover, NSC markers Nestin and SOX2 were expressed in tumors, whereas no signal for neural marker NeuN was detected, which further emphasizes the undifferentiated nature of tumor cells.

In molecular analysis, both gene expression and methylation data showed similarities of our model to human Group 3 MB. However, proximity to SHH MB was also evident. The reason for this resemblance most probably lies in the cellular origin of our tumors. SHH MB develop from GCPs as previously demonstrated in several mouse models and confirmed by comparisons to single-cell sequencing data of murine and human cell populations [60, 117, 209, 241]. Since all cells within our tumors showed a loss of SMARCA4 through cre-loxP recombination, we can confidently assume the origin of our tumors to also lie in *Math1*-positive GCPs rather than other cerebellar progenitor populations that might have been left in our cell culture. GCPs are among many other neural progenitor populations that have been used before to model Group 3 MB in mice [177-179]. This fits to the fact that the exact cellular origin of Group 3 MB cannot be clearly assigned to a single murine cell population in the brain [60]. However, recently published works by Smith *et al.*

and Hendrikse *et al.* provide evidence for both Group 3 and 4 MB originating from a distinct cell population in the subventricular zone of the human rhombic lip [117, 119]. In humans, the rhombic lip shows a clear division into a ventricular and a subventricular zone and is internalized in the nodulus later in development [119]. In contrast to that, the murine rhombic lip does not show any division and is only present in early brain development [134]. Therefore, the cellular origin needed for an accurate Group 3 MB model might not even exist in mice, which questions the suitability of not only our but also all other previously published mouse models.

Another limitation of our model is the technical complexity, which hampers reproducibility. Cell culture conditions, lentiviral batches, and the manual stereotactic injections might greatly influence the level of MYC overexpression and the efficiency of engraftment. The resulting heterogeneity within our mouse tumors is clearly represented not only in their gene expression profiles but also in their time of occurrence (time span of four weeks to five months after transplantation). Hence, a GEMM with a timed and specific MYC overexpression and SMARCA4 loss might provide a more reliable and less labor-intensive alternative.

Despite questionable cells of origin and methodological difficulties in our tumor model, we made one important new observation: The loss of SMARCA4 drives the formation of MYC-driven brain tumors. Ballabio *et al.* have shown before that an overexpression of SMARCA4 wildtype represses tumor development in an OTX2/MYC MB mouse model [131]. The other way around, the selection for SMARCA4-negative cells in our model now confirmed the tumor-driving mechanism behind a SMARCA4 deficiency. Since recent publications have shown that MYC overexpression on its own can induce MB formation, we questioned whether this loss of SMARCA4 represents the second hit needed for tumorigenesis or only accelerates tumor development. Tao *et al.* generated a Group 3 MB model by transplanting SOX2-positive neural progenitors transduced with a MYC^{T58A} lentivirus, which reliably resulted in tumor formation without a second oncogenic hit [178]. Within the same setting, MYC^{T58A} transduction of SOX2-negative populations – which also include GCPs – only rarely generated tumors [178]. Moreover, overexpression of wildtype MYC alone did not suffice to induce MB formation in a previous study [177]. Consequently, in our tumor model, aberrant chromatin remodeling by the loss of SMARCA4 might cause stabilization of wildtype MYC required for the development of tumors. In a recently developed transgenic model, Mainwaring *et al.* induced wildtype MYC overexpression in GLT-1-positive hindbrain progenitors to successfully drive MB formation [179]. However, GLT-1 is expressed throughout the whole hindbrain in embryonic development and does not specifically affect GCPs. Therefore, it remains unclear if MYC overexpression alone can induce tumorigenesis in GCPs. To address this issue, we transplanted additional cohorts of *CD1^{nu/nu}* mice using not only GCPs harboring both alterations but also GCPs with

a MYC overexpression only. However, no tumor development was detected in any of the new cohorts, including positive controls. Several adjustments of cell culture conditions, freshly ordered materials, and new batches of lentivirus or Matrigel in following attempts could not resolve this problem of reproducibility. Therefore, we decided to terminate the transplantations for animal welfare reasons.

Still, the thorough investigation of tumor material from our first cohort comprising five tumors provided us with valuable insights into the development of MYC driven MB and the involvement of SMARCA4 in tumorigenesis. We showed comparability to human Group 3 MB in both histology, gene expression, and methylation analysis and confirmed a selection for SMARCA4-negative cells in tumor development. Additionally, comparisons between gene expression profiles of our tumor model and an established SHH MB model provided us with insights into pathways and genes that could be specifically involved in tumorigenesis of SMARCA4-deficient MYC driven tumors. Upregulated gene sets in our tumor model mainly included terms associated with synaptic signaling and transmembrane transport, while upregulated pathways involved G protein signaling and glucose metabolism. Tao *et al.* have identified altered glucose metabolic pathways in their MYC driven tumors and were successful in treating tumor cells with specific inhibitors to upregulated lactate dehydrogenase A [178]. Similarly, genes upregulated in our tumors might provide new therapeutic targets that could be investigated in follow-up studies as soon as a MYC driven SMARCA4-deficient model can be stably established.

4.3 SMARCA4 in the Development of WNT Medulloblastoma

In order to model SMARCA4 altered WNT MB in mice, we modified a mouse model previously described by Gibson *et al.* (*Blb-cre::Ctnnb1(ex3)^{fl/wt}::Trp53^{fl/fl}*), which uses a stabilizing mutation of β -catenin combined with a loss of p53 to drive MB formation in the brain stem of mice [105]. Although both mutations used in the previously published tumor model have been described in WNT MB patients, the low penetrance (15%) and long latency contraindicates accurate modeling of a pediatric tumor [105]. An additional introduction of a *Pik3ca* mutation in *Blb-cre::Ctnnb1(ex3)^{fl/wt}::Trp53^{fl/fl}::Pik3ca^{fl/wt}* mice results in a 100% penetrance for MB development with significantly reduced latency [127]. However, although mutations of *TP53* or *PIK3CA* occur in WNT MB patients (each at a frequency of 5-10%), the combination of both alterations has not been detected throughout several MB cohorts, which could limit practicality of this model [106, 173]. In contrast, concurrent mutations of *CTNNB1* and *SMARCA4* are detected in around 20% of WNT MB patients [70, 103, 106, 127]. Therefore, we combined both alterations in our

mouse model *Blbp-cre::Ctnnb1(ex3)^{fl/wt}::Smarca4^{fl/fl}*, attempting to model SMARCA4-deficient WNT MB.

4.3.1 Unexpected phenotypes of *Blbp-cre::Ctnnb1(ex3)^{fl/wt}* mutants

Our first observation was the severe phenotype of *Blbp-cre::Ctnnb1(ex3)^{fl/wt}* mice with short survival, severe hydrocephalus, and hypoplastic cerebella, which was not described by Gibson *et al.* before [105]. As both the *Blbp-cre* and *Ctnnb1(ex3)^{fl/fl}* strain were originally obtained from the same source, we first attributed this effect to a different genetic background of our mice. Genetic background has previously been shown to greatly influence observed phenotypes in GEMMs [161, 162]. Therefore, we first performed backcrossing of our *Ctnnb1(ex3)^{fl/fl}* line with a previously unknown mixed background for at least five generations to generate a pure *C57Bl6/J* background. Simultaneously, we performed backcrossing of our *C57Bl6/J Blbp-cre* mice to a *129S2/Sv* background. However, both variations did not result in any alterations of the observed phenotype in *Blbp-cre::Ctnnb1(ex3)^{fl/wt}* offspring (data not shown). Therefore, we continued on a pure *C57Bl6/J* background for all further analysis. Additionally, we used RFP fate mapping mice to track expression of cre at embryonic stages for a comparison with previously published expression patterns. While Gibson *et al.* described BLBP expression in the cerebellum mostly restricted to the germinal zones at E14.5 [105], our *Blbp-cre* line showed much broader recombination, including the whole developing cerebellum at E14.5. This discrepancy could easily explain the different phenotypes observed. In fact, our model displayed a phenotype quite similar to previously described *hGFAP-cre::Ctnnb1(ex3)^{fl/wt}* mice displaying hydrocephalus, hypoplastic cerebella, and underdeveloped cerebral cortices [242]. Consequently, it is quite probable that our *Blbp-cre* line targets similar cell populations as *hGFAP-cre* in the brain. This is further supported by the phenotypes observed in our *Blbp-cre::Smarca4^{fl/fl}* mice. At P0, they already displayed a severe hydrocephalus, thinned cortex, and hypoplastic cerebellum. This is in line with previously reported findings on *hGFAP-cre::Smarca4^{fl/fl}* mice with underdeveloped cerebella and cerebral cortices [165]. A mix up of mouse lines per accident was ruled out by the detection of lacZ in both PCR analysis of our *Blbp-cre* mice and in single-cell RNA sequencing data of cerebellar lesions, since lacZ is not present in any other cre line used in our laboratory (data not shown). Therefore, we hypothesize that the difference in cre expression is a result of genetic drift between our *Blbp-cre* line and other previously used colonies, which is a common phenomenon for inbred mouse strains [243-245].

The fact that both cell accumulations in the brain stem as well as in the cerebellum of our *Blbp-cre::Ctnnb1(ex3)^{fl/wt}* mice showed a low degree of proliferation points towards a neurodevelopmental disorder rather than the development of tumorous lesions. Brain stem lesions were also

detected by Gibson *et al.* and were attributed to stalled migration of mossy fiber neuron precursors [105]. Similarly, cell accumulations in the cerebellum of our *Blbp-cre::Ctnnb1(ex3)^{fl/wt}* mice could consist of neural progenitors that are unable to differentiate and migrate to their final position in the cerebellum. Positive stainings for SOX2 and Nestin and negative stainings for markers associated with more differentiated cell types (parvalbumin, PAX6, S100, NeuN, and calbindin) also point towards an origin in early neural precursors. The fact that *Blbp-cre::Ctnnb1(ex3)^{fl/wt}::Smarca4^{fl/fl}* mice did not develop any lesions in the brain stem suggests that a loss of SMARCA4 prevents stalled migration of mossy fiber neuron precursors. Since SMARCA4 plays an important role in neurogenesis, a loss of SMARCA4 might hamper early differentiation towards this lineage, consequently also blocking the accumulation of cells [164, 165].

4.3.2 Cerebellar lesions induced by activated WNT signaling and SMARCA4 loss

The embryonic cerebellar lesions found in *Blbp-cre::Ctnnb1(ex3)^{fl/wt}::Smarca4^{fl/fl}* mutants displayed different characteristics than the postnatal cell accumulations described before. Firstly, they were highly proliferative and secondly, they expanded from E13.5 to E16.5 until covering a big part of the cerebellum. Lesions stained positive for SOX2, the expression of which is usually restricted to the ventricular zone at this developmental stage. Additionally, the development of lesions seemed to prevent the formation and migration of PAX2-positive interneuron progenitors. This observation combined with the localization of lesions growing from the ventricular zone inwards suggests an origin in GABAergic progenitors, which reside in the ventricular zone in embryonic brain development and give rise to Purkinje cells and inhibitory interneurons [135, 136]. However, Zhang *et al.* have recently described a SOX2-positive progenitor cell population that can give rise to cerebellar precursors of both upper rhombic lip and ventricular zone [246]. When these precursors are labelled at E10.5, they can later be found equally distributed between both germinal zones, giving rise to all known cerebellar precursors, including GABAergic and glutamatergic populations [246]. This more primitive progenitor cell population might also be a target of BLBP-targeted recombination, which is expressed in mouse brains from E9.5 on [149].

We analyzed *Blbp-cre::Ctnnb1(ex3)^{fl/wt}::Smarca4^{fl/fl}* mice throughout embryonic brain development and saw that up until E16.5, mutants were counted at expected Mendelian ratio. This was not the case at E18.5, where four litters did not yield any mice with the desired genotype and at P0, where only 26% of expected mice were born. Consequently, we concluded prenatal lethality induced by the expanding cerebellar lesions. The few mutants born and analyzed at P0 did not display any lesions although a loss of SMARCA4 in the cerebellum was evident. However, PCR revealed missing recombination of *Ctnnb1* in these mice, which suggested insufficient recombina-

tion causing the missing phenotype and delayed death. Different degrees of recombination between animals of the same genotype have been described before, for example when cre expression is driven by the GFAP promoter [242, 247]. Moreover, floxed alleles have differential sensitivities to cre-mediated recombination, which could explain a more efficient recombination of *Smarca4* than *Cttnb1* in this case [156, 248].

Additionally, we detected germline recombination of *Smarca4* in all offspring of cre-positive mothers. A recent evaluation of recombination in CNS-specific cre-driver lines revealed unexpected germline recombination as a very common phenomenon, affecting more than half of all commonly used lines [156]. The early loss of one *Smarca4* allele in our model seemed to greatly influence phenotypes since only mutants derived from cre-positive mothers developed cerebellar lesions. Hence, our observations further stress the necessity to test for germline recombination in every new cre-driven mouse model to avoid false conclusions. What remains unexplored is if the reason for the presence of cerebellar lesions only in mutants derived from cre-positive mothers lies in a more efficient recombination or in the surrounding brain tissue harboring a heterozygous loss of *Smarca4*.

Cerebellar lesions did not resemble early tumorous lesions in the WNT MB mouse model *Blbp-cre::Cttnb1(ex3)^{fl/wt::Trp53^{fl/fl}}* [105] considering their localization in the brain stem as well as their disturbed blood brain barrier, which seemed intact in our lesions according to GLUT-1 stainings. Gibson *et al.* used this mouse model to convincingly demonstrate the origin for WNT MB to lie in progenitor cells derived from the lower rhombic lip. Jessa *et al.* confirmed these findings by comparing WNT MB bulk gene expression data to a single-cell transcriptome atlas of the murine and human developing brain and more specifically defined the origin in the pontine mossy fiber neuron population [249]. Hence, our model most probably does not recapitulate the biological origin of WNT MB. This was also reflected by our comparison of global DNA methylation of cerebellar lesions to human brain tumors, which did not yield a reliable match. However, the transformation of cells in the cerebellar ventricular zone by mutation of β -catenin and SMARCA4 loss raises the question if other cell populations might be prone to tumor development upon deregulation of WNT signaling and chromatin remodeling. Moreover, our *Blbp-cre::Cttnb1(ex3)^{fl/wt::Smarca4^{fl/fl}}* model is the first one to show a cooperative effect between mutated β -catenin and loss of SMARCA4 in promoting extensive proliferation of cells. Robinson *et al.* have hypothesized before that the development of WNT MB requires disruption of chromatin remodeling at WNT responsive genes additional to stabilization of β -catenin by mutation [127]. This is reflected by the finding that WNT MBs not only show a high frequency of *SMARCA4* muta-

tions but also of other chromatin modifiers such as acetyltransferase *CREBBP*, BAF complex subunits *ARID1A/ARID2*, or methyl transferase *KMT2D* [70, 106, 127]. It has been shown before that nuclear β -catenin can directly interact with both SMARCA4 and CREBBP proteins to regulate transcription of WNT-responsive genes [250]. This interaction might be essential for the transformation of cells since both *Cttnb1* and *Smarca4* alterations on their own did not suffice to form lesions in our mouse model. Nevertheless, Gibson *et al.* have shown that a p53 loss can cooperate with mutated β -catenin to drive MB formation in mice without alterations in chromatin modifying genes [105]. Consequently, disrupted chromatin remodeling might only be one of several tumor driving mechanisms in WNT MB.

4.3.3 Molecular analysis of cerebellar lesions

To analyze cerebellar lesions of *Blbp-cre::Cttnb1(ex3)^{fl/wt::Smarca4^{fl/fl}}* mice on a molecular level, we performed both methylation analysis and single-cell gene expression analysis of E16.5 cerebella. The methylation profile of cerebellar lesions did not show a clear match with a human brain tumor entity. In case of WNT MB, this can be attributed to the cellular origin of lesions that lies in the cerebellar ventricular zone rather than in pontine mossy fiber neuron populations as previously discussed [249]. Other brain tumor entities besides WNT MB are only rarely affected by *CTNNB1* mutations [251-253]. We have seen before that murine embryonic control tissue frequently clusters with ATRT in UMAPs, which might explain the clustering of our cerebellar lesions with this entity, probably attributed to the undifferentiated nature of both groups.

A comparison of DNA methylation profiles of cerebellar lesions to control cerebella at E16.5 revealed deregulated methylation in processes involved in nervous system development, signal transduction, cytoskeleton organization, transmembrane transport, protein phosphorylation, and cell migration. The influence of altered *Cttnb1* and *Smarca4* on nervous system development is evident considering the severe developmental phenotypes observed in postnatal brains. Moreover, the terms signal transduction, transmembrane transport, and protein phosphorylation all include mechanisms associated with WNT signaling since the loss of exon 3 of *Cttnb1* in our model prevents phosphorylation and thus degradation of β -catenin [185]. Deregulated cell migration is reflected by the migration of proliferative cells within the lesions inside the developing cerebellum. Furthermore, remodeling of the actin and tubulin cytoskeleton is essential for brain tumor cell migration and invasion and emphasizes the potentially tumorigenic nature of alterations in the cerebellar lesions [254, 255].

In single-cell gene expression analysis, we identified distinct clusters in the mutant cerebellum that showed increased expression of SOX2 and activation of WNT signaling target genes. A com-

parison with a murine single-cell atlas revealed characteristics of radial glia cells with a resemblance to cellular ages earlier than E16.5. Altogether, these results further emphasize the previously suspected origin of cerebellar lesions in early progenitor cells. The fact that a large portion of glutamatergic cerebellar cells was missing in mutants compared to controls suggests that progenitors of the glutamatergic lineage were also affected by recombination. This observation provides further reason to consider the origin of lesions in the SOX2-positive bipotent progenitor population described by Zhang *et al.* [246]. Additionally, we identified high mitotic activity in one of the mutant clusters, which might be worth further characterizing. Therefore, in a next step, gene set enrichment analysis of single-cell clusters will be performed to elucidate pathways and gene signatures that could be associated with the development of cerebellar lesions driven by aberrant WNT signaling and SMARCA4 loss.

4.3.4 Tumorigenic potential of cerebellar lesions

In vitro, hindbrain progenitor cells (HPCs) of *Blbp-cre::Ctnnb1(ex3)^{fl/wt::Smarca4^{fl/fl}}* mutants did not show increased proliferation and were prone to selection for non-recombined cells over time. We have shown before that SMARCA4-deficient neurospheres have a selection disadvantage *in vitro*, which was also recapitulated in GCP cultures of *Math1-creERT2::Smarca4^{fl/fl}* mice after SMARCA4 knockdown within this project [169]. However, even when mutant HPCs were directly transplanted into adult immunodeficient mice after singularization, they did not induce brain tumor formation. This observation suggests that the cerebellar lesions found in our model do not harbor neoplastic potential after all. Still, there is a chance that the tumorigenic potential of *Ctnnb1* and *Smarca4* altered cells is dependent on an embryonic microenvironment that cannot be provided by adult brain tissue of immunodeficient mice. Since mutants with cerebellar lesions do not survive past E16.5, further tracing of tumor development *in vivo* is not feasible. However, cerebellar explants or culture of brain slices could provide an alternative to study cerebellar cells *in vitro* while providing a scaffold including extracellular matrix and a variety of surrounding embryonic cell types [256, 257]. Alternatively, transplantation of mutant HPCs into younger mice such as P0 pups might provide a more suitable environment for the development of tumors [258, 259].

4.4 Conclusions and Outlook

In the data presented here, we found evidence for a tumor-driving role of deficient SMARCA4 in the development of MB. Although viability of MB cell lines and primary neural cells was not altered upon overexpression of mutated SMARCA4 alone, the cooperative effect of a SMARCA4 deficiency with other frequently detected alterations in MB was demonstrated *in vivo* using two different mouse models.

In our first mouse model, we generated brain tumors resembling Group 3 MB by transplanting SMARCA4-deficient and MYC transduced GCPs in immunodeficient mice. Despite methodological complications hampering the use of this model in further studies, the fact that both alterations cooperate in tumorigenesis paves the way for future investigations. The additional introduction of a SMARCA4 knockdown in recently described MYC-driven MB models by Mainwaring *et al.* or Morcavallo *et al.* could provide further proof for the influence of a SMARCA4 loss on penetrance or latency of tumors [179, 260]. In a next step, it might be interesting to explore therapeutic options specifically for SMARCA4-deficient MB. Several studies have suggested HDAC inhibitors for treating MYC-driven Group 3 MB with efficacy shown both in cell lines *in vitro* and in mouse models *in vivo* [261-263]. However, Romero *et al.* have shown that SMARCA4-deficient cells do not respond to HDAC inhibition but in contrast are sensitive to KDM6A/B inhibition, even when MYC is concurrently amplified [58]. This observation emphasizes the importance of considering alternative treatment options for SMARCA4-deficient MB that could be explored in stably established mouse tumor models.

In our second mouse model *Blbp-cre::Ctnnb1(ex3)^{fl/wt}::Smarca4^{fl/fl}*, we detected embryonic cerebellar lesions that suggest a cooperative effect of aberrant WNT signaling and a SMARCA4 deficiency in driving cell transformation. However, cells derived from these lesions neither showed a survival advantage *in vitro* nor induced brain tumor formation after transplantation in immunodeficient mice. Therefore, in a next step, we will investigate the influence of the microenvironment on cell viability by culturing cerebellar explants that contain not only recombined cerebellar progenitors but also surrounding matrix and a variety of embryonic cell types. Increased proliferation of recombined cells in this environment would provide further evidence for the important role of the microenvironment in supporting growth of SMARCA4-deficient cells.

Single-cell gene expression analysis of cerebellar lesions revealed distinct clusters in the mutant that were predicted younger in age with resemblance to radial glia cells. Some mutant clusters additionally showed upregulation of WNT target genes with mutant cluster 9 also displaying high

mitotic activity. However, it remains unclear which mutant cluster represents the origin of aberrant cells within the lesions. In this case, RNA velocity analysis will be performed to estimate trajectories from one cluster to another and hereby assign developmental stages [264].

Since recombination induced by our *Blbp-cre* line was widely spread across the whole brain and induced severe developmental phenotypes and early death of mutants, future investigations *in vivo* should focus on a more targeted approach. To induce recombination more specifically in the lower rhombic lip as the proposed origin for WNT MB, other cre lines such as *Olig3-creER^{T2}* might be worth exploring [265]. Furthermore, the detection of both recombination divergent from published studies and unexpected germ line recombination in our mouse line taught us to routinely test for these issues in future mouse experiments.

Altogether, we hope that our evidence for a tumor-driving role of a SMARCA4 loss in MB leads the way to improved SMARCA4-deficient MB tumor models in the future. Those models could provide a valuable platform to explore specific therapeutic options for affected patients and should be analyzed with special attention to the role of the microenvironment in tumorigenesis.

5 ABSTRACT

SMARCA4 is a catalytic subunit of the BAF (BRG1/BRM-associated factor) chromatin remodeling complex, which acts as a regulator of chromatin accessibility and gene expression in mammals. Alterations of *SMARCA4* are frequently detected in medulloblastoma (MB), the most common malignant pediatric brain tumor. MB can be divided into the four molecular subgroups Sonic Hedgehog (SHH), Wingless/Int-1 (WNT), Group 3, and Group 4, of which mainly WNT and Group 3 MB are affected by *SMARCA4* mutations. However, the functional role of these alterations in tumorigenesis has not been deciphered yet. Therefore, we designed lentiviral constructs for the overexpression of mutant SMARCA4 variants to assess effects on cell viability *in vitro*. Additionally, we combined a knockdown of SMARCA4 with subgroup-specific alterations of WNT and Group 3 MB in two different mouse models.

In our *in vitro* approach, we transduced three MB cell lines and primary murine granule cell precursors (GCPs) with mutant SMARCA4 variants T910M and R1135W. Both variants were previously identified in MB patients and are known to induce a loss of function. We successfully demonstrated functionality of our plasmids. However, overexpression of SMARCA4 wildtype and mutant variants did not influence viability of cell lines or primary cells *in vitro*.

In a next step, we successfully generated a SMARCA4-deficient MB mouse model by combining an overexpression of MYC with a loss of SMARCA4 in GCPs *in vitro* with subsequent transplantation into immunodeficient mice. Tumors developed in 5 out of 19 mice with a high resemblance to Group 3 MB in both gene expression and DNA methylation analysis. SMARCA4 loss was evident in all tumor cells, suggesting a dependency of tumor growth on the *Smarca4* alteration.

Lastly, we modified a previously published WNT MB mouse model by combining a mutation in the β -catenin gene *Cttnb1* with a loss of SMARCA4 in *Blbp-cre::Cttnb1(ex3)^{fl/wt::Smarca4^{fl/fl}}* mice. The combination of both alterations resulted in perinatal lethality of mice. However, we detected proliferative cerebellar lesions at embryonic age, which suggest a cooperative effect of altered WNT signaling and SMARCA4 loss in driving cell transformation. We thoroughly analyzed these lesions both histologically and on a molecular level by DNA methylation analysis and single-cell RNA sequencing analysis. Our results indicate an origin in early SOX2-positive cerebellar progenitors.

Taken together, these results provide evidence for a tumor-driving role of *SMARCA4* alterations in both MYC-driven MB as well as in cooperation with aberrant WNT signaling.

6 ZUSAMMENFASSUNG

SMARCA4 ist eine katalytische Untereinheit des BAF (BRG1/BRM-assoziiertes Faktor) Chromatin Remodeling Komplexes, welcher die Zugänglichkeit von Chromatin und somit auch die Genexpression in Säugetieren reguliert. Obwohl Medulloblastome (MB), die häufigsten malignen pädiatrischen Hirntumore, oft von Mutationen im *SMARCA4* Gen betroffen sind, verbleibt die funktionelle Rolle dieser Alterationen bislang unklar. Von den vier molekularen MB-Subgruppen (Wingless/Int-1 (WNT), Sonic Hedgehog (SHH), Gruppe 3 und Gruppe 4) weisen vor allem WNT und Gruppe 3 MB häufig *SMARCA4* Mutationen auf. Innerhalb dieses Projekts untersuchten wir Effekte dieser Mutationen zunächst durch die Überexpression von *SMARCA4* Varianten *in vitro*. Zusätzlich kombinierten wir einen Knockdown von *SMARCA4* mit Subgruppen-spezifischen Alterationen von WNT und Gruppe 3 MB in zwei unabhängigen Mausmodellen.

Insgesamt transduzierten wir drei MB-Zelllinien und primäre murine Körnerzellvorläufer mit den mutierten *SMARCA4* Varianten T910M und R1135W. Beide Varianten wurden zuvor in MB-Patienten identifiziert und führen zu einem Funktionsverlust des Proteins. Trotz erwiesener Funktionalität unserer Konstrukte konnten wir keinen Einfluss von Wildtyp oder mutiertem *SMARCA4* auf die Viabilität von Zelllinien oder primären Zellen *in vitro* feststellen.

In unserem ersten *in vivo* Ansatz generierten wir ein *SMARCA4*-defizientes MB-Mausmodell, indem wir eine Überexpression von *MYC* mit einem Verlust von *SMARCA4* in Körnerzellvorläufern kombinierten. Nach Transplantation in immundefiziente Mäuse entwickelten 5 von 19 Tieren Tumoren, deren DNA-Methylierung und Genexpressionsprofile große Ähnlichkeiten zu Gruppe 3 MBs aufzeigten. Der Verlust von *SMARCA4* in allen Tumorzellen wies auf eine Abhängigkeit der Tumorentwicklung von der eingebrachten *Smarca4* Veränderungen hin.

Schlussendlich modifizierten wir ein zuvor publiziertes WNT MB Mausmodell, indem wir eine Mutation im β -Catenin Gen *Ctnnb1* mit einem *SMARCA4* Verlust in *Blbp-cre::Ctnnb1(ex3)^{fl/wt::Smarca4^{fl/fl}}* Mäusen kombinierten. Diese Tiere waren nicht lebensfähig, entwickelten jedoch im embryonalen Alter große proliferative Läsionen im Kleinhirn. Dies suggeriert einen kooperativen Effekt des aktivierten WNT-Signalwegs mit einem Verlust von *SMARCA4* in der Transformation von Zellen. Eine ausgiebige Charakterisierung der Histologie, DNA Methylierung und Einzelzell-Genexpression in den Läsionen deutete auf einen Ursprung in SOX2-positiven zerebellären Vorläufern hin.

Zusammenfassend liefern die Ergebnisse dieser Studien neue Hinweise auf einen tumortreibenden Effekt von *SMARCA4* Veränderungen sowohl in *MYC*-getriebenen MB als auch in Kooperation mit einer Überaktivierung des WNT-Signalwegs.

7 REFERENCES

1. McGinty, R.K. and S. Tan, *Nucleosome structure and function*. Chem Rev, 2015. **115**(6): p. 2255-73.
2. Kouzarides, T., *Chromatin Modifications and Their Function*. Cell, 2007. **128**(4): p. 693-705.
3. Clapier, C.R., et al., *Mechanisms of action and regulation of ATP-dependent chromatin-remodelling complexes*. Nat Rev Mol Cell Biol, 2017. **18**(7): p. 407-22.
4. Stern, M., R. Jensen, and I. Herskowitz, *Five SWI genes are required for expression of the HO gene in yeast*. J Mol Biol, 1984. **178**(4): p. 853-68.
5. Neigeborn, L. and M. Carlson, *Genes affecting the regulation of Suc2 gene expression by glucose repression in saccharomyces cerevisiae*. Genetics, 1984. **108**(4): p. 845-58.
6. Whitehouse, I., et al., *Nucleosome mobilization catalysed by the yeast SWI/SNF complex*. Nature, 1999. **400**(6746): p. 784-87.
7. Peterson, C.L. and I. Herskowitz, *Characterization of the yeast SWI1, SWI2, and SWI3 genes, which encode a global activator of transcription*. Cell, 1992. **68**(3): p. 573-83.
8. Kadoch, C., et al., *Proteomic and bioinformatic analysis of mammalian SWI/SNF complexes identifies extensive roles in human malignancy*. Nat Genet, 2013. **45**(6): p. 592-601.
9. Mashtalir, N., et al., *Modular Organization and Assembly of SWI/SNF Family Chromatin Remodeling Complexes*. Cell, 2018. **175**(5): p. 1272-88.
10. Ronan, J.L., W. Wu, and G.R. Crabtree, *From neural development to cognition: unexpected roles for chromatin*. Nat Rev Genet, 2013. **14**(5): p. 347-59.
11. Wang, W., et al., *Purification and biochemical heterogeneity of the mammalian SWI-SNF complex*. EMBO J, 1996. **15**(19): p. 5370-82.
12. Bögershausen, N. and B. Wollnik, *Mutational Landscapes and Phenotypic Spectrum of SWI/SNF-Related Intellectual Disability Disorders*. Front Mol Neurosci, 2018. **11**: p. 252.
13. Strohner, R., et al., *A 'loop recapture' mechanism for ACF-dependent nucleosome remodeling*. Nat Struct Mol Biol, 2005. **12**(8): p. 683-90.
14. Zofall, M., et al., *Chromatin remodeling by ISW2 and SWI/SNF requires DNA translocation inside the nucleosome*. Nat Struct Mol Biol, 2006. **13**(4): p. 339-46.
15. Kadoch, C., et al., *Dynamics of BAF-Polycomb complex opposition on heterochromatin in normal and oncogenic states*. Nat Genet, 2017. **49**(2): p. 213-22.
16. Ho, L., et al., *esBAF facilitates pluripotency by conditioning the genome for LIF/STAT3 signalling and by regulating polycomb function*. Nat Cell Biol, 2011. **13**(8): p. 903-13.
17. Zhang, Z.K., et al., *Cell cycle arrest and repression of cyclin D1 transcription by INI1/hSNF5*. Mol Cell Biol, 2002. **22**(16): p. 5975-88.

18. Nagl, N.G., Jr., et al., *Distinct mammalian SWI/SNF chromatin remodeling complexes with opposing roles in cell-cycle control*. EMBO J, 2007. **26**(3): p. 752-63.
19. Kaeser, M.D., et al., *BRD7, a novel PBAF-specific SWI/SNF subunit, is required for target gene activation and repression in embryonic stem cells*. J Biol Chem, 2008. **283**(47): p. 32254-63.
20. Debril, M.B., et al., *Transcription factors and nuclear receptors interact with the SWI/SNF complex through the BAF60c subunit*. J Biol Chem, 2004. **279**(16): p. 16677-86.
21. Link, K.A., et al., *BAF57 governs androgen receptor action and androgen-dependent proliferation through SWI/SNF*. Mol Cell Biol, 2005. **25**(6): p. 2200-15.
22. Euskirchen, G.M., et al., *Diverse roles and interactions of the SWI/SNF chromatin remodeling complex revealed using global approaches*. PLoS Genet, 2011. **7**(3): p. e1002008.
23. Morrison, E.A., et al., *DNA binding drives the association of BRG1/hBRM bromodomains with nucleosomes*. Nat Commun, 2017. **8**: p. 16080.
24. Allen, M.D., et al., *The SWI/SNF Subunit INI1 Contains an N-Terminal Winged Helix DNA Binding Domain that Is a Target for Mutations in Schwannomatosis*. Structure, 2015. **23**(7): p. 1344-49.
25. Lessard, J., et al., *An essential switch in subunit composition of a chromatin remodeling complex during neural development*. Neuron, 2007. **55**(2): p. 201-15.
26. Staahl, B.T., et al., *Kinetic analysis of npBAF to nBAF switching reveals exchange of SS18 with CREST and integration with neural developmental pathways*. J Neurosci, 2013. **33**(25): p. 10348-61.
27. Braun, S.M.G., et al., *BAF subunit switching regulates chromatin accessibility to control cell cycle exit in the developing mammalian cortex*. Genes Dev, 2021. **35**(5-6): p. 335-53.
28. Tuoc, T., et al., *Ablation of BAF170 in Developing and Postnatal Dentate Gyrus Affects Neural Stem Cell Proliferation, Differentiation, and Learning*. Mol Neurobiol, 2017. **54**(6): p. 4618-35.
29. Hota, S.K., et al., *Dynamic BAF chromatin remodeling complex subunit inclusion promotes temporally distinct gene expression programs in cardiogenesis*. Development, 2019. **146**(19): p. e174086.
30. de la Serna, I.L., K.A. Carlson, and A.N. Imbalzano, *Mammalian SWI/SNF complexes promote MyoD-mediated muscle differentiation*. Nat Genet, 2001. **27**(2): p. 187-90.
31. Ohkawa, Y., C.G. Marfella, and A.N. Imbalzano, *Skeletal muscle specification by myogenin and Mef2D via the SWI/SNF ATPase Brg1*. EMBO J, 2006. **25**(3): p. 490-501.
32. Lickert, H., et al., *Baf60c is essential for function of BAF chromatin remodelling complexes in heart development*. Nature, 2004. **432**(7013): p. 107-12.
33. Qi, W., et al., *BRG1 promotes the repair of DNA double-strand breaks by facilitating the replacement of RPA with RAD51*. J Cell Sci, 2015. **128**(2): p. 317-30.
34. Peng, G., et al., *BRIT1/MCPH1 links chromatin remodelling to DNA damage response*. Nat Cell Biol, 2009. **11**(7): p. 865-72.

35. Watanabe, R., et al., *SWI/SNF factors required for cellular resistance to DNA damage include ARID1A and ARID1B and show interdependent protein stability*. *Cancer Res*, 2014. **74**(9): p. 2465-75.
36. Vogel-Ciernia, A., et al., *The neuron-specific chromatin regulatory subunit BAF53b is necessary for synaptic plasticity and memory*. *Nat Neurosci*, 2013. **16**(5): p. 552-61.
37. Cui, K., et al., *The chromatin-remodeling BAF complex mediates cellular antiviral activities by promoter priming*. *Mol Cell Biol*, 2004. **24**(10): p. 4476-86.
38. Hah, N., et al., *A role for BAF57 in cell cycle-dependent transcriptional regulation by the SWI/SNF chromatin remodeling complex*. *Cancer Res*, 2010. **70**(11): p. 4402-11.
39. Wieczorek, D., et al., *A comprehensive molecular study on Coffin-Siris and Nicolaides-Baraitser syndromes identifies a broad molecular and clinical spectrum converging on altered chromatin remodeling*. *Hum Mol Genet*, 2013. **22**(25): p. 5121-35.
40. Shain, A.H. and J.R. Pollack, *The spectrum of SWI/SNF mutations, ubiquitous in human cancers*. *PLoS One*, 2013. **8**(1): p. e55119.
41. Ramos, P., et al., *Loss of the tumor suppressor SMARCA4 in small cell carcinoma of the ovary, hypercalcemic type (SCCOHT)*. *Rare Dis*, 2014. **2**(1): p. e967148.
42. Jelinic, P., et al., *Concomitant loss of SMARCA2 and SMARCA4 expression in small cell carcinoma of the ovary, hypercalcemic type*. *Mod Pathol*, 2016. **29**(1): p. 60-66.
43. Fernando, T.M., et al., *Functional characterization of SMARCA4 variants identified by targeted exome-sequencing of 131,668 cancer patients*. *Nat Commun*, 2020. **11**(1): p. 5551.
44. Hodges, H.C., et al., *Dominant-negative SMARCA4 mutants alter the accessibility landscape of tissue-unrestricted enhancers*. *Nat Struct Mol Biol*, 2018. **25**(1): p. 61-72.
45. Hasselblatt, M., et al., *SMARCA4-mutated atypical teratoid/rhabdoid tumors are associated with inherited germline alterations and poor prognosis*. *Acta Neuropathol*, 2014. **128**(3): p. 453-56.
46. Holdhof, D., et al., *Atypical teratoid/rhabdoid tumors (ATRTs) with SMARCA4 mutation are molecularly distinct from SMARCB1-deficient cases*. *Acta Neuropathol*, 2021. **141**(2): p. 291-301.
47. Bai, J., et al., *BRG1 expression is increased in human glioma and controls glioma cell proliferation, migration and invasion in vitro*. *J Cancer Res Clin Oncol*, 2012. **138**(6): p. 991-98.
48. Koshy, M., et al., *Improved survival time trends for glioblastoma using the SEER 17 population-based registries*. *J Neurooncol*, 2012. **107**(1): p. 207-12.
49. Wang, Y., et al., *Brahma-Related Gene-1 (BRG1) promotes the malignant phenotype of glioblastoma cells*. *J Cell Mol Med*, 2021. **25**(6): p. 2956-66.
50. Peng, L., et al., *A Pan-Cancer Analysis of SMARCA4 Alterations in Human Cancers*. *Front Immunol*, 2021. **12**: p. e762598.

51. Guerrero-Martinez, J.A. and J.C. Reyes, *High expression of SMARCA4 or SMARCA2 is frequently associated with an opposite prognosis in cancer*. *Sci Rep*, 2018. **8**(1): p. 2043.
52. Modemann, F., et al., *P431: The role of SMARCA4 in hematopoiesis and acute myeloid leukemia*. *HemaSphere*, 2022. **6**: p. 331-32.
53. Wilson, B.G., et al., *Residual complexes containing SMARCA2 (BRM) underlie the oncogenic drive of SMARCA4 (BRG1) mutation*. *Mol Cell Biol*, 2014. **34**(6): p. 1136-44.
54. Oike, T., et al., *A synthetic lethality-based strategy to treat cancers harboring a genetic deficiency in the chromatin remodeling factor BRG1*. *Cancer Res*, 2013. **73**(17): p. 5508-18.
55. Giles, K.A., et al., *Integrated epigenomic analysis stratifies chromatin remodellers into distinct functional groups*. *Epigenetics Chromatin*, 2019. **12**(1): p. 12.
56. Helming, Katherine C., X. Wang, and Charles W.M. Roberts, *Vulnerabilities of Mutant SWI/SNF Complexes in Cancer*. *Cancer Cell*, 2014. **26**(3): p. 309-17.
57. Xue, Y., et al., *CDK4/6 inhibitors target SMARCA4-determined cyclin D1 deficiency in hypercalcemic small cell carcinoma of the ovary*. *Nat Commun*, 2019. **10**(1): p. 558.
58. Romero, O.A., et al., *SMARCA4 deficient tumours are vulnerable to KDM6A/UTX and KDM6B/JMJD3 blockade*. *Nat Commun*, 2021. **12**(1): p. 4319.
59. WHO_Classification_of_Tumours_Editorial_Board, *World Health Organization Classification of Tumours of the Central Nervous System*. 5th edition ed. 2021, Lyon: International Agency for Research on Cancer. p. 200-219.
60. Vladoiu, M.C., et al., *Childhood cerebellar tumours mirror conserved fetal transcriptional programs*. *Nature*, 2019. **572**(7767): p. 67-73.
61. Liu, Y., et al., *Risk Factors for Survival in Patients With Medulloblastoma: A Systematic Review and Meta-Analysis*. *Front Oncol*, 2022. **12**: p. e827054.
62. McKean-Cowdin, R., et al., *Trends in childhood brain tumor incidence, 1973-2009*. *J Neurooncol*, 2013. **115**(2): p. 153-60.
63. Smoll, N.R. and K.J. Drummond, *The incidence of medulloblastomas and primitive neuroectodermal tumours in adults and children*. *J Clin Neurosci*, 2012. **19**(11): p. 1541-44.
64. Stiller, C.A., et al., *Incidence of childhood CNS tumours in Britain and variation in rates by definition of malignant behaviour: population-based study*. *BMC Cancer*, 2019. **19**(1): p. 139.
65. Eibl, T., et al., *Medulloblastoma in adults; reviewing the literature from a surgeon's point of view*. *Aging*, 2021. **13**(2): p. 3146-60.
66. Jiang, T., et al., *A Retrospective Study of Progression-Free and Overall Survival in Pediatric Medulloblastoma Based on Molecular Subgroup Classification: A Single-Institution Experience*. *Front Neurol*, 2017. **8**: p. 198.
67. Johnston, D.L., et al., *Survival Following Tumor Recurrence in Children With Medulloblastoma*. *J Pediatr Hematol Oncol*, 2018. **40**(3): p. 159-63.

68. Mynarek, M., et al., *Nonmetastatic Medulloblastoma of Early Childhood: Results From the Prospective Clinical Trial HIT-2000 and An Extended Validation Cohort*. J Clin Oncol, 2020. **38**(18): p. 2028-40.
69. Dhall, G., et al., *Excellent outcome of young children with nodular desmoplastic medulloblastoma treated on "Head Start" III: a multi-institutional, prospective clinical trial*. Neuro Oncol, 2020. **22**(12): p. 1862-72.
70. Gajjar, A., et al., *Outcomes by Clinical and Molecular Features in Children With Medulloblastoma Treated With Risk-Adapted Therapy: Results of an International Phase III Trial (SJMB03)*. J Clin Oncol, 2021. **39**(7): p. 822-35.
71. Mynarek, M., et al., *Identification of low and very high-risk patients with non-WNT/non-SHH medulloblastoma by improved clinico-molecular stratification of the HIT2000 and I-HIT-MED cohorts*. Acta Neuropathol, 2023. **145**(1): p. 97-112.
72. Bhakta, N., et al., *The cumulative burden of surviving childhood cancer: an initial report from the St Jude Lifetime Cohort Study (SJLIFE)*. Lancet, 2017. **390**(10112): p. 2569-82.
73. King, A.A., et al., *Long-term neurologic health and psychosocial function of adult survivors of childhood medulloblastoma/PNET: a report from the Childhood Cancer Survivor Study*. Neuro Oncol, 2017. **19**(5): p. 689-98.
74. Thompson, E.M., et al., *Prognostic value of medulloblastoma extent of resection after accounting for molecular subgroup: a retrospective integrated clinical and molecular analysis*. Lancet Oncol, 2016. **17**(4): p. 484-95.
75. Toescu, S.M., et al., *Fourth ventricle tumors in children: complications and influence of surgical approach*. J Neurosurg Pediatr, 2021. **27**(1): p. 52-61.
76. Robertson, P.L., et al., *Incidence and severity of postoperative cerebellar mutism syndrome in children with medulloblastoma: a prospective study by the Children's Oncology Group*. J Neurosurg Pediatr, 2006. **105**(6): p. 444-51.
77. Moxon-Emre, I., et al., *Intellectual Outcome in Molecular Subgroups of Medulloblastoma*. J Clin Oncol, 2016. **34**(34): p. 4161-70.
78. Baroni, L.V., et al., *Bridging the treatment gap in infant medulloblastoma: molecularly informed outcomes of a globally feasible regimen*. Neuro Oncol, 2020. **22**(12): p. 1873-81.
79. Rutkowski, S., et al., *Treatment of Early Childhood Medulloblastoma by Postoperative Chemotherapy Alone*. NEJM, 2005. **352**(10): p. 978-86.
80. von Bueren, A.O., et al., *Treatment of young children with localized medulloblastoma by chemotherapy alone: Results of the prospective, multicenter trial HIT 2000 confirming the prognostic impact of histology*. Neuro Oncol, 2011. **13**(6): p. 669-79.
81. Lannering, B., et al., *Hyperfractionated Versus Conventional Radiotherapy Followed by Chemotherapy in Standard-Risk Medulloblastoma: Results From the Randomized Multicenter HIT-SIOP PNET 4 Trial*. J Clin Oncol, 2012. **30**(26): p. 3187-93.
82. Pompe, R.S., et al., *Intraventricular methotrexate as part of primary therapy for children with infant and/or metastatic medulloblastoma: Feasibility, acute toxicity and evidence for efficacy*. Eur J Cancer, 2015. **51**(17): p. 2634-42.

83. Palmer, S.L., et al., *Processing speed, attention, and working memory after treatment for medulloblastoma: an international, prospective, and longitudinal study*. J Clin Oncol, 2013. **31**(28): p. 3494-500.
84. Mynarek, M., et al., *SIOP PNET5 MB Trial: History and Concept of a Molecularly Stratified Clinical Trial of Risk-Adapted Therapies for Standard-Risk Medulloblastoma*. Cancers (Basel), 2021. **13**(23): p. e6077.
85. Orr, B.A., *Pathology, diagnostics, and classification of medulloblastoma*. Brain Pathol, 2020. **30**(3): p. 664-78.
86. McManamy, C.S., et al., *Nodule Formation and Desmoplasia in Medulloblastomas—Defining the Nodular/Desmoplastic Variant and Its Biological Behavior*. Brain Pathol, 2007. **17**(2): p. 151-64.
87. Korshunov, A., et al., *Molecular characterization of medulloblastomas with extensive nodularity (MBEN)*. Acta Neuropathol, 2018. **136**(2): p. 303-13.
88. Pietsch, T., et al., *Prognostic significance of clinical, histopathological, and molecular characteristics of medulloblastomas in the prospective HIT2000 multicenter clinical trial cohort*. Acta Neuropathol, 2014. **128**(1): p. 137-49.
89. Giangaspero, F., et al., *Medulloblastoma with extensive nodularity: a variant with favorable prognosis*. J Neurosurg, 1999. **91**(6): p. 971-77.
90. Eberhart, C.G., et al., *Histopathologic grading of medulloblastomas: a Pediatric Oncology Group study*. Cancer, 2002. **94**(2): p. 552-60.
91. Rutkowski, S., et al., *Survival and prognostic factors of early childhood medulloblastoma: an international meta-analysis*. J Clin Oncol, 2010. **28**(33): p. 4961-68.
92. McManamy, C.S., et al., *Morphophenotypic variation predicts clinical behavior in childhood non-desmoplastic medulloblastomas*. J Neuropathol Exp Neurol, 2003. **62**(6): p. 627-32.
93. Louis, D.N., et al., *The 2021 WHO Classification of Tumors of the Central Nervous System: a summary*. Neuro Oncol, 2021. **23**(8): p. 1231-51.
94. Thompson, M.C., et al., *Genomics identifies medulloblastoma subgroups that are enriched for specific genetic alterations*. J Clin Oncol, 2006. **24**(12): p. 1924-31.
95. Kool, M., et al., *Integrated genomics identifies five medulloblastoma subtypes with distinct genetic profiles, pathway signatures and clinicopathological features*. PLoS One, 2008. **3**(8): p. e3088.
96. Cho, Y.J., et al., *Integrative genomic analysis of medulloblastoma identifies a molecular subgroup that drives poor clinical outcome*. J Clin Oncol, 2011. **29**(11): p. 1424-30.
97. Northcott, P.A., et al., *Medulloblastoma comprises four distinct molecular variants*. J Clin Oncol, 2011. **29**(11): p. 1408-14.
98. Taylor, M.D., et al., *Molecular subgroups of medulloblastoma: the current consensus*. Acta Neuropathol, 2012. **123**(4): p. 465-72.

99. Northcott, P.A., et al., *Molecular subgroups of medulloblastoma*. *Expert Rev Neurother*, 2012. **12**(7): p. 871-84.
100. Louis, D.N., et al., *The 2016 World Health Organization Classification of Tumors of the Central Nervous System: a summary*. *Acta Neuropathol*, 2016. **131**(6): p. 803-20.
101. Capper, D., et al., *DNA methylation-based classification of central nervous system tumours*. *Nature*, 2018. **555**(7697): p. 469-74.
102. Schwalbe, E.C., et al., *DNA methylation profiling of medulloblastoma allows robust subclassification and improved outcome prediction using formalin-fixed biopsies*. *Acta Neuropathol*, 2013. **125**(3): p. 359-71.
103. Goschzik, T., et al., *Genetic alterations of TP53 and OTX2 indicate increased risk of relapse in WNT medulloblastomas*. *Acta Neuropathol*, 2022. **144**(6): p. 1143-56.
104. Patay, Z., et al., *MR Imaging Characteristics of Wingless-Type-Subgroup Pediatric Medulloblastoma*. *AJNR Am J Neuroradiol*, 2015. **36**: p. A4495.
105. Gibson, P., et al., *Subtypes of medulloblastoma have distinct developmental origins*. *Nature*, 2010. **468**(7327): p. 1095-99.
106. Northcott, P.A., et al., *The whole-genome landscape of medulloblastoma subtypes*. *Nature*, 2017. **547**(7663): p. 311-17.
107. Liu, J., et al., *Wnt/ β -catenin signalling: function, biological mechanisms, and therapeutic opportunities*. *Signal Transduct Target Ther*, 2022. **7**(1): p. 3.
108. ClinicalTrials.gov. *A Clinical and Molecular Risk-Directed Therapy for Newly Diagnosed Medulloblastoma*. Identifier: NCT01878617, available online: <https://www.clinicaltrials.gov/ct2/show/NCT01878617> [cited 2023 Mar 11th].
109. ClinicalTrials.gov. *Reduced Craniospinal Radiation Therapy and Chemotherapy in Treating Younger Patients With Newly Diagnosed WNT-Driven Medulloblastoma*. Identifier: NCT02724579, available online: <https://clinicaltrials.gov/ct2/show/NCT02724579> [cited 2023 Mar 11th].
110. Perreault, S., et al., *MRI surrogates for molecular subgroups of medulloblastoma*. *AJNR Am J Neuroradiol*, 2014. **35**(7): p. 1263-69.
111. Wefers, A.K., et al., *Subgroup-specific localization of human medulloblastoma based on pre-operative MRI*. *Acta Neuropathol*, 2014. **127**(6): p. 931-33.
112. Waszak, S.M., et al., *Germline Elongator mutations in Sonic Hedgehog medulloblastoma*. *Nature*, 2020. **580**(7803): p. 396-401.
113. Remke, M., et al., *TERT promoter mutations are highly recurrent in SHH subgroup medulloblastoma*. *Acta Neuropathol*, 2013. **126**(6): p. 917-29.
114. Zhukova, N., et al., *Subgroup-Specific Prognostic Implications of TP53 Mutation in Medulloblastoma*. *J Clin Oncol*, 2013. **31**(23): p. 2927-35.
115. Juraschka, K. and M.D. Taylor, *Medulloblastoma in the age of molecular subgroups: a review*. *J Neurosurg Pediatr*, 2019. **24**(4): p. 353-63.

116. Cavalli, F.M.G., et al., *Intertumoral Heterogeneity within Medulloblastoma Subgroups*. *Cancer Cell*, 2017. **31**(6): p. 737-54.
117. Smith, K.S., et al., *Unified rhombic lip origins of group 3 and group 4 medulloblastoma*. *Nature*, 2022. **609**(7929): p. 1012-20.
118. Korshunov, A., et al., *Gene expression profiling of Group 3 medulloblastomas defines a clinically tractable stratification based on KIRREL2 expression*. *Acta Neuropathol*, 2022. **144**(2): p. 339-52.
119. Hendrikse, L.D., et al., *Failure of human rhombic lip differentiation underlies medulloblastoma formation*. *Nature*, 2022. **609**(7929): p. 1021-28.
120. Northcott, P.A., et al., *Enhancer hijacking activates GFI1 family oncogenes in medulloblastoma*. *Nature*, 2014. **511**(7510): p. 428-34.
121. Shih, D.J.H., et al., *Cytogenetic Prognostication Within Medulloblastoma Subgroups*. *J Clin Oncol*, 2014. **32**(9): p. 886-96.
122. Schwalbe, E.C., et al., *Novel molecular subgroups for clinical classification and outcome prediction in childhood medulloblastoma: a cohort study*. *Lancet Oncol*, 2017. **18**(7): p. 958-71.
123. Sharma, T., et al., *Second-generation molecular subgrouping of medulloblastoma: an international meta-analysis of Group 3 and Group 4 subtypes*. *Acta Neuropathol*, 2019. **138**(2): p. 309-26.
124. Luo, W., et al., *Single-cell spatial transcriptomic analysis reveals common and divergent features of developing postnatal granule cerebellar cells and medulloblastoma*. *BMC Biol*, 2021. **19**(1): p. 135.
125. Jones, D.T., et al., *Dissecting the genomic complexity underlying medulloblastoma*. *Nature*, 2012. **488**(7409): p. 100-105.
126. Pugh, T.J., et al., *Medulloblastoma exome sequencing uncovers subtype-specific somatic mutations*. *Nature*, 2012. **488**(7409): p. 106-10.
127. Robinson, G., et al., *Novel mutations target distinct subgroups of medulloblastoma*. *Nature*, 2012. **488**(7409): p. 43-48.
128. Robinson, G.W., et al., *Risk-adapted therapy for young children with medulloblastoma (SJYC07): therapeutic and molecular outcomes from a multicentre, phase 2 trial*. *Lancet Oncol*, 2018. **19**(6): p. 768-84.
129. Morrissy, A.S., et al., *Divergent clonal selection dominates medulloblastoma at recurrence*. *Nature*, 2016. **529**(7586): p. 351-57.
130. Stanton, B.Z., et al., *Smarca4 ATPase mutations disrupt direct eviction of PRC1 from chromatin*. *Nat Genet*, 2017. **49**(2): p. 282-88.
131. Ballabio, C., et al., *Modeling medulloblastoma in vivo and with human cerebellar organoids*. *Nat Commun*, 2020. **11**(1): p. 583.

132. Chen, V.S., et al., *Histology Atlas of the Developing Prenatal and Postnatal Mouse Central Nervous System, with Emphasis on Prenatal Days E7.5 to E18.5*. Toxicol Pathol, 2017. **45**(6): p. 705-44.
133. Meng, W., et al., *Development and Differentiation of Midbrain Dopaminergic Neuron: From Bench to Bedside*. Cells, 2020. **9**: p. 1489.
134. Leto, K., et al., *Consensus Paper: Cerebellar Development*. Cerebellum, 2016. **15**(6): p. 789-828.
135. Martinez, S., et al., *Cellular and molecular basis of cerebellar development*. Front Neuroanat, 2013. **7**: p. 18.
136. van Essen, M.J., et al., *Deconstructing cerebellar development cell by cell*. PLoS Genet, 2020. **16**(4): p. e1008630.
137. Consalez, G.G., et al., *Origins, Development, and Compartmentation of the Granule Cells of the Cerebellum*. Front Neural Circuits, 2020. **14**: p. e611841.
138. Wechsler-Reya, R.J. and M.P. Scott, *Control of neuronal precursor proliferation in the cerebellum by Sonic Hedgehog*. Neuron, 1999. **22**(1): p. 103-14.
139. Cerrato, V., *Cerebellar Astrocytes: Much More Than Passive Bystanders In Ataxia Pathophysiology*. J Clin Med, 2020. **9**(3): p. 757.
140. Araujo, A.P.B., R. Carpi-Santos, and F.C.A. Gomes, *The Role of Astrocytes in the Development of the Cerebellum*. The Cerebellum, 2019. **18**(6): p. 1017-35.
141. Leto, K., C. Rolando, and F. Rossi, *The Genesis of Cerebellar GABAergic Neurons: Fate Potential and Specification Mechanisms*. Front Neuroanat, 2012. **6**: p. 6.
142. Waterston, R.H., et al., *Initial sequencing and comparative analysis of the mouse genome*. Nature, 2002. **420**(6915): p. 520-62.
143. Rosenthal, N. and S. Brown, *The mouse ascending: perspectives for human-disease models*. Nat Cell Biol, 2007. **9**(9): p. 993-99.
144. Sternberg, N. and D. Hamilton, *Bacteriophage P1 site-specific recombination. I. Recombination between loxP sites*. J Mol Biol, 1981. **150**(4): p. 467-86.
145. Sauer, B. and N. Henderson, *Site-specific DNA recombination in mammalian cells by the Cre recombinase of bacteriophage P1*. Proc Natl Acad Sci U S A, 1988. **85**(14): p. 5166-70.
146. Gu, H., Y.R. Zou, and K. Rajewsky, *Independent control of immunoglobulin switch recombination at individual switch regions evidenced through Cre-loxP-mediated gene targeting*. Cell, 1993. **73**(6): p. 1155-64.
147. Lakso, M., et al., *Targeted oncogene activation by site-specific recombination in transgenic mice*. PNAS, 1992. **89**(14): p. 6232-36.
148. Doyle, A., et al., *The construction of transgenic and gene knockout/knockin mouse models of human disease*. Transgenic Res, 2012. **21**(2): p. 327-49.

149. Hegedus, B., et al., *Neurofibromatosis-1 regulates neuronal and glial cell differentiation from neuroglial progenitors in vivo by both cAMP- and Ras-dependent mechanisms*. *Cell Stem Cell*, 2007. **1**(4): p. 443-57.
150. Metzger, D. and P. Chambon, *Site- and time-specific gene targeting in the mouse*. *Methods*, 2001. **24**(1): p. 71-80.
151. Machold, R. and G. Fishell, *Math1 is expressed in temporally discrete pools of cerebellar rhombic-lip neural progenitors*. *Neuron*, 2005. **48**(1): p. 17-24.
152. Soriano, P., *Generalized lacZ expression with the ROSA26 Cre reporter strain*. *Nat Genet*, 1999. **21**(1): p. 70-71.
153. Madisen, L., et al., *A robust and high-throughput Cre reporting and characterization system for the whole mouse brain*. *Nat Neurosci*, 2010. **13**(1): p. 133-40.
154. Harno, E., Elizabeth C. Cottrell, and A. White, *Metabolic Pitfalls of CNS Cre-Based Technology*. *Cell Metabolism*, 2013. **18**(1): p. 21-28.
155. Janbandhu, V.C., D. Moik, and R. Fässler, *Cre recombinase induces DNA damage and tetraploidy in the absence of loxP sites*. *Cell Cycle*, 2014. **13**(3): p. 462-70.
156. Luo, L., et al., *Optimizing Nervous System-Specific Gene Targeting with Cre Driver Lines: Prevalence of Germline Recombination and Influencing Factors*. *Neuron*, 2020. **106**(1): p. 37-65.
157. Heffner, C.S., et al., *Supporting conditional mouse mutagenesis with a comprehensive cre characterization resource*. *Nat Commun*, 2012. **3**(1): p. 1218.
158. Álvarez-Aznar, A., et al., *Tamoxifen-independent recombination of reporter genes limits lineage tracing and mosaic analysis using CreERT2 lines*. *Transgenic Research*, 2020. **29**(1): p. 53-68.
159. Stifter, S.A. and M. Greter, *STOP floxing around: Specificity and leakiness of inducible Cre/loxP systems*. *European Journal of Immunology*, 2020. **50**(3): p. 338-41.
160. Lizen, B., et al., *Perinatal induction of Cre recombination with tamoxifen*. *Transgenic Res*, 2015. **24**(6): p. 1065-77.
161. Doetschman, T., *Influence of genetic background on genetically engineered mouse phenotypes*. *Methods Mol Biol*, 2009. **530**: p. 423-33.
162. Tanabe, L.M., C. Martin, and W.T. Dauer, *Genetic Background Modulates the Phenotype of a Mouse Model of DYT1 Dystonia*. *PLOS ONE*, 2012. **7**(2): p. e32245.
163. Bultman, S., et al., *A Brg1 null mutation in the mouse reveals functional differences among mammalian SWI/SNF complexes*. *Mol Cell*, 2000. **6**(6): p. 1287-95.
164. Matsumoto, S., et al., *Brg1 is required for murine neural stem cell maintenance and gliogenesis*. *Dev Biol*, 2006. **289**(2): p. 372-83.
165. Holdhof, D., et al., *hGFAP-Positive Stem Cells Depend on Brg1 for Proper Formation of Cerebral and Cerebellar Structures*. *Cereb Cortex*, 2020. **30**(3): p. 1382-92.

166. Reyes, J.C., et al., *Altered control of cellular proliferation in the absence of mammalian brahma (SNF2alpha)*. EMBO J, 1998. **17**(23): p. 6979-91.
167. Moreno, N., et al., *Loss of Smarc proteins impairs cerebellar development*. J Neurosci, 2014. **34**(40): p. 13486-91.
168. Holdhof, D., et al., *Simultaneous Brg1 Knockout and MYCN Overexpression in Cerebellar Granule Neuron Precursors Is Insufficient to Drive Tumor Formation but Temporarily Enhances their Proliferation and Delays their Migration*. Cerebellum, 2021. **20**(3): p. 410-19.
169. Holdhof, D., et al., *Brahma-related gene 1 has time-specific roles during brain and eye development*. Development, 2021. **148**(10): p. e196147.
170. Neyazi, S., et al., *Generation of new transgenic SMARCA4-deficient mouse models results in neuromuscular weakness and paralysis of limbs*. Brain Pathol. **n/a**(n/a): p. e13146.
171. Bultman, S.J., et al., *Characterization of mammary tumors from Brg1 heterozygous mice*. Oncogene, 2008. **27**(4): p. 460-68.
172. Glaros, S., et al., *Targeted Knockout of BRG1 Potentiates Lung Cancer Development*. Cancer Res, 2008. **68**(10): p. 3689-96.
173. Gajjar, A. and J.L. Finlay, *The management of children and adolescents with medulloblastoma in low and middle income countries*. Pediatr Blood Cancer, 2015. **62**(4): p. 549-50.
174. Swartling, F.J., et al., *Pleiotropic role for MYCN in medulloblastoma*. Genes Dev, 2010. **24**(10): p. 1059-72.
175. Roussel, M.F. and J.L. Stripay, *Modeling pediatric medulloblastoma*. Brain Pathol, 2020. **30**(3): p. 703-12.
176. Kawauchi, D., et al., *A mouse model of the most aggressive subgroup of human medulloblastoma*. Cancer Cell, 2012. **21**(2): p. 168-80.
177. Kawauchi, D., et al., *Novel MYC-driven medulloblastoma models from multiple embryonic cerebellar cells*. Oncogene, 2017. **36**(37): p. 5231-42.
178. Tao, R., et al., *MYC Drives Group 3 Medulloblastoma through Transformation of Sox2(+) Astrocyte Progenitor Cells*. Cancer Res, 2019. **79**(8): p. 1967-80.
179. Mainwaring, O.J., et al., *ARF suppression by MYC but not MYCN confers increased malignancy of aggressive pediatric brain tumors*. Nat Commun, 2023. **14**(1): p. 1221.
180. Dhar, S.S., et al., *MLL4 Is Required to Maintain Broad H3K4me3 Peaks and Super-Enhancers at Tumor Suppressor Genes*. Mol Cell, 2018. **70**(5): p. 825-41
181. Beckmann, P.J., et al., *Sleeping Beauty Insertional Mutagenesis Reveals Important Genetic Drivers of Central Nervous System Embryonal Tumors*. Cancer Res, 2019. **79**(5): p. 905-17.
182. Pan, J., et al., *The ATPase module of mammalian SWI/SNF family complexes mediates subcomplex identity and catalytic activity-independent genomic targeting*. Nat Genet, 2019. **51**(4): p. 618-26.

183. Ye, J., et al., *Primer-BLAST: a tool to design target-specific primers for polymerase chain reaction*. BMC Bioinformatics, 2012. **13**: p. 134.
184. Pantelouris, E.M., *Absence of thymus in a mouse mutant*. Nature, 1968. **217**(5126): p. 370-71.
185. Harada, N., et al., *Intestinal polyposis in mice with a dominant stable mutation of the beta-catenin gene*. EMBO J, 1999. **18**(21): p. 5931-42.
186. Luche, H., et al., *Faithful activation of an extra-bright red fluorescent protein in "knock-in" Cre-reporter mice ideally suited for lineage tracing studies*. Eur J Immunol, 2007. **37**(1): p. 43-53.
187. Indra, A.K., et al., *Temporally controlled targeted somatic mutagenesis in embryonic surface ectoderm and fetal epidermal keratinocytes unveils two distinct developmental functions of BRG1 in limb morphogenesis and skin barrier formation*. Development, 2005. **132**(20): p. 4533-44.
188. Sumi-Ichinose, C., et al., *SNF2beta-BRG1 is essential for the viability of F9 murine embryonal carcinoma cells*. Mol Cell Biol, 1997. **17**(10): p. 5976-86.
189. Truett, G.E., et al., *Preparation of PCR-quality mouse genomic DNA with hot sodium hydroxide and tris (HotSHOT)*. Biotechniques, 2000. **29**(1): p. 52-54.
190. Otte, A., et al., *A tumor-derived population (SCCOHT-1) as cellular model for a small cell ovarian carcinoma of the hypercalcemic type*. Int J Oncol, 2012. **41**(2): p. 765-75.
191. Miller, M.W. and R.S. Nowakowski, *Use of bromodeoxyuridine-immunohistochemistry to examine the proliferation, migration and time of origin of cells in the central nervous system*. Brain Res, 1988. **457**(1): p. 44-52.
192. Aryee, M.J., et al., *Minfi: a flexible and comprehensive Bioconductor package for the analysis of Infinium DNA methylation microarrays*. Bioinformatics, 2014. **30**(10): p. 1363-1369.
193. Zhou, W., et al., *SeSAME: reducing artifactual detection of DNA methylation by Infinium BeadChips in genomic deletions*. Nucleic Acids Research, 2018. **46**(20): p. e123.
194. McInnes, L., et al., *UMAP: Uniform Manifold Approximation and Projection*. J Open Source Softw, 2018. **3**(29): p. e861.
195. Gu, Z., R. Eils, and M. Schlesner, *Complex heatmaps reveal patterns and correlations in multidimensional genomic data*. Bioinformatics, 2016. **32**(18): p. 2847-49.
196. Ren, X. and P.F. Kuan, *methylGSA: a Bioconductor package and Shiny app for DNA methylation data length bias adjustment in gene set testing*. Bioinformatics, 2019. **35**(11): p. 1958-59.
197. Supek, F., et al., *REVIGO Summarizes and Visualizes Long Lists of Gene Ontology Terms*. PLOS ONE, 2011. **6**(7): p. e21800.
198. Afgan, E., et al., *The Galaxy platform for accessible, reproducible and collaborative biomedical analyses: 2018 update*. Nucleic Acids Res, 2018. **46**(W1): p. 537-44.

199. Sturm, D., et al., *New Brain Tumor Entities Emerge from Molecular Classification of CNS-PNETs*. Cell, 2016. **164**(5): p. 1060-72.
200. Ritchie, M.E., et al., *limma powers differential expression analyses for RNA-sequencing and microarray studies*. Nucleic Acids Res, 2015. **43**(7): p. e47.
201. Zheng, G.X.Y., et al., *Massively parallel digital transcriptional profiling of single cells*. Nature Communications, 2017. **8**(1): p. 14049.
202. Hao, Y., et al., *Integrated analysis of multimodal single-cell data*. Cell, 2021. **184**(13): p. 3573-87.
203. Stuart, T., et al., *Comprehensive Integration of Single-Cell Data*. Cell, 2019. **177**(7): p. 1888-1902.e21.
204. La Manno, G., et al., *Molecular architecture of the developing mouse brain*. Nature, 2021. **596**(7870): p. 92-96.
205. Karnezis, A.N., et al., *Dual loss of the SWI/SNF complex ATPases SMARCA4/BRG1 and SMARCA2/BRM is highly sensitive and specific for small cell carcinoma of the ovary, hypercalcaemic type*. J Pathol, 2016. **238**(3): p. 389-400.
206. Pei, Y., et al., *An animal model of MYC-driven medulloblastoma*. Cancer Cell, 2012. **21**(2): p. 155-67.
207. Vo, B.T., et al., *Inactivation of Ezh2 Upregulates Gfi1 and Drives Aggressive Myc-Driven Group 3 Medulloblastoma*. Cell Rep, 2017. **18**(12): p. 2907-2917.
208. Grotzer, M.A., A. Neve, and M. Baumgartner, *Dissecting brain tumor growth and metastasis in vitro and ex vivo*. J Cancer Metastasis Treat, 2016. **2**: p. 149-62.
209. Schüller, U., et al., *Acquisition of granule neuron precursor identity is a critical determinant of progenitor cell competence to form Shh-induced medulloblastoma*. Cancer Cell, 2008. **14**(2): p. 123-34.
210. van Riggelen, J., A. Yetil, and D.W. Felsher, *MYC as a regulator of ribosome biogenesis and protein synthesis*. Nat Rev Cancer, 2010. **10**(4): p. 301-09.
211. Pöschl, J., et al., *Expression of BARHL1 in medulloblastoma is associated with prolonged survival in mice and humans*. Oncogene, 2011. **30**(47): p. 4721-30.
212. Cimino, P.J., et al., *Increased HOXA5 expression provides a selective advantage for gain of whole chromosome 7 in IDH wild-type glioblastoma*. Genes Dev, 2018. **32**(7-8): p. 512-23.
213. He, Z.C., et al., *HOXA5 is amplified in glioblastoma stem cells and promotes tumor progression by transcriptionally activating PTPRZ1*. Cancer Lett, 2022. **533**: p. e215605.
214. Wilson, P.G. and S.S. Stice, *Development and differentiation of neural rosettes derived from human embryonic stem cells*. Stem Cell Rev, 2006. **2**(1): p. 67-77.
215. Pardridge, W.M., R.J. Boado, and C.R. Farrell, *Brain-type glucose transporter (GLUT-1) is selectively localized to the blood-brain barrier. Studies with quantitative western blotting and in situ hybridization*. J Biol Chem, 1990. **265**(29): p. 18035-40.

216. Dermietzel, R., et al., *Pattern of glucose transporter (Glut 1) expression in embryonic brains is related to maturation of blood-brain barrier tightness*. Dev Dyn, 1992. **193**(2): p. 152-63.
217. Phoenix, T.N., et al., *Medulloblastoma Genotype Dictates Blood Brain Barrier Phenotype*. Cancer Cell, 2016. **29**(4): p. 508-22.
218. Seto, Y., et al., *Temporal identity transition from Purkinje cell progenitors to GABAergic interneuron progenitors in the cerebellum*. Nat Commun, 2014. **5**: p. 3337.
219. Latour, M., et al., *WNT Signaling as a Therapeutic Target for Glioblastoma*. Int J Mol Sci, 2021. **22**(16): p. e8428.
220. Zhang, N., et al., *FoxM1 promotes β -catenin nuclear localization and controls Wnt target-gene expression and glioma tumorigenesis*. Cancer Cell, 2011. **20**(4): p. 427-42.
221. Dykhuizen, E.C., et al., *BAF complexes facilitate decatenation of DNA by topoisomerase IIa*. Nature, 2013. **497**(7451): p. 624-27.
222. Bigner, S.H., et al., *Amplification of the c-myc Gene in Human Medulloblastoma Cell Lines and Xenografts1*. Cancer Res, 1990. **50**(8): p. 2347-50.
223. Di, C., et al., *Identification of OTX2 as a medulloblastoma oncogene whose product can be targeted by all-trans retinoic acid*. Cancer Res, 2005. **65**(3): p. 919-24.
224. Nath, D., et al., *Abi1 loss drives prostate tumorigenesis through activation of EMT and non-canonical WNT signaling*. Cell Commun Signal, 2019. **17**(1): p. 120.
225. Lochhead, P.A., et al., *Activating ROCK1 somatic mutations in human cancer*. Oncogene, 2010. **29**(17): p. 2591-98.
226. van Horssen, R., et al., *E-cadherin promotor methylation and mutation are inversely related to motility capacity of breast cancer cells*. Breast Cancer Res Treat, 2012. **136**(2): p. 365-77.
227. Liang, C.-C., A.Y. Park, and J.-L. Guan, *In vitro scratch assay: a convenient and inexpensive method for analysis of cell migration in vitro*. Nature Protocols, 2007. **2**(2): p. 329-33.
228. Justus, C.R., et al., *In vitro cell migration and invasion assays*. J Vis Exp, 2014(88): p. e51046.
229. Othman, R.T., et al., *Overcoming multiple drug resistance mechanisms in medulloblastoma*. Acta Neuropathol Commun, 2014. **2**: p. 57.
230. Manoranjan, B., et al., *Wnt activation as a therapeutic strategy in medulloblastoma*. Nat Commun, 2020. **11**(1): p. 4323.
231. Zhan, X., et al., *Dual role of Brg chromatin remodeling factor in Sonic hedgehog signaling during neural development*. PNAS, 2011. **108**(31): p. 12758-63.
232. UniProt. *Protein sequence of human SMARCA4*. Entry: P51532 (SMCA4_HUMAN), available online: <https://www.uniprot.org/uniprotkb/P51532/entry> [cited 2023 Apr 27th].
233. UniProt. *Protein sequence of murine SMARCA4*. Entry: Q3TKT4 (SMCA4_MOUSE), available online: <https://www.uniprot.org/uniprotkb/Q3TKT4/entry> [cited 2023 Apr 27th].

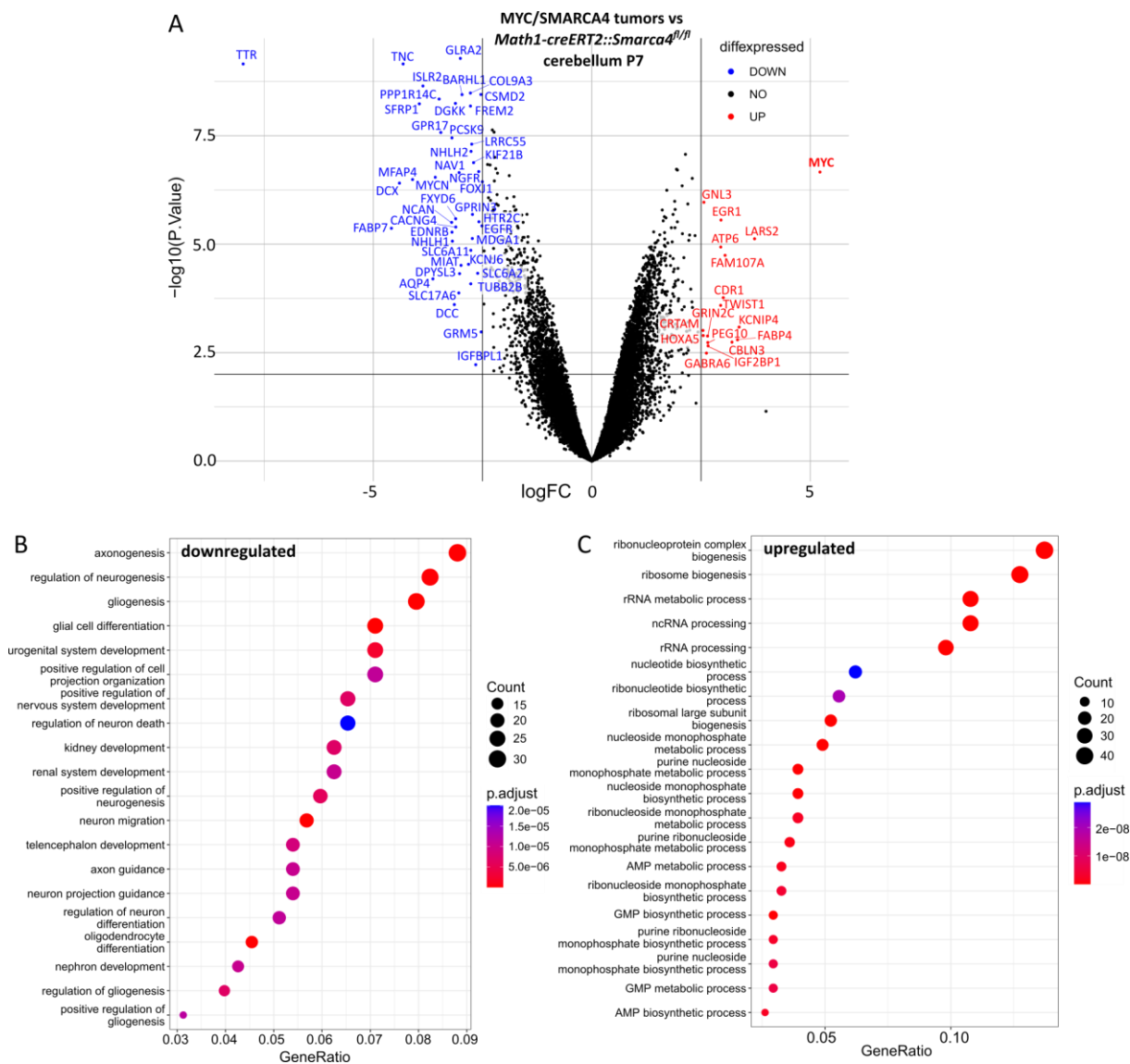
234. Swartling, Fredrik J., et al., *Distinct Neural Stem Cell Populations Give Rise to Disparate Brain Tumors in Response to N-MYC*. *Cancer Cell*, 2012. **21**(5): p. 601-13.
235. McMahon, S.B., *MYC and the control of apoptosis*. *Cold Spring Harb Perspect Med*, 2014. **4**(7): p. e014407.
236. Murphy, D.J., et al., *Distinct thresholds govern Myc's biological output in vivo*. *Cancer Cell*, 2008. **14**(6): p. 447-57.
237. Boulanger, J.J., et al., *A simple histological technique to improve immunostaining when using DNA denaturation for BrdU labelling*. *J Neurosci Methods*, 2016. **259**: p. 40-46.
238. Salic, A. and T.J. Mitchison, *A chemical method for fast and sensitive detection of DNA synthesis in vivo*. *PNAS*, 2008. **105**(7): p. 2415-20.
239. Vo, B.T., et al., *Mouse medulloblastoma driven by CRISPR activation of cellular Myc*. *Sci Rep*, 2018. **8**(1): p. 8733.
240. Shultz, L.D., et al., *Human lymphoid and myeloid cell development in NOD/LtSz-scid IL2R gamma null mice engrafted with mobilized human hemopoietic stem cells*. *J Immunol*, 2005. **174**(10): p. 6477-89.
241. Ayrault, O., et al., *Atoh1 inhibits neuronal differentiation and collaborates with Gli1 to generate medulloblastoma-initiating cells*. *Cancer Res*, 2010. **70**(13): p. 5618-27.
242. Pöschl, J., et al., *Constitutive activation of β -catenin in neural progenitors results in disrupted proliferation and migration of neurons within the central nervous system*. *Dev Biol*, 2013. **374**(2): p. 319-32.
243. Stevens, J.C., et al., *Quiet mutations in inbred strains of mice*. *Trends Mol Med*, 2007. **13**(12): p. 512-19.
244. Mahajan, V.S., et al., *Striking Immune Phenotypes in Gene-Targeted Mice Are Driven by a Copy-Number Variant Originating from a Commercially Available C57BL/6 Strain*. *Cell Rep*, 2016. **15**(9): p. 1901-09.
245. Benavides, F., et al., *Genetic quality assurance and genetic monitoring of laboratory mice and rats: FELASA Working Group Report*. *Lab Anim*, 2020. **54**(2): p. 135-48.
246. Zhang, T., et al., *Generation of excitatory and inhibitory neurons from common progenitors via Notch signaling in the cerebellum*. *Cell Reports*, 2021. **35**(10): p. e109208.
247. Requardt, R.P., et al., *Quality control of astrocyte-directed Cre transgenic mice: The benefits of a direct link between loss of gene expression and reporter activation*. *Glia*, 2009. **57**(6): p. 680-92.
248. Liu, J., et al., *Non-parallel recombination limits Cre-LoxP-based reporters as precise indicators of conditional genetic manipulation*. *Genesis*, 2013. **51**(6): p. 436-42.
249. Jessa, S., et al., *Stalled developmental programs at the root of pediatric brain tumors*. *Nat Genet*, 2019. **51**(12): p. 1702-13.
250. Mosimann, C., G. Hausmann, and K. Basler, *β -Catenin hits chromatin: regulation of Wnt target gene activation*. *Nat Rev Mol Cell Biol*, 2009. **10**(4): p. 276-86.

251. Eberhart, C.G., T. Tihan, and P.C. Burger, *Nuclear Localization and Mutation of β -Catenin in Medulloblastomas*. *J Neuropathol Exp Neurol*, 2000. **59**(4): p. 333-37.
252. Lee, C.I., et al., *CTNNB1 (beta-catenin) mutation is rare in brain tumours but involved as a sporadic event in a brain metastasis*. *Acta Neurochir (Wien)*, 2009. **151**(9): p. 1107-11.
253. He, J., et al., *Characterization of novel CTNNB1 mutation in Craniopharyngioma by whole-genome sequencing*. *Molecular Cancer*, 2021. **20**(1): p. 168.
254. Hall, A., *The cytoskeleton and cancer*. *Cancer Metastasis Rev*, 2009. **28**(1-2): p. 5-14.
255. Nürnberg, A., T. Kitzing, and R. Grosse, *Nucleating actin for invasion*. *Nat Rev Cancer*, 2011. **11**(3): p. 177-87.
256. Delbridge, A.R.D., et al., *Organotypic Brain Slice Culture Microglia Exhibit Molecular Similarity to Acutely-Isolated Adult Microglia and Provide a Platform to Study Neuroinflammation*. *Front Cell Neurosci*, 2020. **14**: p. e592005.
257. Gilthorpe, J.D., et al., *The migration of cerebellar rhombic lip derivatives*. *Development*, 2002. **129**(20): p. 4719-28.
258. Olivetti, P.R., C.O. Lacefield, and C. Kellendonk, *A device for stereotaxic viral delivery into the brains of neonatal mice*. *Biotechniques*, 2020. **69**(4): p. 307-12.
259. Ho, H., et al., *An inhalation anaesthesia approach for neonatal mice allowing streamlined stereotactic injection in the brain*. *J Neurosci Methods*, 2020. **342**: p. e108824.
260. Morcavallo, A., et al., *MODL-02. A novel Cre-conditional cMYC-driven MB Group 3 transgenic mouse model shows traceable leptomeningeal dissemination*. *Neuro Oncol*, 2022. **24**(Supplement_1): p. 168.
261. Li, X.N., et al., *Valproic acid induces growth arrest, apoptosis, and senescence in medulloblastomas by increasing histone hyperacetylation and regulating expression of p21Cip1, CDK4, and CMYC*. *Mol Cancer Ther*, 2005. **4**(12): p. 1912-22.
262. Pei, Y., et al., *HDAC and PI3K Antagonists Cooperate to Inhibit Growth of MYC-Driven Medulloblastoma*. *Cancer Cell*, 2016. **29**(3): p. 311-23.
263. Ecker, J., et al., *Targeting class I histone deacetylase 2 in MYC amplified group 3 medulloblastoma*. *Acta Neuropathol Commun*, 2015. **3**: p. 22.
264. Bergen, V., et al., *RNA velocity—current challenges and future perspectives*. *Mol Syst Biol*, 2021. **17**(8): p. e10282.
265. Lowenstein, E.D., et al., *Olig3 regulates early cerebellar development*. *Elife*, 2021. **10**: p. e64684.
266. Hill, R.M., et al., *Combined MYC and P53 defects emerge at medulloblastoma relapse and define rapidly progressive, therapeutically targetable disease*. *Cancer Cell*, 2015. **27**(1): p. 72-84.
267. Jenkins, N.C., et al., *Somatic cell transfer of c-Myc and Bcl-2 induces large-cell anaplastic medulloblastomas in mice*. *J Neurooncol*, 2016. **126**(3): p. 415-24.

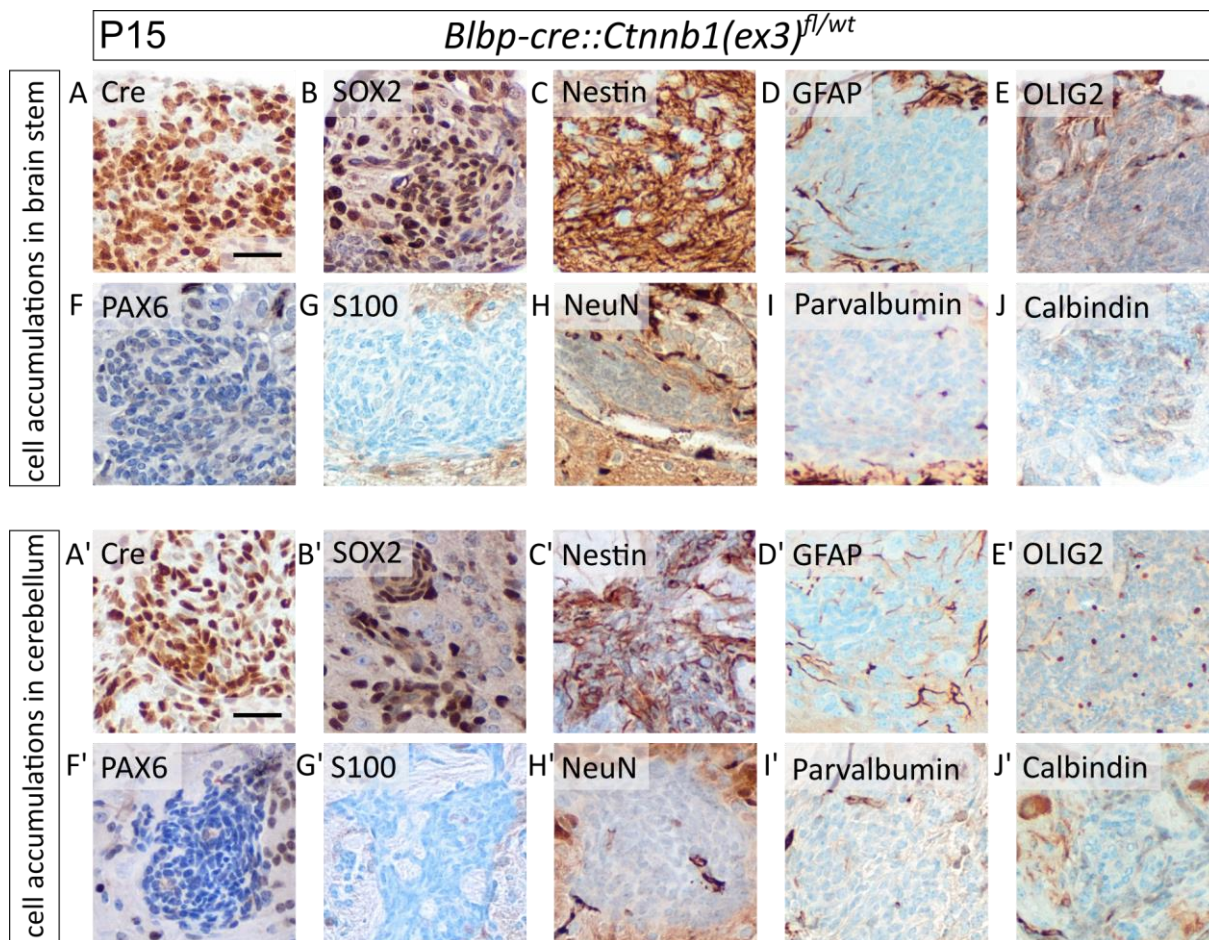
-
268. Lee, C., et al., *Lsd1 as a therapeutic target in Gfi1-activated medulloblastoma*. Nat Commun, 2019. **10**(1): p. 332.
269. Ballabio, C., et al., *Notch1 switches progenitor competence in inducing medulloblastoma*. Sci Adv, 2021. **7**(26): p. 2781.

8 APPENDIX

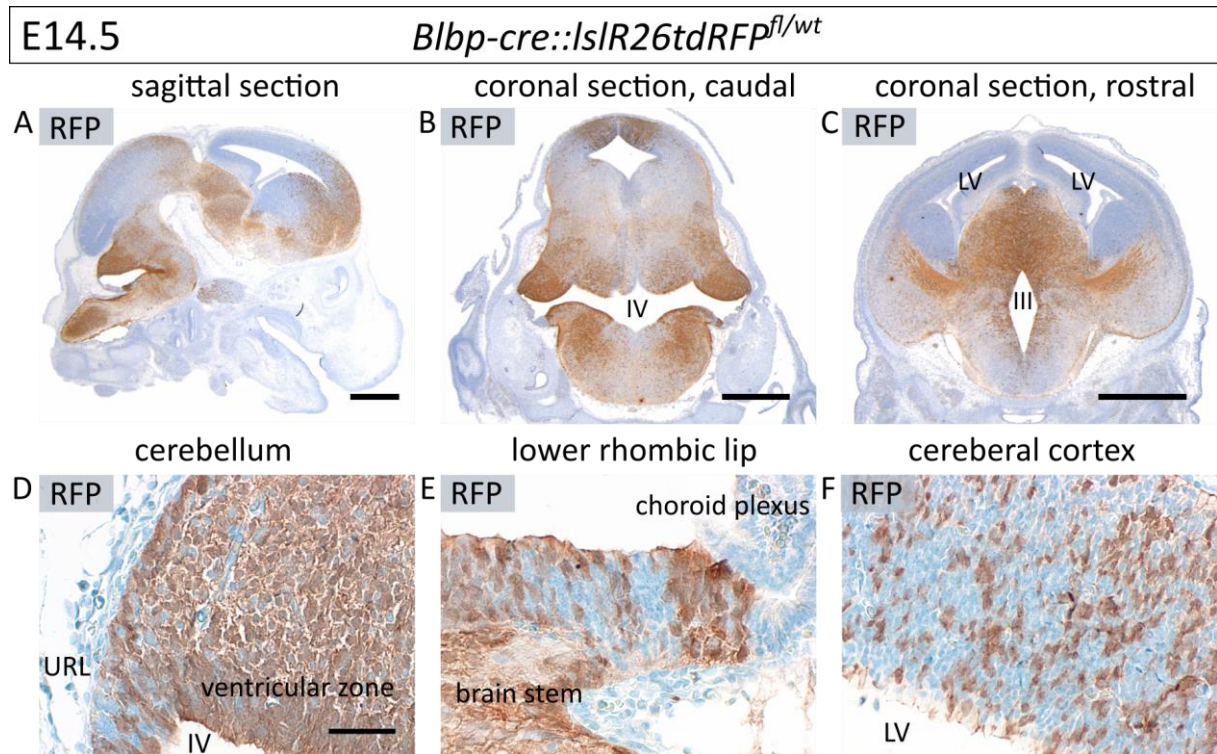
8.1 Supplementary Figures



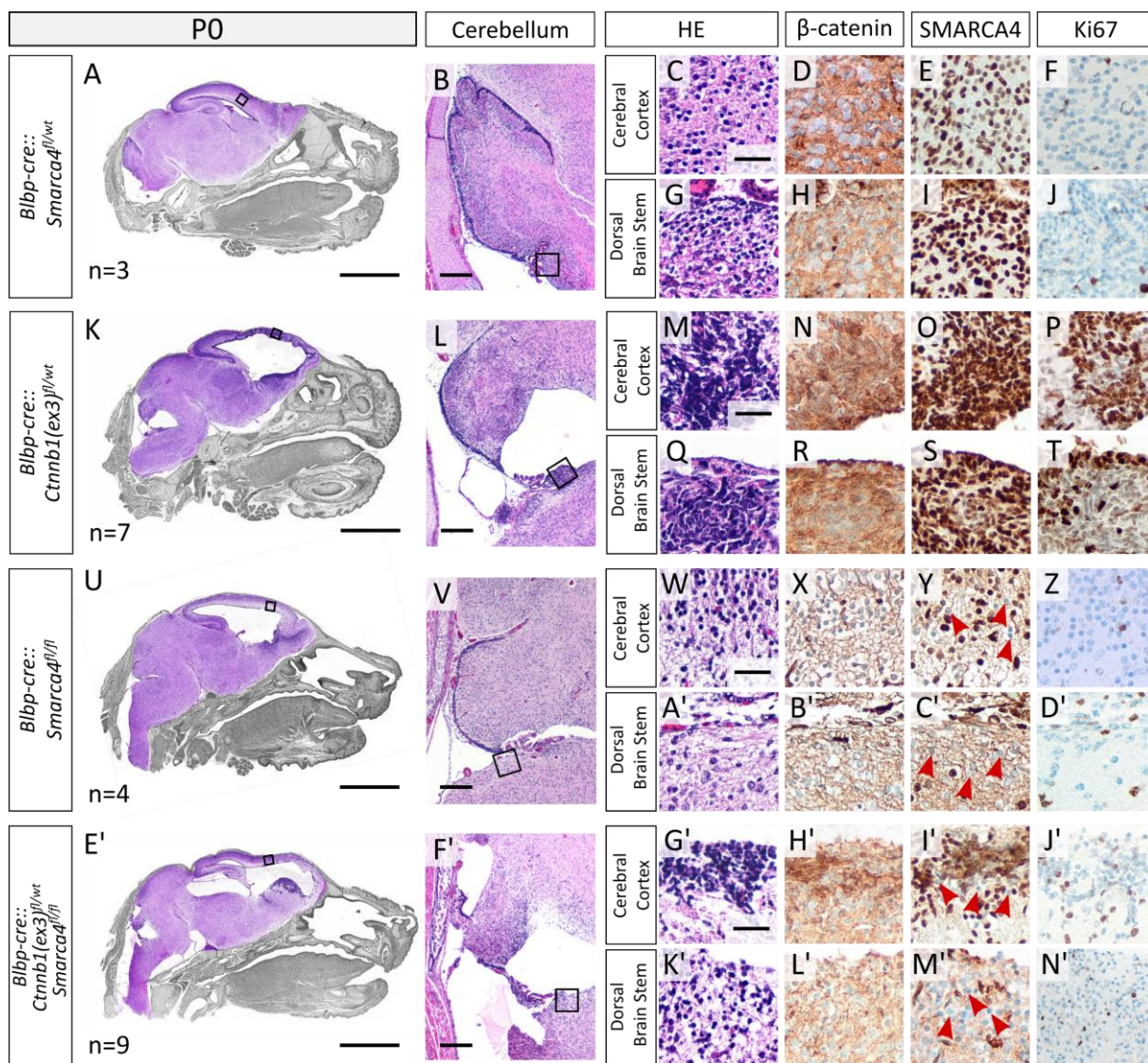
Supplementary Figure 1. Differential gene expression of MYC/SMARCA4 tumors compared to *Math1-creERT2::Smarca4^{fl/fl}* cerebella at P7. (A) Volcano plot depicting differential gene expression as assessed by RNA sequencing analysis between our MYC/SMARCA4 tumor model ($n=4$) and P7 *Math1-creERT2::Smarca4^{fl/fl}* cerebella after tamoxifen injection at P3 ($n=3$), recapitulating the cellular origin of our tumors. Only genes orthologous in mouse and humans were visualized, and differential expression with $\log_{2}FC \geq 2.5$ and $p \leq 0.01$ was considered significant (blue/red coloring) after Benjamini-Hochberg correction. (B,C) Gene set enrichment analysis was performed based on significantly differentially expressed genes considering all mouse genes with $\log_{2}FC \geq 1.5$ and $p \leq 0.01$. Count = count of significantly deregulated genes; GeneRatio = count/size of gene set; p.adjust = adjusted p-value.



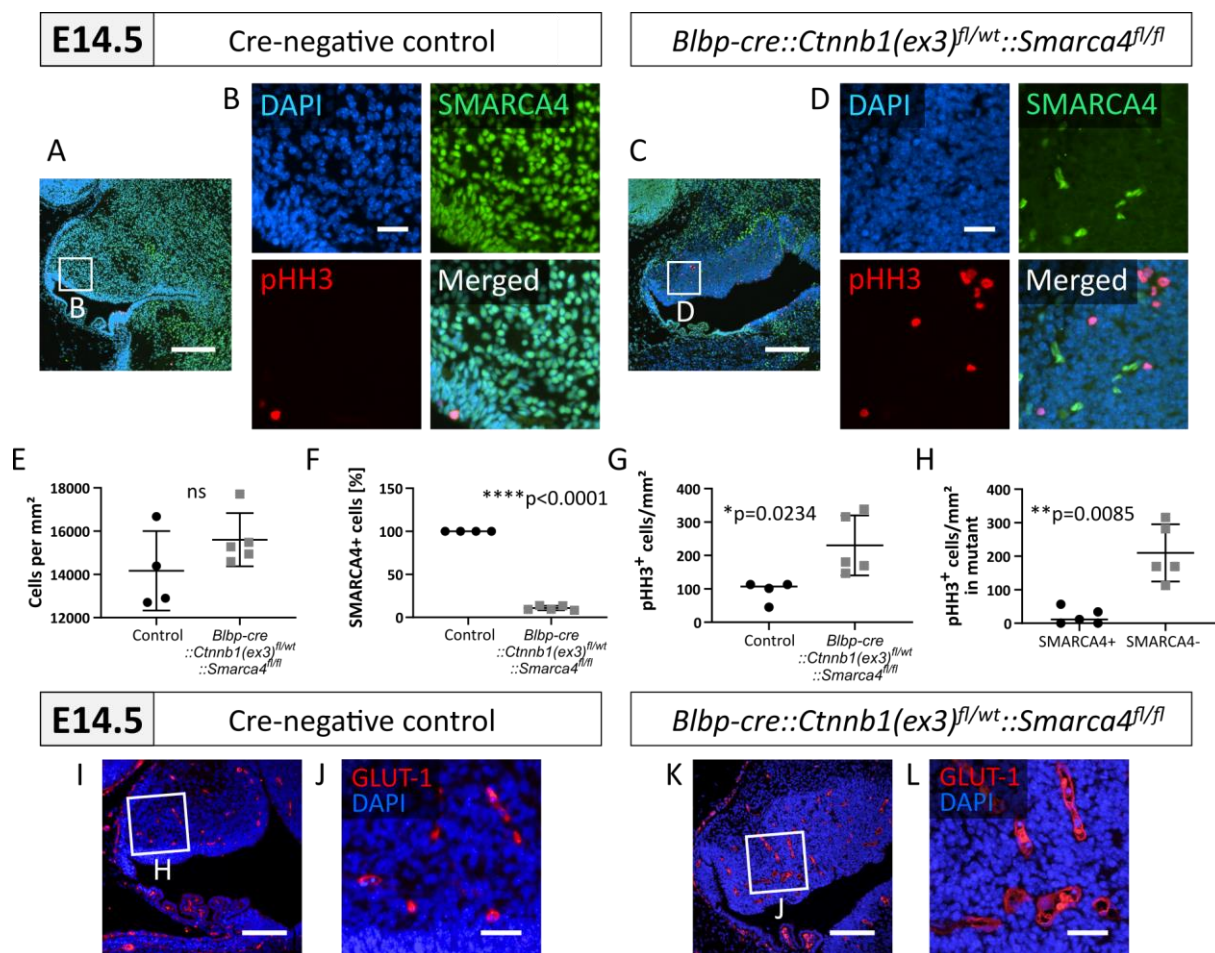
Supplementary Figure 2. Histological characterization of cell accumulations in the cerebellum and brain stem of *Blbp-cre::Ctnnb1(ex3)^{fl/wt}* mutants. Cell accumulations in both locations at P15 display similar immunohistochemistry, staining positive for cre (A+A'), SOX2 (B+B'), and Nestin (C+C') with sparse to no expression of GFAP (D+D') and OLIG2 (E+E'), and negativity for PAX6 (F+F'), S100 (G+G'), NeuN (H+H'), parvalbumin (I+I'), and calbindin (J+J'). Scale bars in A+A' correspond to 50 μ m and are applicable to all other panels.



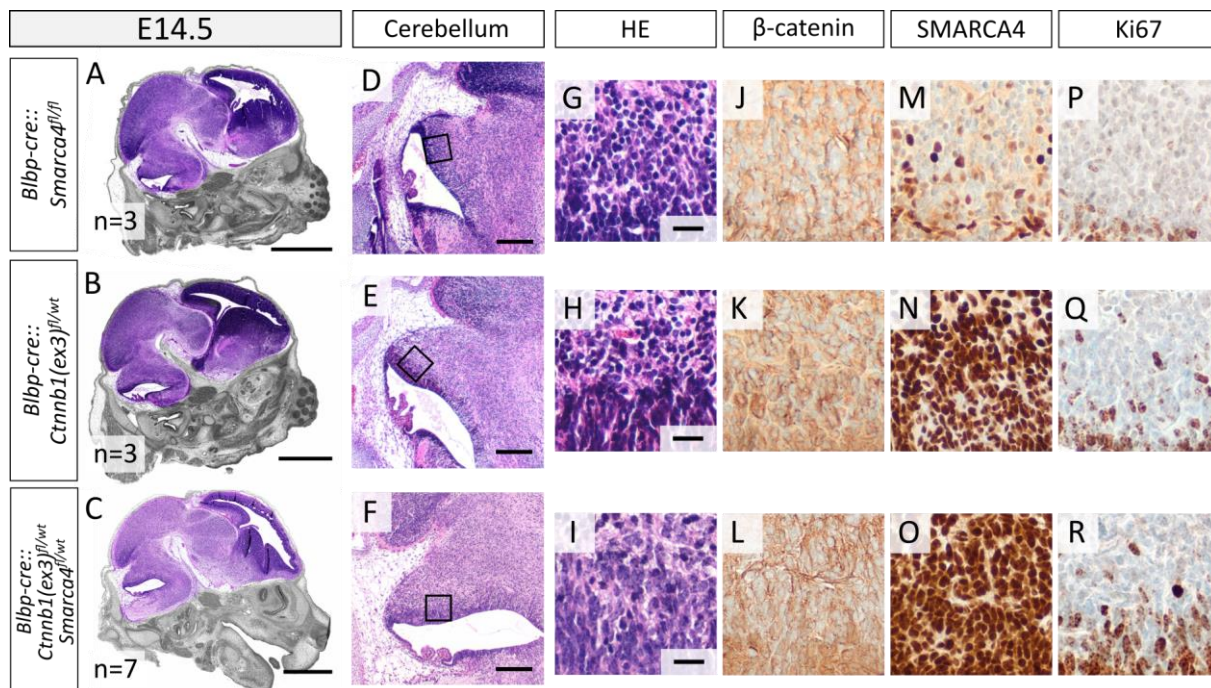
Supplementary Figure 3. Fate mapping mice show broad recombination by *Blbp-cre* throughout the embryonic brain. (A) RFP staining in *Blbp-cre::IslR26tdRFP^{fl/wt}* embryos at E14.5 (sagittal section of whole head) reveals recombination in the cerebellum, midbrain, and cortex, which was also verified in coronal sections (B+C). High power images show positive stainings throughout the whole cerebellum (D), no signal in the choroid plexus (E), and scattered expression in the dorsal brain stem (E) and rostral part of the cerebral cortex (F). Scale bars in A, B and C correspond to 500 μ m, scale bar in D corresponds to 50 μ m and is applicable to E and F. LV = lateral ventricle, III = third ventricle, IV = fourth ventricle, URL = upper rhombic lip.



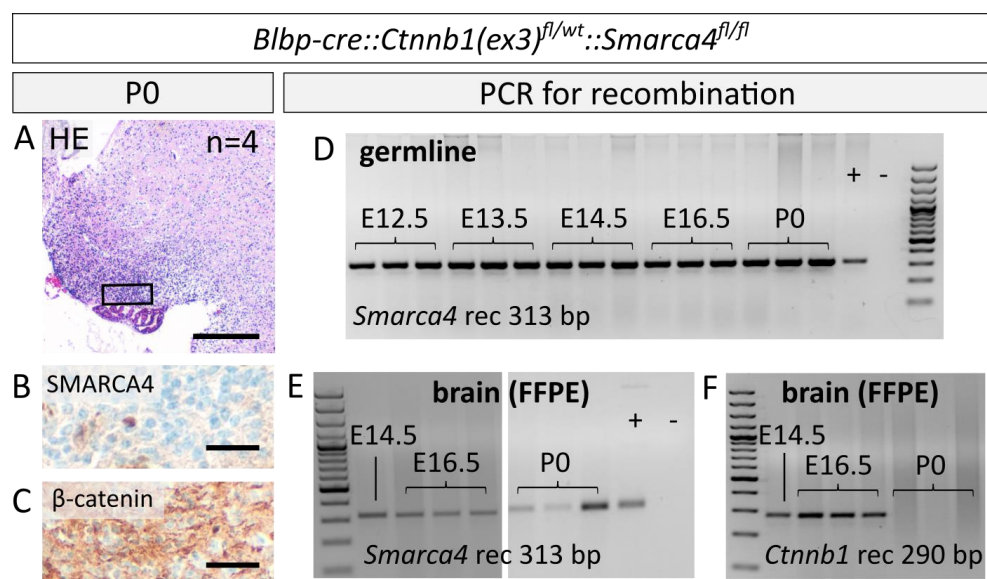
Supplementary Figure 4. Severe developmental phenotypes but no tumor development in mutants at P0. (A) HE staining of sagittal section of the whole head (brain in color) of *Blbp-cre::Smarca4^{fl/wt}* mice at P0 reveals no phenotype. (B-J) High power images show normally developing cerebellum, cortex, and dorsal brain stem. Cerebral cortex region is indicated by the black rectangle in A, while the dorsal brain stem region is indicated by the black rectangle in B. (K-T) *Blbp-cre::Ctnnb1(ex3)^{fl/wt}* mutants already display severe hydrocephalus, hypoplastic cerebella, and aberrant cell accumulations in both cerebral cortex and dorsal brain stem with nuclear accumulation of β -catenin at P0. *Blbp-cre::Ctnnb1(ex3)^{fl/wt}::Smarca4^{fl/wt}* mutants showed the exact same phenotype and are therefore not displayed (n=11 analyzed). (U-D') *Blbp-cre::Smarca4^{fl/fl}* mutants also show hydrocephalus and hypoplastic cerebella but no cell accumulations in both cortex and brain stem. Partial SMARCA4 loss is visible in both regions, examples marked by red arrowheads (Y, C'). (E'-N') *Blbp-cre::Ctnnb1(ex3)^{fl/wt}::Smarca4^{fl/fl}* mutants were mostly found dead at birth and showed severe hydrocephalus and the most prominent hypoplastic cerebella. Aberrant cell accumulations in the cerebral cortex were detected in reduced quantity and size, whereas cell accumulations in the dorsal brain stem were never found. Scale bars in A, K, U, E' correspond to 2 mm, in B, L, V, F' to 200 μ m and in C, M, W, G' to 50 μ m (applicable to all remaining panels).



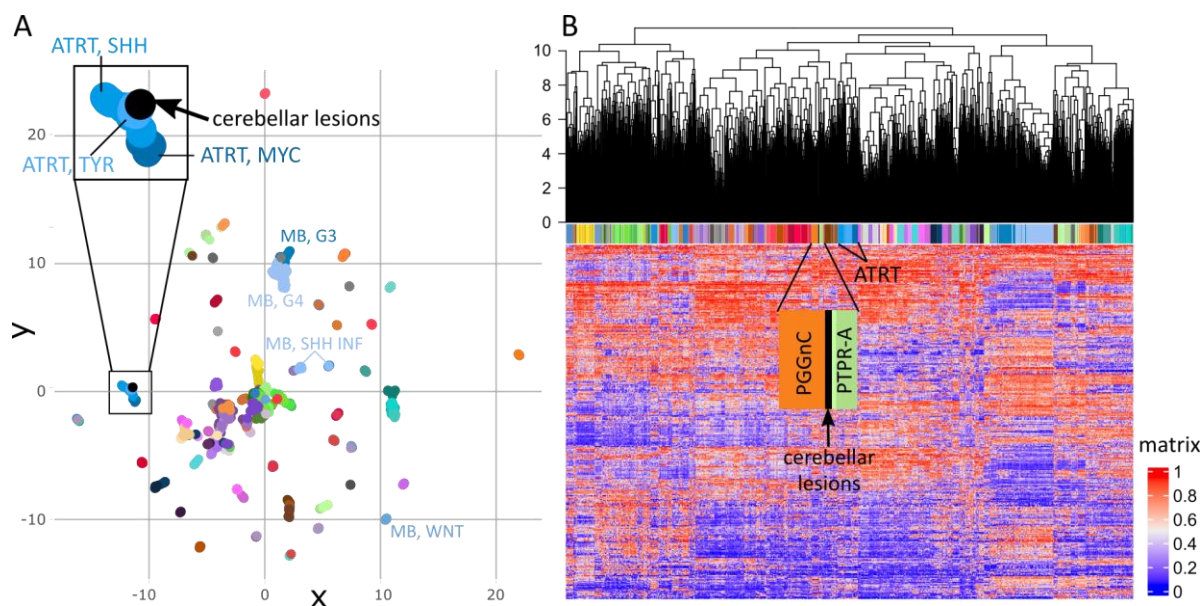
Supplementary Figure 5. Cerebellar lesions in *Blbp-cre::Ctnnb1(ex3)^{fl/wt}::Smarca4^{fl/fl}* mutants show increased mitotic count but no loss of blood brain barrier. (A-D) IF staining of SMARCA4 and pHH3 in the ventricular zone of controls and mutants (*Blbp-cre::Ctnnb1(ex3)^{fl/wt}::Smarca4^{fl/fl}*) reveals a loss of SMARCA4 and increased mitotic count in mutants. (E-H) While cell density is not significantly increased in mutants (E), SMARCA4 knockdown is visible in around 90% of cells (F), and mitotic cell count is significantly increased in mutants (G) with significantly more SMARCA4-negative mitotic cells than SMARCA4-positive mitotic cells (H). Welch's t-tests were applied in E and G, one sample t-test was applied in F, and paired t-test was applied in H. (I-L) Blood vessels in controls as well as mutants show positivity for GLUT-1, suggesting a maintained blood-brain barrier within the lesion. Scale bars in A+C correspond to 200 μ m, in B+D to 25 μ m, in G+I to 100 μ m, and in H+J to 25 μ m.



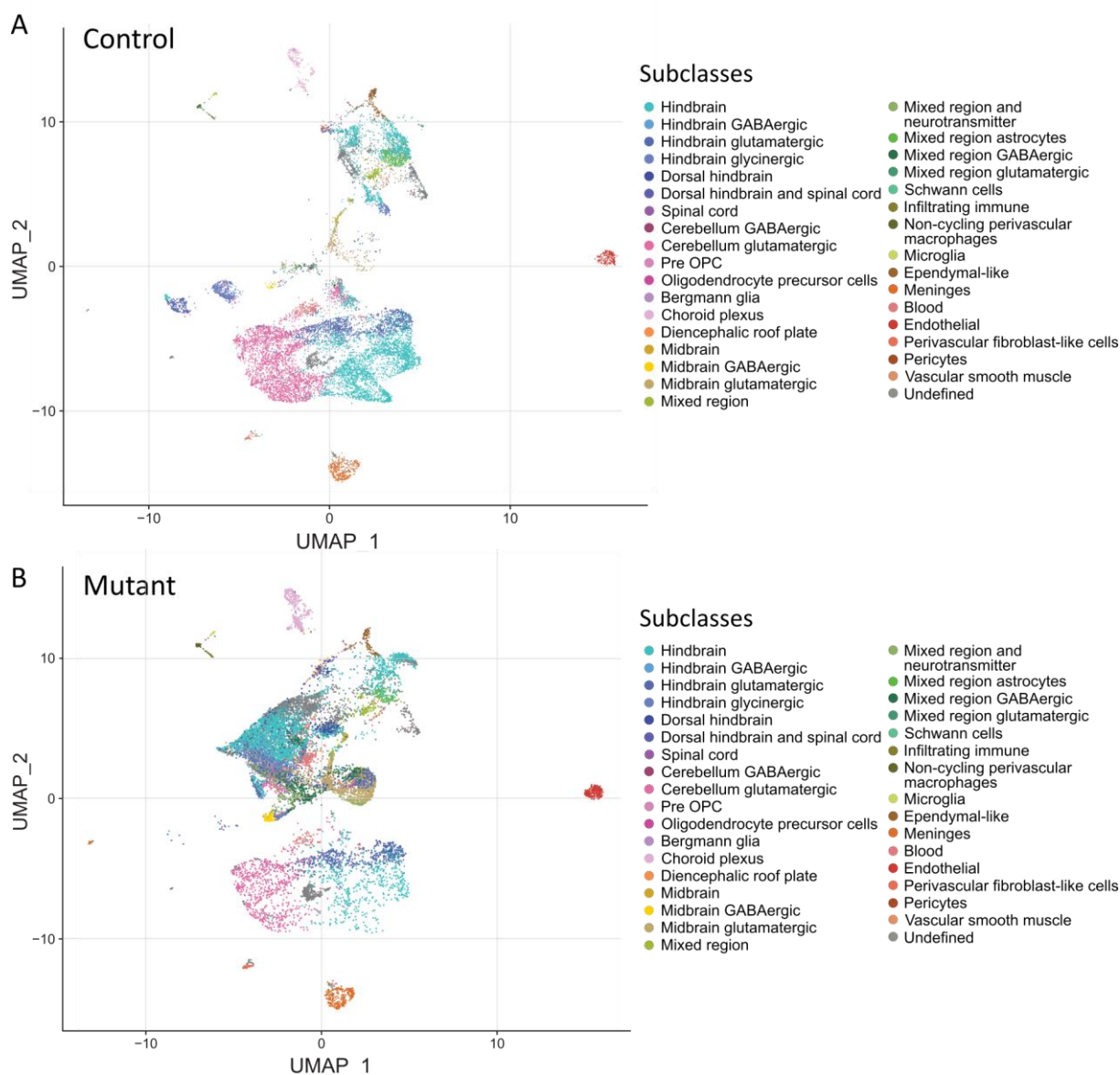
Supplementary Figure 6. Cerebellar lesions are not detected in other mutant genotypes at E14.5. (A-C) Mutants *Blbp-cre::Smarca4^{fl/fl}*, *Blbp-cre::Ctnnb1(ex3)^{fl/wt}*, and *Blbp-cre::Ctnnb1(ex3)^{fl/wt}::Smarca4^{fl/wt}* do not display any apparent phenotype at E14.5 in HE stainings of brains. (D-I) HE stainings show no formation of lesions in the cerebella of mutants. (J-O) Accumulation of β -catenin is not evident in any of the genotypes (J-L), whereas loss of SMARCA4 is visible in *Blbp-cre::Smarca4^{fl/fl}* mice only (M-O). (P-R) Proliferation in the ventricular zone is not increased in mutants according to Ki67 stainings. Scale bars in A-C correspond to 1 mm, in D-F to 200 μ m and in G-I to 20 μ m (also applicable to J-R). Only offspring of cre-positive mothers was included in analysis.



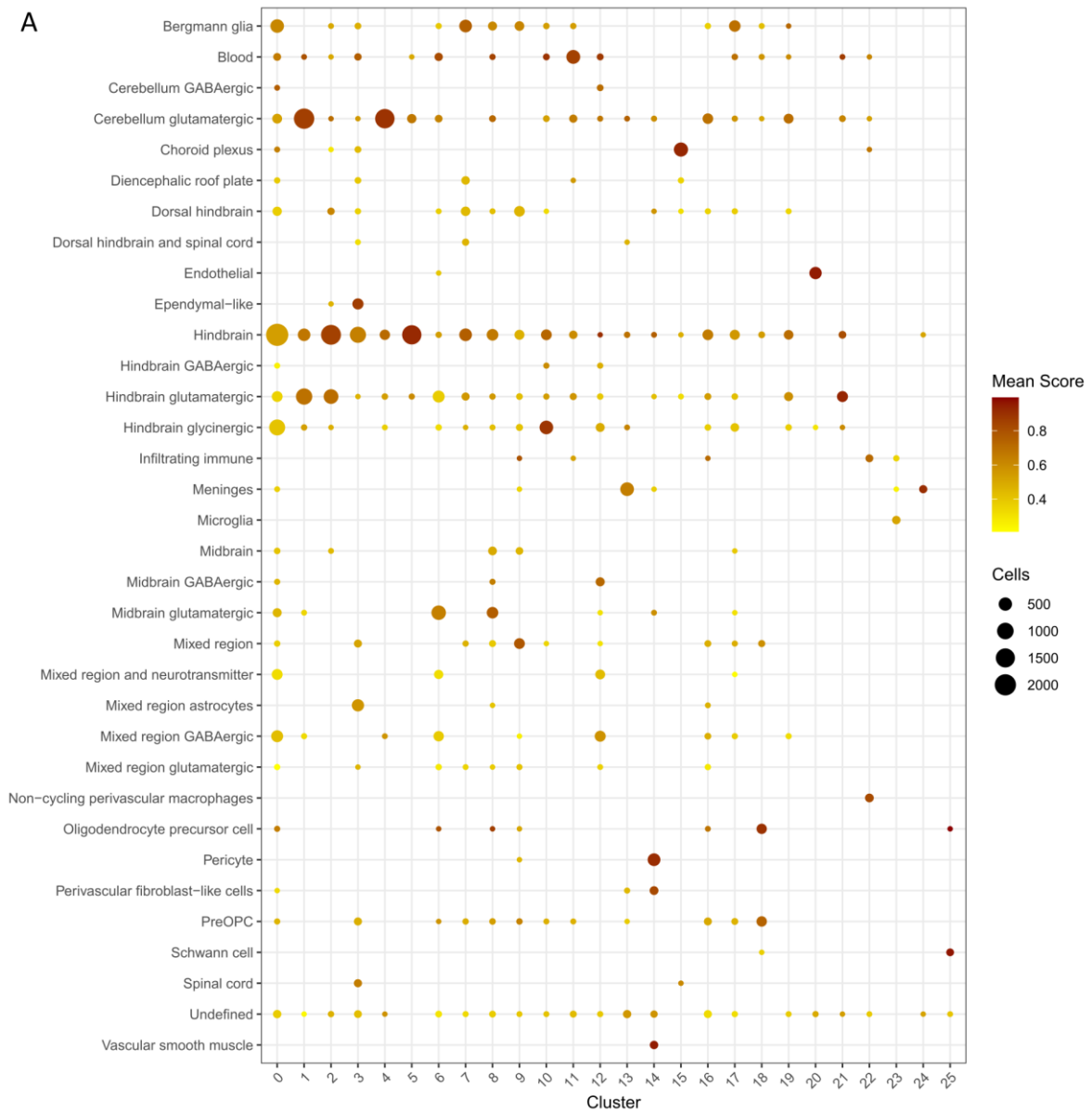
Supplementary Figure 7. *Blbp-cre::Ctnnb1(ex3)^{fl/wt}::Smarca4^{fl/fl}* mutants found at P0 do not show cerebellar lesions due to insufficient recombination. (A-C) Four mutants derived from cre-positive mothers found at P0 showed a loss of SMARCA4 in the cerebellum but no evidence of cerebellar lesions. (D) Recombination of *Smarca4* tested by PCR in genomic DNA from tail biopsies of histologically analyzed mutants from E12.5 to P0 shows recombination at all time points tested. (E) *Smarca4* recombination was also detected using DNA isolated from FFPE sections of mutant brains. (F) Using the same DNA samples as in E, recombination of *Ctnnb1* was only detected at E14.5 and E16.5 but not in mutants analyzed at P0. Scale bar in A corresponds to 250 μm and in B+C to 25 μm.



Supplementary Figure 8. Cerebellar lesions do not show a clear match to a human brain tumor entity in DNA methylation analysis. (A) UMAP clustering according to DNA methylation of cerebellar lesions of *Blbp-cre::Ctnnb1(ex3)^{fl/wt}::Smarca4^{fl/fl}* mice (Illumina Mouse Methylation BeadChip) and human brain tumors (Capper *et al.* 2018 [101], Sharma *et al.* 2019 [123]) using 640 orthologous CpG sites out of the 15,000 most differentially methylated CpG sites within the human dataset. Mouse samples show most similarity to ATRT subgroups. (B) Heatmap clustering according to DNA methylation of the same samples and CpG sites shows proximity of cerebellar lesions to PGGnC (paraganglionic, spinal non-CIMP [CpG island methylator phenotype]) and PTPR-A (papillary tumor of the pineal region, group A).



Supplementary Figure 9. Predicted subclasses in single-cell RNA sequencing analysis of control and mutant cerebella at E16.5. (A-B) UMAP clustering of single cells derived from control (A) and mutant (B) (*Blbp-cre::Ctnnb1(ex3)^{fl/wt::Smarca4^{fl/fl}}*) cerebella at E16.5 according to differential gene expression. For each cell, the predicted cell subclass with the highest score as defined by la Manno *et al.*, 2021 [204] is depicted. Mutant clusters show a high number of cells assigned to subclasses ‘hindbrain’ as well as ‘undefined’. Furthermore, the subclass ‘cerebellum glutamatergic’, which is well presented in the control, is highly diminished in mutants.



Supplementary Figure 10. Scores for predicted subclasses in single-cell RNA sequencing analysis according to clusters. Bubble chart reflecting the cell count (bubble size) and prediction score (color scale) for subclasses predicted according to la Manno *et al.*, 2021 [204] within clusters 0-25 including cells of both control and mutant (*Blbp-cre::Ctnnb1(ex3)^{fl/wt}::Smarca4^{fl/fl}*) cerebella at E16.5. In general, subclasses within clusters mainly including mutant cells (clusters 0, 6, 9, 17, 19) were predicted with lower scores.

8.2 Supplementary Tables

Suppl. Table 1. List of previously described Group 3 MB mouse models

First hit	Second hit	Cells of origin	System/Approach	Publication	Penetration	Latency
MYCN		GLT1 ⁺ hindbrain progenitors	GEMM	Swartling <i>et al.</i> 2010 [174]	75%	40-160 d
MYCN	p53 ^{-/-}	GLT1 ⁺ hindbrain progenitors	GEMM	Hill <i>et al.</i> 2015 [266]	100%	40-100 d
MYC	p53 ^{-/-}	GCPs (ATOH1 ⁺)	orthotopic transplantation	Kawauchi <i>et al.</i> 2012 [176]	100%	20-40 d
MYC	p53 ^{DN}	cerebellar stem cells (PROM1 ⁺ LIN ⁻)	orthotopic transplantation	Pei <i>et al.</i> 2012 [206]	33%	15-20 w
MYC ^{T58A}	p53 ^{DN}	cerebellar stem cells (PROM1 ⁺ LIN ⁻)	orthotopic transplantation	Pei <i>et al.</i> 2012 [206]	100%	6-12 w
MYC ^{T58A}	p53 ^{DN}	cerebellar stem cells (PROM1 ⁺ LIN ⁻)	orthotopic transplantation	Pei <i>et al.</i> 2012 [206]	100%	6-12 w
MYC ^{T58A}	p53 ^{DN}	GCPs	orthotopic transplantation	Pei <i>et al.</i> 2012 [206]	32%	108 d
MYC	p53 ^{-/-}	SOX2 ⁺ progenitors	orthotopic transplantation	Kawauchi <i>et al.</i> 2017 [177]	80%	6-11 w
MYC	p53 ^{DN}	BLBP ⁺ progenitors (PAX6 ⁺ /PAX2 ⁺ /SOX2 ⁺)	<i>in utero</i> electroporation	Kawauchi <i>et al.</i> 2017 [177]	100%	5-8 w
MYC	p53 ^{DN}	ATOH1 ⁺ progenitors	<i>in utero</i> electroporation	Kawauchi <i>et al.</i> 2017 [177]	100%	7 w
MYC	p53 ^{DN}	PTF1A ⁺ progenitors	<i>in utero</i> electroporation	Kawauchi <i>et al.</i> 2017 [177]	43%	9-11 w
MYC	p53 ^{DN}	GAD2 ⁺ progenitors	<i>in utero</i> electroporation	Kawauchi <i>et al.</i> 2017 [177]	36%	9-13 w
MYC	p53 ^{-/-}	Nestin ⁺ neural stem cells	targeted viral delivery (RCAS/tv-a)	Jenkins <i>et al.</i> 2016 [267]	50%	20-120 d
MYC ^{T58A}	GFI1	cerebellar stem cells (PROM1 ⁺ LIN ⁻)	orthotopic transplantation	Northcott <i>et al.</i> 2014 [120]	88%	24-70 d
MYC ^{T58A}	GFI1B	cerebellar stem cells (PROM1 ⁺ LIN ⁻)	orthotopic transplantation	Northcott <i>et al.</i> 2014 [120]	90%	24-40 d
MYC	GFI1	GCPs grown as neurospheres	orthotopic transplantation	Vo <i>et al.</i> 2017 [207]	100%	10-20 d
MYC ^{T58A}	GFI1	PROM ⁺ neural progenitors	orthotopic transplantation	Lee <i>et al.</i> 2019 [268]	100%	20-60 d
MYC	GFI1	cerebellar progenitors at P0	transfection of pups (PiggyBac)	Ballabio <i>et al.</i> 2020 [131]	32%	65-100 d
MYC	OTX2	cerebellar progenitors at P0	transfection of pups (PiggyBac)	Ballabio <i>et al.</i> 2020 [131]	74%	25-75 d
MYC	GFI1	S100b ⁺ progenitors	combined GEMM/Piggy Bac system	Ballabio <i>et al.</i> 2021 [269]	19%	n.a.
MYC	BCL2	Nestin ⁺ neural stem cells	targeted viral delivery (RCAS/tv-a)	Jenkins <i>et al.</i> 2016 [267]	18%	20-120 d
KMT2D ^{-/-}		Nestin ⁺ neural stem cells	GEMM	Dhar <i>et al.</i> 2018 [180]	35%	5-7 mo
random	p53 ^{R270H}	Nestin ⁺ neural stem cells	GEMM (Sleeping Beauty Transposase)	Beckmann <i>et al.</i> 2019 [181]	38%	n.a.
MYC ^{T58A}		SOX2 ⁺ ALDH1L1 ^{high} astrocyte progenitors	orthotopic transplantation	Tao <i>et al.</i> 2019 [178]	60-100%	20-100 d
MYC		GLT1 ⁺ hindbrain progenitors	GEMM	Mainwaring <i>et al.</i> 2023 [179]	62%	90-150 d
MYC		BLBP ⁺ progenitors	GEMM	Morcavallo <i>et al.</i> 2022*	n.a.	n.a.

*conference abstract [260]

Suppl. Table 2. List of differentially expressed genes ($\log_{2}FC \geq 2.5$ and $p \leq 0.01$) in MYC/SMARCA4 tumors compared to the SHH MB mouse model *Math1-cre::Smo^{fl/wt}* considering only genes with a human homolog

Gene (human homolog)	log ₂ FC expression	p-value	adjusted p-value	difference
MYC	5.221945327	2.17E-07	0.000112786	UP
GNL3	2.56460136	1.09E-06	0.00034119	UP
EGR1	2.956430221	2.78E-06	0.000578517	UP
LARS2	3.724486147	7.53E-06	0.001036929	UP
ATP6	2.951720465	1.17E-05	0.001352242	UP
FAM107A	3.050622984	1.81E-05	0.001714084	UP
CDR1	3.009762397	0.000171238	0.004874617	UP
TWIST1	2.948413935	0.000257649	0.006126849	UP
KCNIP4	3.370541583	0.000815343	0.011819973	UP
CRTAM	2.544433431	0.000974723	0.013159696	UP
HOXA5	2.550010512	0.001282387	0.015546325	UP
GRIN2C	2.650453836	0.001313098	0.015631532	UP
FABP4	3.334848453	0.001606812	0.017664943	UP
CBLN3	3.20728539	0.001816914	0.018723607	UP
PEG10	2.654550882	0.001854505	0.018936111	UP
IGF2BP1	2.661333844	0.002217071	0.021238549	UP
GABRA6	2.623622846	0.003252566	0.026601477	UP
GLRA2	-3.008378179	5.22E-10	3.31E-06	DOWN
TTR	-7.977945444	7.02E-10	3.31E-06	DOWN
TNC	-4.317085673	7.02E-10	3.31E-06	DOWN
ISLR2	-3.863698218	2.26E-09	7.24E-06	DOWN
COL9A3	-2.778762879	3.29E-09	7.24E-06	DOWN
CSMD2	-2.5379476	3.55E-09	7.24E-06	DOWN
BARHL1	-2.969552139	3.58E-09	7.24E-06	DOWN
PPP1R14C	-3.49392389	4.52E-09	8.00E-06	DOWN
DGKK	-3.122036297	5.70E-09	8.25E-06	DOWN
SFRP1	-3.946703422	5.83E-09	8.25E-06	DOWN
FREM2	-2.776972787	6.57E-09	8.45E-06	DOWN
GPR17	-3.454789269	2.66E-08	2.69E-05	DOWN
PCSK9	-3.200447994	3.55E-08	3.35E-05	DOWN
LRRC55	-2.748088419	4.96E-08	4.39E-05	DOWN
NHLH2	-2.763707513	7.28E-08	6.06E-05	DOWN
KIF21B	-2.704675498	1.32E-07	9.37E-05	DOWN
NGFR	-2.587954691	2.12E-07	0.000112786	DOWN
NAV1	-3.036762976	2.24E-07	0.000112786	DOWN
MYCN	-3.581832876	2.88E-07	0.000131322	DOWN
MFAP4	-4.10158751	3.24E-07	0.000139018	DOWN
FOXJ1	-2.505206443	3.65E-07	0.000147501	DOWN
DCX	-4.400747974	3.92E-07	0.000154207	DOWN
GPRIN3	-2.730461692	2.06E-06	0.000471964	DOWN
FXVD6	-3.115214195	2.60E-06	0.000548187	DOWN

Gene (human homolog)	logFC expression	p-value	adjusted p-value	difference
HTR2C	-2.582433268	3.04E-06	0.000587007	DOWN
NCAN	-3.20653512	3.15E-06	0.000587007	DOWN
EGFR	-2.51520312	3.80E-06	0.000697518	DOWN
CACNG4	-3.112686023	4.03E-06	0.000721799	DOWN
FABP7	-4.585817638	4.31E-06	0.000734006	DOWN
EDNRB	-3.199575349	5.30E-06	0.000842952	DOWN
MDGA1	-2.73438028	7.41E-06	0.001036929	DOWN
NHLH1	-3.190476772	8.55E-06	0.001099171	DOWN
SLC6A11	-2.76818048	1.39E-05	0.001477066	DOWN
KCNJ6	-2.82122105	2.92E-05	0.002014205	DOWN
MIAT	-2.991693881	3.08E-05	0.002055407	DOWN
SLC6A2	-2.611892483	4.71E-05	0.002504192	DOWN
DPYSL3	-3.026303087	4.79E-05	0.00251728	DOWN
AQP4	-3.636199478	6.33E-05	0.00288804	DOWN
TUBB2B	-2.769118711	8.22E-05	0.0033499	DOWN
SLC17A6	-3.042946826	0.000133265	0.004265998	DOWN
DCC	-3.14659226	0.000247667	0.006010696	DOWN
GRM5	-2.531919833	0.001056143	0.013785399	DOWN
IGFBPL1	-2.656242367	0.006014076	0.037585316	DOWN

Suppl. Table 3. Predicted classes in single-cell RNA sequencing analysis of control cerebellum at E16.5

Cluster	Predicted class										
	Blood	Choroid plexus	Fibroblast	Glioblast	Immune	Neuroblast	Neuron	Oligodendrocyte	Radial glia	Schwann cell	Vascular
0	0	0	0	0	0	2	5	0	0	0	0
1	2	0	0	0	0	1014	1319	0	0	0	0
2	0	0	0	1	0	1901	1	0	20	0	0
3	18	4	0	1001	0	8	1	0	241	0	2
4	0	0	0	0	0	190	1345	0	0	0	0
5	1	0	0	0	0	1419	95	0	0	0	0
6	6	0	0	1	0	3	105	0	0	0	0
7	0	0	0	326	0	58	1	0	514	0	0
8	0	0	0	15	0	162	11	0	25	0	0
9	0	0	0	149	0	9	0	0	43	0	0
10	16	0	0	3	0	407	350	0	24	0	1
11	246	0	0	2	0	72	47	0	2	0	1
12	5	0	0	0	0	4	170	0	0	0	0
13	0	0	329	1	0	8	3	0	1	0	21
14	0	0	28	1	0	6	2	0	0	0	258
15	0	193	0	0	0	0	0	0	7	0	0
16	0	0	0	57	1	251	212	2	6	0	3
17	0	0	0	0	0	0	0	0	0	0	0
18	2	0	0	185	0	6	1	125	3	0	0
19	0	0	0	0	0	4	4	0	0	0	0
20	0	0	0	0	0	0	1	0	0	0	178
21	2	0	0	0	0	173	127	0	0	0	1
22	0	0	0	0	68	0	1	0	0	0	0
23	0	0	1	0	53	0	0	0	0	0	0
24	0	0	6	0	0	1	0	0	0	0	0
25	0	0	1	0	0	0	0	0	0	36	0
SUM	298	197	365	1742	122	5698	3801	127	886	36	465

Suppl. Table 4. Predicted classes in single-cell RNA sequencing analysis of mutant (*Blbp-cre::Ctnnb1(ex3)^{fl/wt}::Smarca4^{fl/fl}*) cerebellum at E16.5

Cluster	Predicted class										
	Blood	Choroid plexus	Fibroblast	Glioblast	Immune	Neuroblast	Neuron	Oligodendrocyte	Radial glia	Schwann cell	Vascular
0	49	3	4	11	0	2171	1702	4	1053	0	21
1	0	0	0	0	0	362	452	0	0	0	0
2	1	0	0	0	0	479	0	0	16	0	0
3	12	1	0	425	0	5	0	0	126	0	1
4	0	0	0	0	0	17	222	0	0	0	1
5	0	0	0	0	0	145	11	0	0	0	0
6	59	0	0	3	0	17	1259	1	9	0	1
7	0	0	0	19	0	52	0	0	178	0	0
8	6	0	0	253	0	240	32	1	133	0	1
9	0	0	1	89	1	131	1	1	416	0	1
10	0	0	0	0	0	9	15	0	2	0	0
11	329	0	0	1	1	30	15	0	11	0	0
12	13	0	0	0	0	6	473	0	1	0	0
13	0	0	248	0	0	2	1	0	1	0	16
14	0	0	63	0	0	1	1	0	1	0	269
15	0	406	0	1	0	0	0	0	11	0	0
16	0	0	0	39	0	33	13	0	1	0	0
17	9	0	0	91	0	120	74	0	318	0	0
18	2	0	0	48	0	0	0	62	0	1	0
19	1	0	0	0	0	244	167	0	4	0	1
20	0	0	0	0	0	0	0	0	0	0	210
21	0	0	0	0	0	2	2	0	0	0	0
22	1	1	0	0	68	0	0	0	0	0	0
23	0	0	0	0	25	0	0	0	0	0	0
24	0	0	53	0	0	0	0	0	1	0	1
25	0	0	0	0	0	0	0	1	0	7	1
SUM	482	411	369	980	95	4066	4440	70	2282	8	524

Suppl. Table 5. Predicted age in single-cell RNA sequencing analysis of control and mutant (*Bibp-cre::Ctnnb1(ex3)^{fl/wt}::Smarca4^{fl/fl}*) cerebellum at E16.5 according to la Manno *et al.* 2021 from E10.0 to E16.5 [204]

Cluster	Predicted age										Cell Count	
	E10.0	E11.0	E12.0	E13.0	E13.5	E14.0	E15.0	E16.0	E16.5	Mean	Control	Mutant
0	0	8	7	7	34	925	3043	481	521	15.04	7	5019
1	0	0	0	0	0	5	725	308	2111	16.10	2335	814
2	1	1	1	0	0	6	593	607	1210	15.99	1923	496
3	0	2	0	0	0	0	534	256	1055	15.99	1277	570
4	0	0	0	0	0	0	866	417	492	15.65	1535	240
5	0	0	0	0	0	2	593	526	550	15.81	1515	156
6	0	0	7	261	100	263	795	10	29	14.38	115	1350
7	0	0	0	0	0	4	456	100	588	15.85	899	249
8	3	41	0	1	0	42	654	43	95	14.96	213	666
9	4	49	9	15	0	78	328	152	207	15.38	201	641
10	2	2	1	0	0	7	559	78	178	15.33	801	26
11	1	7	0	0	0	6	350	340	58	15.51	371	391
12	0	0	0	11	10	46	489	46	76	15.11	180	498
13	0	0	0	0	0	32	407	165	29	15.28	365	268
14	0	0	1	0	0	11	280	281	57	15.56	295	335
15	0	0	0	0	0	0	524	86	9	15.16	200	419
16	0	0	0	0	0	0	494	12	112	15.29	532	86
17	0	0	0	0	0	13	402	68	129	15.41	0	612
18	0	0	0	0	0	0	140	113	191	15.90	329	115
19	0	0	0	0	0	8	99	31	287	16.07	8	417
20	0	0	0	0	0	0	239	34	116	15.53	179	210
21	0	0	0	0	0	2	192	72	41	15.43	303	4
22	0	0	0	0	0	20	87	32	0	15.09	69	70
23	0	0	0	0	0	0	45	2	32	15.63	54	25
24	0	0	0	0	0	0	59	2	1	15.06	7	55
25	0	0	0	0	0	0	39	6	1	15.16	37	9

9 DANKSAGUNG

Ein großes Dankeschön geht zunächst an Ulrich Schüller, der stets an das Projekt geglaubt hat und immer positive Aspekte finden konnte, auch wenn es Rückschläge und gescheiterte Experimente hagelte. Vielen Dank für deine Verlässlichkeit und deine Offenheit für neue Ideen und Veränderungen, das ist nicht selbstverständlich.

Danke für die großartige Unterstützung der gesamten AG Schüller, die in den vielen Labmeetings, aber auch beim gemeinsamen Mittagessen und Kaffee trinken nicht nur für fachlichen, sondern auch moralischen Support gesorgt hat. Besonders möchte ich mich bei Melanie bedanken, die mich über die gesamte Zeit hinweg begleitet hat und mit Rat und Tat zur Seite stand. Großer Dank geht auch an Catena, vor allem für das gemeinsame Durchstehen der Corona-Zeit und der späten Abende im Labor. Vielen Dank an Dörthe, die mich in das Projekt eingeleitet hat, mir methodisch und fachlich viel beibringen konnte, aber auch für sportliche Motivation nach der Arbeit gesorgt hat. Diese Arbeit wäre außerdem nicht möglich gewesen ohne die Unterstützung unserer fleißigen TAs Jacky und Vanessa, tausend Dank für all eure Hilfe! Herzlichen Dank auch an unsere ehemaligen Hiwis Margarethe und Jessi.

Ein riesiges Dankeschön geht an all die helfenden Hände in der Neuropathologie für die Unmengen an Schnitten und Färbungen: ohne euch gäbe es die schönen Abbildungen nicht!

Ich möchte mich außerdem für all die Hilfe aus dem Leibniz-Institut für Virologie bedanken, allen voran bei den Mitarbeitern im Tierstall, die sich immer ausgezeichnet um unsere Mäuse gekümmert haben. Großer Dank geht auch an Gundula Pilnitz-Stolze für die Hilfe bei der Histo und an Arne Düsedau für die Unterstützung am FACS.

Danke an die Mädels aus der AG Müller für die schönen Mittagspausen, die Doppelkopf-Runden und den regen Austausch im ersten Jahr.

Vielen Dank auch an Shweta Godbole, Julia Neumann und Michael Spohn, die mich mit zahlreichen bioinformatischen Analysen unterstützt haben.

Zudem möchte ich mich bei den Mitgliedern meines Thesis-Komitees, Prof. Harriet Wikman-Kocher und Prof. Stefan Rutkowski für den Input und die motivierenden Worte bedanken.

Zuletzt geht ein großes Dankeschön an meine Familie und vor allem an Enno, der über die gesamte Zeit hinweg für mich da war und ohne dessen Unterstützung vieles nicht möglich gewesen wäre.

10 CURRICULUM VITAE

Der Lebenslauf wurde aus datenschutzrechtlichen Gründen entfernt.

11 LIST OF PUBLICATIONS

Two manuscripts based on the data presented in this thesis are currently in preparation for submission.

Co-authorships during PhD program:

Brugmans AK, Walter C, Moreno N, **Göbel C**, Holdhof D, de Faria F, Hotfilder M, Jeising D, Frühwald MC, Skryabin BV, Rozhdestvensky TS, Wachsmuth L, Faber C, Dugas M, Varghese J, Schüller U, Albert TK, Kerl K. A Carboxy-terminal *Smarch1* Point Mutation Induces Hydrocephalus Formation and Affects AP-1 and Neuronal Signalling Pathways in Mice. *Cell Mol Neurobiol* (2023). doi: 10.1007/s10571-023-01361-5. PMID: 37219662.

Neyazi S, Altendorf L, Schwetje D, **Göbel C**, Schoof M, Holdhof D, Schüller U. Generation of new transgenic SMARCA4-deficient mouse models results in neuromuscular weakness and paralysis of limbs. *Brain Pathol.* (2023). doi: 10.1111/bpa.13146. PMID: 36582072

Ricklefs FL, Fita KD, Mohme M, Mawrin C, Rahmzade R, Sahm F, Dührsen L, **Göbel C**, Lamszus K, Westphal M, Schüller U, Eicker SO. Genetic and epigenetic profiling identifies two distinct classes of spinal meningiomas. *Acta Neuropathol.* (2022). doi: 10.1007/s00401-022-02504-6. PMID: 36163595

Graf M, Interlandi M, Moreno N, Holdhof D, **Göbel C**, Melcher V, Mertins J, Albert TK, Kastrati D, Alfert A, Holsten T, de Faria F, Meisterernst M, Rossig C, Warmuth-Metz M, Nowak J, Meyer Zu Hörste G, Mayère C, Nef S, Johann P, Frühwald MC, Dugas M, Schüller U, Kerl K. Single-cell transcriptomics identifies potential cells of origin of MYC rhabdoid tumors. *Nat Commun.* (2022). doi: 10.1038/s41467-022-29152-4. PMID: 35318328

Holdhof D, Schoof M, Al-Kershi S, Spohn M, Kresbach C, **Göbel C**, Hellwig M, Indenbirken D, Moreno N, Kerl K, Schüller U. Brahma-related gene 1 has time-specific roles during brain and eye development. *Development* (2021). doi: 10.1242/dev.196147. PMID: 34042968

Holdhof D, On JH, Schoof M, **Göbel C**, Schüller U. Simultaneous Brg1 Knockout and MYCN Overexpression in Cerebellar Granule Neuron Precursors Is Insufficient to Drive Tumor Formation but Temporarily Enhances their Proliferation and Delays their Migration. *Cerebellum* (2021). doi: 10.1007/s12311-020-01219-2. PMID: 33387268

Previous authorships:

Göbel C, Goetzke R, Eggermann T, Wagner W. Interrupted reprogramming into induced pluripotent stem cells does not rejuvenate human mesenchymal stromal cells. *Sci Rep.* (2018). doi: 10.1038/s41598-018-30069-6. PMID: 30076334

12 EIDESSTATTLICHE VERSICHERUNG

Ich versichere ausdrücklich, dass ich diese Arbeit selbständig und ohne fremde Hilfe verfasst, andere als die von mir angegebenen Quellen und Hilfsmittel nicht benutzt und die aus den benutzten Werken wörtlich oder inhaltlich entnommenen Stellen einzeln nach Ausgabe (Auflage und Jahr des Erscheinens), Band und Seite des benutzten Werkes kenntlich gemacht habe. Ferner versichere ich, dass ich die Dissertation bisher nicht einem Fachvertreter an einer anderen Hochschule zur Überprüfung vorgelegt oder mich anderweitig um Zulassung zur Promotion beworben habe. Ich erkläre mich einverstanden, dass meine Dissertation vom Dekanat der Medizinischen Fakultät mit einer gängigen Software zur Erkennung von Plagiaten überprüft werden kann.

Unterschrift: